Università degli Studi di Milano - Bicocca
Facoltà di Scienze MM. FF. NN.
Department of Materials Science

Doctor of Philosophy Dissertation

Synthesis and characterization of Mg-Al-Ni alloys and Li-Mg borohydrides for hydrogen storage

by

Angeloclaudio Nale

Supervisor: prof. Michele Catti

Contents

Contents i

1 Introduction 3

I Metal hydrides 7

2 Mg-Al-Ni alloys 9
2.1 Introduction 9
2.2 Experimental 10
2.3 Synthesis and XRD characterization of the Mg-Al-Ni alloys 11
2.4 Hydrogenation reactions 14
2.5 Conclusions 19

II Complex hydrides 21

3 Chemical synthesis 23
3.1 Introduction 23
3.2 Handling and chemical synthesis operations 24
3.2.1 X-Ray Diffraction 27
3.2.2 Ball milling 28
3.2.3 Thermal analysis 28
3.2.4 Elemental analysis 29
3.3 Synthesis procedures 29
3.3.1 Direct synthesis 29
3.3.2 Metathesis reactions: ball milling and crystallization 31
3.3.3 Synthesis reactions: mechanochemical 32
3.3.4 Synthesis reactions: dissolution 32

4 Material characterization **35**
4.1 X-Ray diffraction . . . 35
4.1.1 $LiBH_4$-$Mg(BH_4)_2$ mixture . . . 35
4.1.2 $x$$LiBH_4$-(1-$x$)$Mg(BH_4)_2$ composite . . . 36
4.2 Thermal Analysis . . . 38
4.2.1 High Pressure Differential Scanning Calorimetry . . . 38
4.2.2 Thermo Gravimetric Analysis, Differential Scanning Calorimetry and Mass Spectrometry . . . 40
4.3 In-Situ X-Ray Diffraction . . . 42
4.4 Phase Diagram . . . 46
4.5 Hydrogen Desorption . . . 46
4.6 Conclusions . . . 47

5 Thermodynamic Measurements **49**
5.1 Chemical model . . . 49
5.2 The *Gas Reaction Controller* Sievert's Apparatus . . . 51
5.2.1 Layout of GRC . . . 51
5.2.2 Operations of GRC . . . 51
5.2.3 Beattie-Bridgeman Equation . . . 53
5.2.4 Benedict-Webb-Rubin Equation of State . . . 54
5.2.5 *Soak* and *Release* modes . . . 54
5.2.6 *Pressure composition isotherm* modes . . . 56
5.2.7 *Monitor* mode . . . 61
5.3 Performed decomposition experiments . . . 65
5.3.1 Decomposition of $LiBH_4$ . . . 66
5.3.2 Decomposition of $Mg(BH_4)_2$ . . . 70
5.3.3 Decomposition of $0.6LiBH_4$–$0.4Mg(BH_4)_2$ . . . 78

6 Conclusions **85**

Bibliography **87**

Abstract

Two important classes of hydrogen storage materials were considered: metallic alloys and molecular borohydrides. Each of them has advantages and disadvantages. Alloys absorb and release hydrogen reversibly and promptly, but in relatively small amount, whereas borohydrides decompose irreversibly yielding over 10 wt% of H2. Two systems of suitable chemical composition were selected from such classes, and materials belonging to them were synthesized and characterized from the structural and thermal point of view; then detailed and thorough experiments of dehydrogenation were performed on them, in order to determine the thermodynamic and kinetic aspects of the hydrogen release.

Within metallic alloys, the Mg-Al-Ni was selected to study the addition of Al to the Mg-Ni system. Samples with Mg_mAlNi_n composition (m,$n \leq 3$) were synthesized by ball milling; by X-ray diffraction studies, they were found to be a basically single phase with substitutionally disordered CsCl-type cubic structure. Only compositions with m large and n small proved to segregate minor quantities of Mg and Mg_2Ni. Hydrogenation experiments on the Mg_2AlNi_2 sample by the PCI technique (Sievert apparatus) showed a reversible absorption/desorption of 1.4 wt% H_2 with formation / decomposition of the MgH_2 and Mg_2NiH_4 hydrides. A particularly favourable dehydrogenation temperature (T $\geq$ 531 K for p $\geq$ 1 bar) was observed, by comparison with those of the single phase hydrides. Also the kinetics of the gas release proved to be satisfactory, indicating that addition of Al improves the H-storage performance of the Mg-Ni alloy substantially.

The mixed $LiBH_4$–$Mg(BH_4)_2$ borohydride system was investigated, to determine its possible better performance as hydrogen storage material with respect to the end-members pure borohydrides. Several composites were synthesized by ball milling, namely $x$$LiBH_4$–(1-$x$)$Mg(BH_4)_2$ with x = 0, 0.10, 0.25, 0.33, 0.40, 0.50, 0.60, 0.66, 0.75, 0.80, 0.90, 1. The physical mixture was investigated by using X- ray powder diffraction and thermal analysis. Interestingly, already a small amount of $LiBH_4$ proved to make the α to β transition of $Mg(BH_4)_2$ reversible, which had not been reported before. The eutectic composition was found to exist at $0.50 < x < 0.60$, exhibiting a eutectic melting at 180 °C. A phase diagram was built based on the data obtained in this study. Furthermore, the decomposition of the material begins right after the melting; thus the decomposition temperature of the composite is much lower than those of the pure borohydrides. At 270 °C the x = 0.50 composite releases about 7.0 wt% of hydrogen.

A full thermodynamic study of the dehydrogenation reaction was performed (Sievert apparatus) on the eutectic mixture, 0.6$LiBH_4$–0.4$Mg(BH_4)_2$, and on the end members $LiBH_4$ and $Mg(BH_4)_2$. Both the dynamic technique (constant pressure, temperature ramp vs. time) and the equilibrium mode (constant temperature, variable pressure with waiting time for pressure equilibration) were

employed to measure the wt% of H_2 released. It was found that the decomposition behavior of the eutectic composite is quite similar to that of $Mg(BH_4)_2$, but the starting temperature of the process is substantially lower, as shown by DSC measurements, opening the way to possible applications. With the help of Van't Hoff plots and by comparison with literature data, it was possible to analyze the dehydrogenation mechanism of the eutectic composite in terms of four steps, implying the intermediate formation of MgH_2. Lithium borohydride proved to play an important role in assisting the final decomposition of MgH_2.

Chapter 1

Introduction

Hydrogen gas is now considered to be the most promising fuel of the future for various applications, e.g. it can generate electricity, useful in cooking food, fuel for automobiles, hydrogen powered industries, jet planes, hydrogen village and for all our domestic energy requirements. Hydrogen as a fuel has already found applications in experimental cars and all the major car companies are in competition to build a commercial car and most probably they may market hydrogen fuel automobiles in near future. Hydrogen is already being used as the fuel of choice for space programmes around the world. It will be used to power aerospace transports to build the international space station, as well as to provide electricity and portable water for its inhabitants.

Hydrogen is the simplest and lightest element of our universe with only one proton and one electron [62], not available as element but in the form of compounds such as water needed for survival of human beings and hydrocarbons being used as a fuel today. Hydrogen has potential to solve fuel needs having three times higher energy efficient compared to petroleum.

For introduction of fuel cells in vehicle transportation, efficient hydrogen storage is necessary . Technical targets were established by US Department of Energy (DOE) and Freedom Car and were revised in 2010 [16]. In FY2005, DOE's office of Energy Efficiency and Renewable Energy (EERE) established three Center of Excellences (CoE) to develop hydrogen storage materials to meet the "Grand Challenge" [45].

Hydrogen storage is regarded as one of the key issues which have to be solved in the developing field of hydrogen technology [46, 42]. Of the various ways of storing hydrogen for fuel cell-driven applications, however, conventional storage systems based on liquefied and pressurized hydrogen exhibit principal drawbacks.

Pressurized hydrogen can be stored in containers made of composite materials that have to withstand pressures of up to 700 bar in order to carry enough fuel

for a reasonable driving cycle of 400–500 km. In this case, however, there are safety concerns related to a tank rupture in an accident. Technical problems arise e.g. from adiabatic effects when expanding and compressing the hydrogen during refuelling. Furthermore, current containers do not allow operation at temperatures below freezing point due to the risk of failure of the composite structure.

To increase the stored mass per container volume, liquefied hydrogen with a density of 70.8 kg/m3 is particularly attractive. For this purpose, the hydrogen has to be cooled down to 21 K, which, however, needs about one third of the energy content of the stored hydrogen. Overall efficiency is further reduced by a finite heat transfer through the insulated vessel, leading to a loss of 2–3% of vaporized hydrogen per day. In order to prevent a high pressure build-up (the critical temperature of hydrogen is 32 K), the overpressure must be released from the tank, e.g. via a catalytic converter.

A practical solution to circumvent these drawbacks would be storage in a material that can readily take up and release large amounts of hydrogen. According to car manufacturers and the technical targets of the US Department of Energy for 2010 and 2015, more than 6 wt% of hydrogen should be contained in such a system, including tank and valves, and the filling time should not exceed 5 min. Furthermore, the thermal properties of the material have to match the operation conditions of the fuel cell, which means that the temperature necessary to release the hydrogen from the storage should not exceed the temperature of the exhaust gas of the fuel cell.

Driven by the DOE targets, the international metal hydrogen community intensified the exploration of the most hydrogen rich, light-weight compounds, such as the alanates, amides and metal borohydrides with AlH_4^-, NH_2^- and BH_4^- anionic complexes respectively, charged balanced by a cation matrix. Although these materials have been known in the literature for decades, their use for hydrogen storage had not been explored. One difficulty in the past was safe sample handling since these materials are more or less reactive in air and moisture. With the development of dry, purified argon or nitrogen filled glove boxes with only a few ppm oxygen and water levels, and, by adapting instruments for measurements in inert atmosphere, synthesis and characterization were enabled during the past 10 years.

The focus of the DOE Metal Hydride CoE (MHCoE) was reversible metal hydrides and one of the projects was dedicated to developing metal borohydrides. The group I borohydride $NaBH_4$ had been rigorously investigated for hydrogen storage applications, but, as a “chemical hydride” since reversibility was never shown [26]. Lithium borohydride, $LiBH_4$, was only known to be re-hydrided at temperatures above 600 °C at 150–350 bar (15–35 MPa) H_2-pressures [37] and [32], thus, we shifted our focus to development of the Group II borohydrides.

In the presented work, investigation has been made into two separated class of hydrides: metal hydrides based on magnesium and metal borohydrides.

Mg-based metal alloys have a favorable gravimetric H_2 content only with light elements but they present a good reversibility and a fast kinetic; the work focused in particular on metal alloys of Mg-Al-Ni system. Metal alloys have been synthesized, characterized and their hydrogen adsorption-desorption performances has been tested.

This work was carried out in collaboration with Dr. Andrea Parente by Dept. of Materials Science of University of Milano Bicocca.

Metal borohydrides have an extremely favorable gravimetric hydrogen content second, but they present an high decomposition temperature and their reversibility is possible only under severe conditions; the work focused on studying the Li-Mg-BH_4 system observing the formation an eutectic mixture: its composition was identified and its decomposition behavior has been investigated.

This work was carried out in collaboration with Dr. Elisa Gil Bardají and Prof. Maximilian Fichtner of the Karlsruhe Institute of Technology (KIT), Institute of Nanotechnology; in particular, the mechanochemical synthesis and eutectic characterization were performed during a 7 months stages at KIT, while the thermodynamic analysis was performed at the Dept. of Materials Science, University of Milano Bicocca.

Part I

Metal hydrides

Chapter 2

Mg-Al-Ni alloys

2.1 Introduction

Despite its well known weak points, magnesium hydride is still often considered to be the best hydrogen storage material which is presently available. Many efforts were made in the last years to improve its performance by lowering the decomposition temperature and/or improving the corresponding kinetics. In most cases, doping or alloying of elemental Mg with very minor quantities of other metals, oxides or different compounds was attempted; positive results were often obtained as far as the kinetics, but not thermodynamics, of the $MgH_2 \rightarrow Mg + H_2$ reaction is concerned [17, 28, 52].

Comparatively less explored was the way leading to real Mg-containing intermetallic compounds or alloys. Although a decrease of the storage capacity may be expected on reducing the Mg contents of the system drastically, significant improvements could be achieved with a lower dehydrogenation temperature. Within this line of research, the Mg-Ni and Mg-Al binary systems were investigated. The first one, which provides the important hydrogenation reaction $Mg_2Ni + 2H_2 \rightarrow Mg_2NiH_4$, is also attractive because of the well known catalytic properties of Ni [52]. Nanocrystalline Mg+Mg_2Ni composites were thus claimed to improve the hydriding kinetics of both components [27]. The Mg-Al system has aroused interest in the hope that, owing to the quite unstable Al-H bonding in aluminium hydride [12], a mixed Mg-Al hydride with intermediate bond strength between MgH_2 and AlH_3 could be formed. This was not found to occur; yet the $Mg_{17}Al_{12}$ binary compound proved to hydride reversibly with formation of MgH_2 and Al [3, 56].

Concerning the Mg-Al-Ni ternary composition, some studies were performed by doping Mg_2Ni with very minor Al quantities [44, 25], and an improvement of the desorption kinetics was generally observed. The $Mg_{1-x}Al_xNi$ [36] and

$Mg_{2-x}Al_xNi$ [58, 54] systems were explored within the x $\leq$ 0.5 compositional range, but in most cases the reaction with hydrogen was characterized only partially or was not considered at all. In particular, the Mg_3AlNi_2 compound turned out to present different cubic phases according to the preparation method: a $Fd\bar{3}m$ $NiTi_2$-type crystal structure, when synthesized by conventional heat treatments [58, 54], and a $Pm\bar{3}m$ CsCl-type structure when prepared by ball milling [11]. Also the ball milled $MgAlNi_2$ compound showed the CsCl-type phase [36]. The hydrogenation capacity proved to decrease substantially with the increase of the Al contents, but the equilibrium temperature of dehydrogenation at/or above room pressure was not investigated.

We thus started an investigation of a broader compositional area within the Mg-Al-Ni ternary system, along the Mg_mAlNi_n lines with m, n=1,2,3. The first aim was to synthesized samples with several compositions by mechanical alloying, in order to obtain nanocrystalline materials with best performance for the hydrogenation reaction. Secondly, we wanted to understand in what conditions single-phase or poly-phase materials are obtained, and to characterize the crystallographic features of such phases. The last goal was to assess the thermodynamic and kinetic behaviour of some of these samples with respect to hydrogen absorption/desorption. In particular, the active chemical species in hydride formation had to be clearly identified, and their effects on the temperature of dehydrogenation of the material at pressures not lower than 0.1 MPa were to be elucidated.

2.2 Experimental

The materials were prepared by mechanical alloying in Retsch PM100 planetary and a Spex 8000 high-energy ball mills (Ar atmosphere), with milling times varying from 30 to 100 hours, and Ball-to-Powder-mass-Ratios of 10:1. Reagent-grade pure metals were used as starting materials, and all samples were always handled in a glove-box filled with purified argon. The progress of the mechanochemical reaction was periodically checked by X-ray powder diffraction (XRD) in the course of the milling. The reaction was considered to be ended when no appreciable XRD change appeared on further milling. A Bruker D8 Advance powder diffractometer, with CuK radiation ($\lambda = 1.5418$ Å) and secondary-beam monochromator, was used for the X-ray characterization. Microstructural analyses were performed by means of a Scanning Electron Microscope (SEM: Tescan Vega Ts 5136) with an energy-dispersive X-ray spectrometer (EDX: EDAX Genesis 4000).

Thermodynamic and kinetic measurements of the hydrogenation/dehydrogenation reactions were done by the method of pressure-composition-isotherm (PCI), employing an automatic Sievert-type apparatus of the Advanced Materials Corporation. The sample of 0.5 g was loaded into the 5 cc reactor located in a furnace

with temperature control. After evacuation, hydrogen gas of high purity was introduced at increasing pressures.

2.3 Synthesis and XRD characterization of the Mg-Al-Ni alloys

Samples were synthesized (Spex 8000, 30 h milling time) with the 1:1, 1:2, and 1:3 Al/Ni molar ratios; for each of them, the Mg/Al ratio was increased from 1:1 to 3:1. In case of the Mg_2AlNi_2 composition, for which detailed hydrogenation measurements are reported below, other samples were also prepared by 100 h milling on the Retsch equipment. As main feature, the final XRD pattern of all samples showed four broad peaks of the CsCl-type $Pm\bar{3}m$ cubic structure in the $2\theta \leq 70°$ range (Figs. 2.1-2.3): (100), (110), (111), and (200) at increasing angles. The same structure is observed for the AlNi alloy, with a"=2.882 Å. The (100) and (111) reflexions, distinguishing the $Pm\bar{3}m$ from the $Im\bar{3}m$ space group (BCC lattice), appear to be comparatively weak in all diffractograms. Thus, the main phase present in all samples looks like a partially ordered solid solution with AlNi-type structure; if the two atomic sites at x=0, y=0, z=0 and 1/2,1/2,1/2 had the same average chemical composition, a true BCC lattice would be attained. In particular, as the intensity of Bragg peaks can be hardly affected by the Mg/Al distribution in view of the close scattering powers of such atoms, we can conclude that some disordering of (Mg,Al) vs. Ni should occur in at least one of the two sites of the CsCl-like structure, at variance with the full order observed in the AlNi alloy. A progressive separation of Mg out of the pseudo-BCC solid solution appears clearly to occur as m increases along each Mg_mAlNi_n series (Figs. 2.1-2.3). In addition to elemental Mg, also Mg_2Ni and Ni may separate for the compositions richest in Mg (Table 2.1). We also prepared samples with Mg/Al ratio of 4:1; in this case larger quantities of the same phases were observed in addition to the p-BCC solid solution, and results are not reported here.

Rietveld profile refinements of the collected XRD powder patterns were performed by the FULLPROF code [43]. Taking into account the poor quality of the data (small scattered intensity and few very broad Bragg peaks), due to low crystallinity of the nanoparticles, it was not possible to distinguish between Mg and Al atoms. The starting structure was then modelled with a full Mg atom in the 0,0,0 site and a mixture of Mg and Ni consistent with the sample nominal composition in the 1/2,1/2,1/2 site, considering Al equivalent to Mg. The Mg/Ni fraction was refined on each site, but the quantity of Ni in 0,0,0 never attained 10%, so that in most cases the starting composition was finally kept fixed. A pseudo-Voigt function was used for the Bragg peak profile, and the background was treated by interpolation through a number of selected points in the pattern. For the samples of the Mg_mAlNi series, with larger amounts of impurities (Fig.

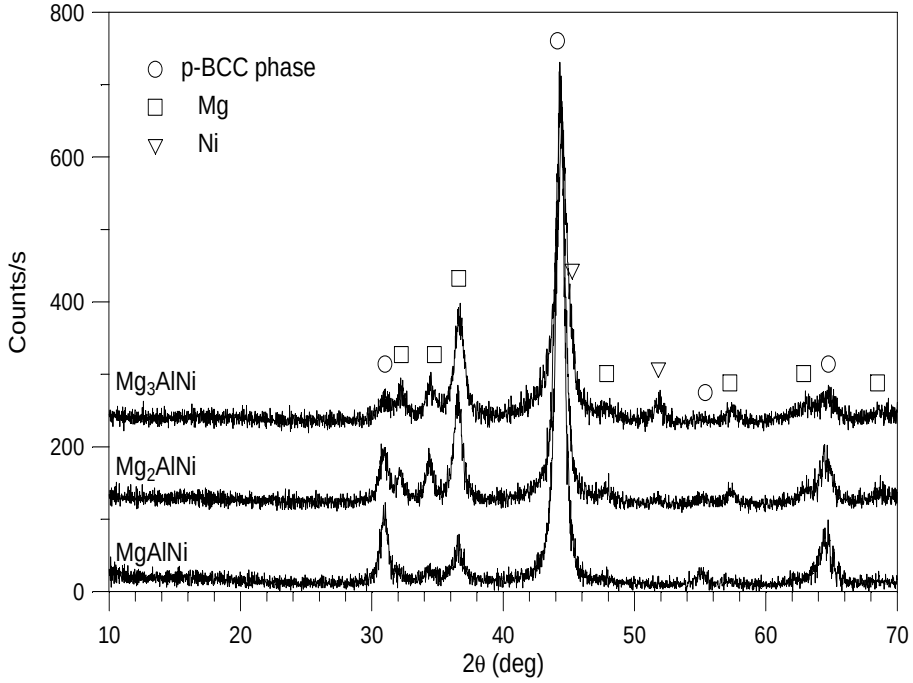

Figure 2.1: powder XRD patterns (CuKα radiation) of the Mg_mAlNi samples with m=1 to 3. The main phase is a pseudo-body-centered-cubic ($Pm\bar{3}m$ space group) AlNi-type solid solution.

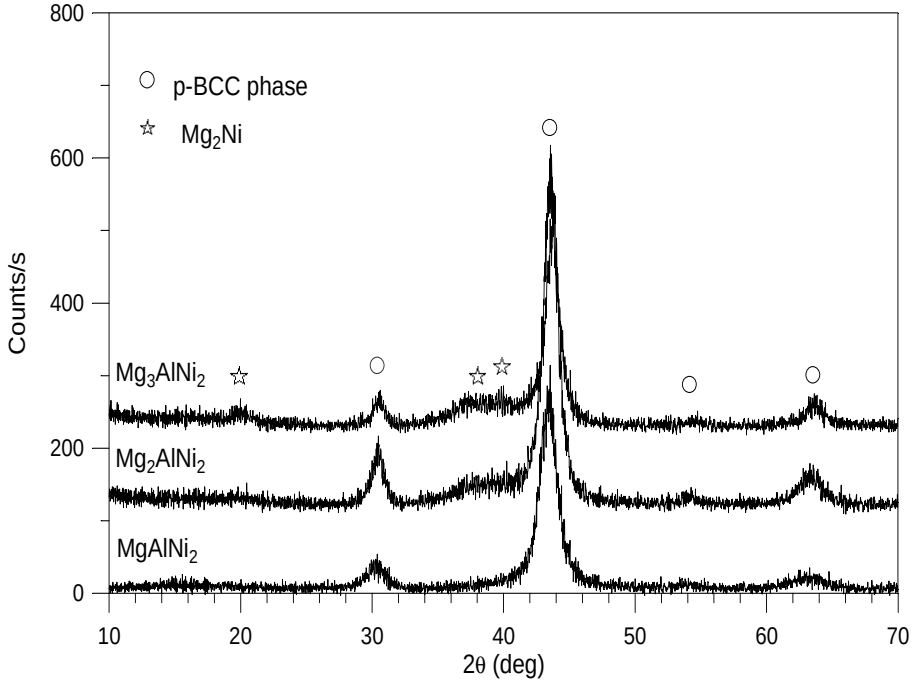

Figure 2.2: powder XRD patterns (CuKα radiation) of the Mg_mAlNi_2 samples with m=1 to 3.

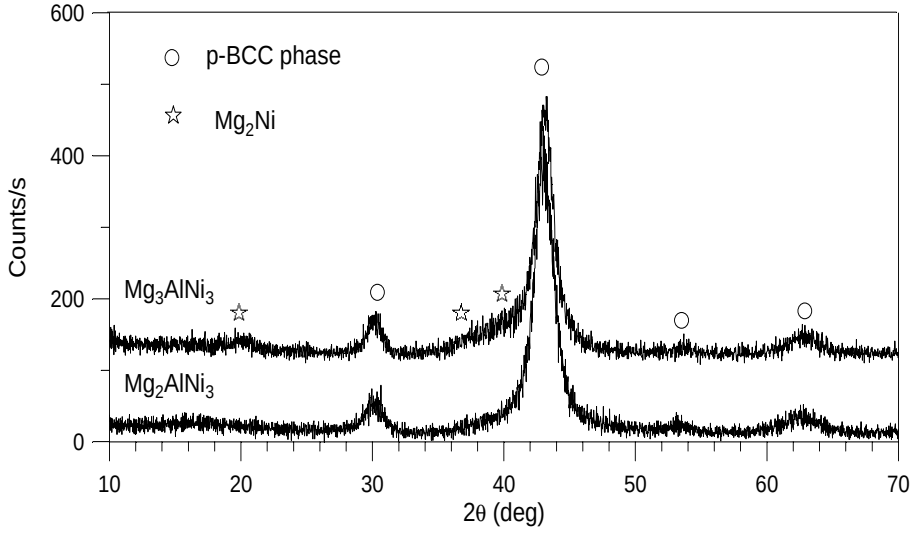

Figure 2.3: powder XRD patterns (CuKα radiation) of the Mg_mAlNi_3 samples with m=2 to 3.

	n=1	2	3
m=1	MgAlNi p-BCC (2.880 Å) + traces of Mg	$MgAlNi_2$ p-BCC (2.943 Å)	
2	Mg_2AlNi p-BCC (2.882 Å) + Mg	Mg_2AlNi_2 p-BCC (2.950 Å) + traces of Mg_2Ni	Mg_2AlNi_3 p-BCC (2.950 Å)
3	Mg_3AlNi p-BCC (2.884 Å) + Mg + Ni	Mg_3AlNi_2 p-BCC (2.925 Å) + traces of Mg_2Ni	Mg_3AlNi_3 p-BCC (2.946 Å) traces of Mg_2Ni

Table 2.1: phase compositions of the samples with nominal Mg_mAlNi_n stoichiometry, from powder XRD data (cf. Figs. 1-3). The cell edge a of the pseudo-body-centred-cubic AlNi-type main phase ($Pm\bar{3}m$ space group) is given in parentheses (the estimated uncertainty is 0.010 Å). AlNi itself has a= 2.882 Å.

2.1), Mg was included as a second phase in the refinement. Convergence was attained with average R_p and R_wp values of 0.13 and 0.18. The unit-cell parameters are reported in Table 2.1. The uncertainty is estimated to be of the order of 0.01 Å from results on different samples with the same composition. A clear trend of increasing a with the Ni content n is observed, consistent with its slightly larger metallic radius; in particular, the a values in the Mg_mAlNi series are comparable with the a of AlNi. The effect of Mg content on the unit-cell dimension can not

be assessed clearly, taking also into account the tendency to segregate Mg-rich phases in the Mg_3AlNi_n compositions.

In summary, the p-BCC solid solution is obtained by ball milling as a pure phase in a wide Mg-Al-Ni compositional range. The molar ratio Ni/(Mg+Al+Ni) seems to have a lower threshold of about 1/3, below which the solid solution starts to decompose segregating Mg-rich phases; similarly, a higher threshold of 1/2 can be observed for the Mg/(Mg+Al+Ni) ratio (Table 2.1). It should be remarked that this p-BCC phase is not reported in the phase diagrams of the Mg-Al-Ni ternary system [41], so that it is probably thermodynamically metastable, and the driving force for its formation may be related to the large surface area and small nanosize of the crystal particles.

The prepared compounds were examined by SEM with microanalysis attachment, which confirmed the nominal compositions by several spot samplings. No chemical unhomogeneities could be detected, so that the size of separated Mg-rich particles should be below the space resolution of the instrument. A typical SEM image is shown in Fig. 2.4 for the Mg_2AlNi_2 composition. The Scherrer equation

$$L = \frac{0.94\lambda}{B\cos\theta}$$

where $B(2\theta)$ is the full-width (radians) at half maximum intensity, was applied to the (110) peak of the pseudo-BCC phase in order to estimate the L size of the particles obtained by ball milling. Values in the 6-12 nm range are obtained, depending on sample composition and milling time.

2.4 Hydrogenation reactions

Some of the prepared samples were tested for hydrogenation by the PCI technique. In terms of wt% absorption Mg_2AlNi_2 gave the best results, which are hereafter reported in detail. A short activation treatment at 3 MPa and 473 K was sufficient to achieve the hydrogenation reaction. The H2 absorption and desorption isotherms in the 485-583 K range (Fig. 2.5) show that about 1.4 wt% of gas reacts reversibly with the alloy. At the lowest temperature of 485 K hydrogenation occurs at about 0.1 MPa, but the release of H_2 has to be forced below room pressure (p=25 kPa), yet with a limited Δp hysteresis. In order to dehydrogenate the sample at 0.12 MPa, T has to be raised to 531 K. In those conditions, the plateau of the hydrogenation step (average pressure 0.4 MPa) is not as stable as at lower temperature, and a larger hysteresis is observed. On rising temperature the pressure hysteresis is confirmed to increase, and the H_2 absorption process is kinetically hindered; however, the dehydrogenation isotherms are still very regular with flat plateaux, indicating good equilibrium conditions for the desorption process.

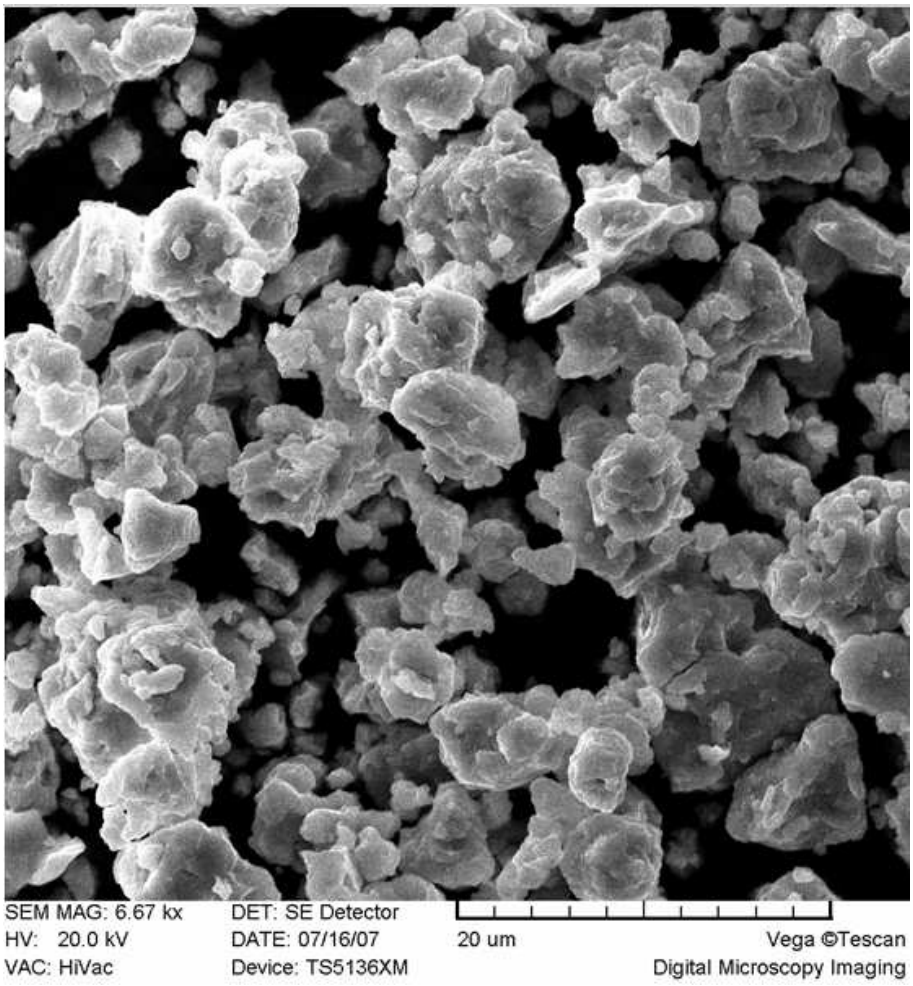

Figure 2.4: scanning Electron Microscope picture of the sample of Mg_2AlNi_2 prepared by ball milling.

From the equilibrium pressures of the four desorption curves of Fig. 2.5 (0.03, 0.12, 0.22 and 0.52 MPa), a van't Hoff plot of type

$$\ln\left(\frac{P}{P_0}\right) = -\frac{\Delta_r H}{R}\frac{1}{T} + \frac{\Delta_r H}{RT_0}. \tag{2.1}$$

was derived and displayed in Fig. 2.6. A good linear trend is shown by the data, and the following values of thermodynamic parameters are obtained by least-squares fitting: $\Delta rH = 67.7$ kJ mol^{-1} (enthalpy of dehydrogenation), and T_0= 524 K (temperature of dehydrogenation at p=0.1 MPa). The decomposition enthalpy is similar to the value reported for Mg_2NiH_4 (68 kJ mol^{-1} [40]), and significantly lower than that of MgH_2 (76 kJ mol^{-1} [4]).

Kinetic measurements were also performed for both the absorption and des-

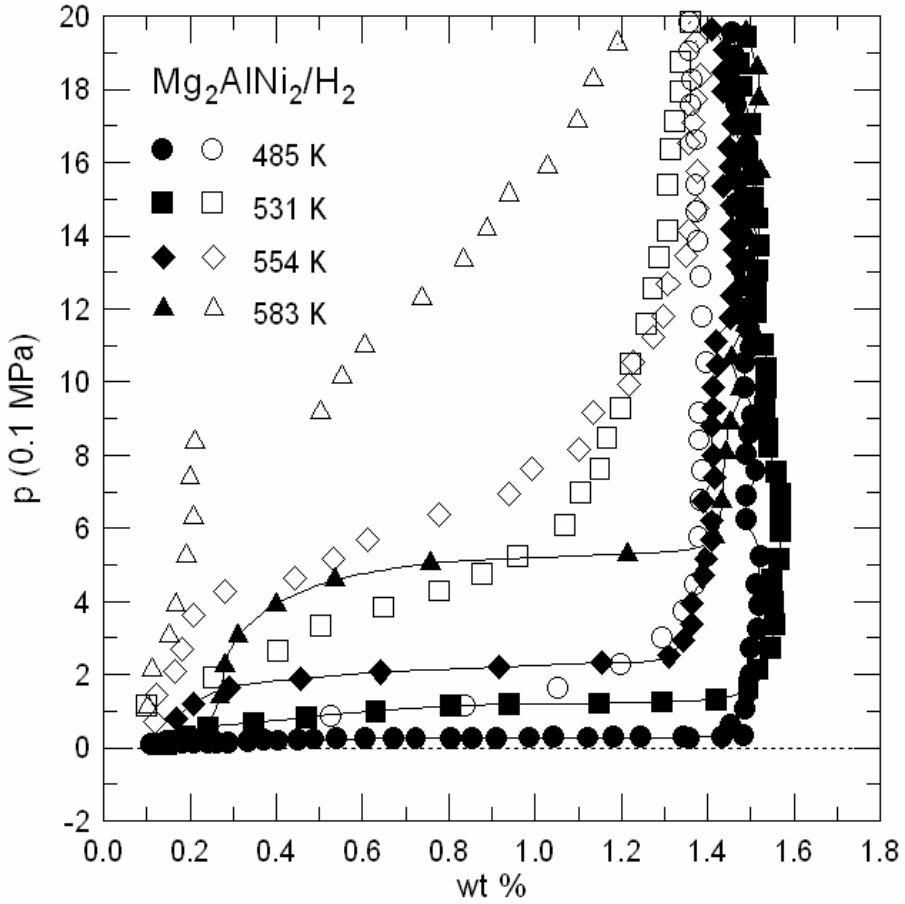

Figure 2.5: Pressure-Composition-Isotherms of the Mg_2AlNi_2/H_2 system at four different temperatures. Full and open symbols refer to hydrogen desorption and absorption, respectively.

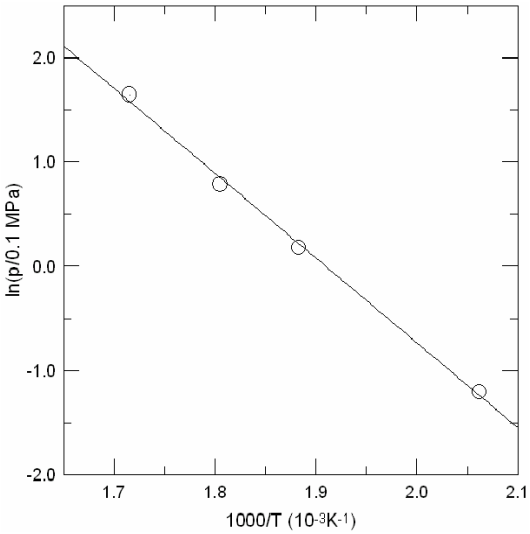

Figure 2.6: van't Hoff plot of the dehydrogenation reaction of hydrogenated Mg_2AlNi_2, from data of Fig. 2.5.

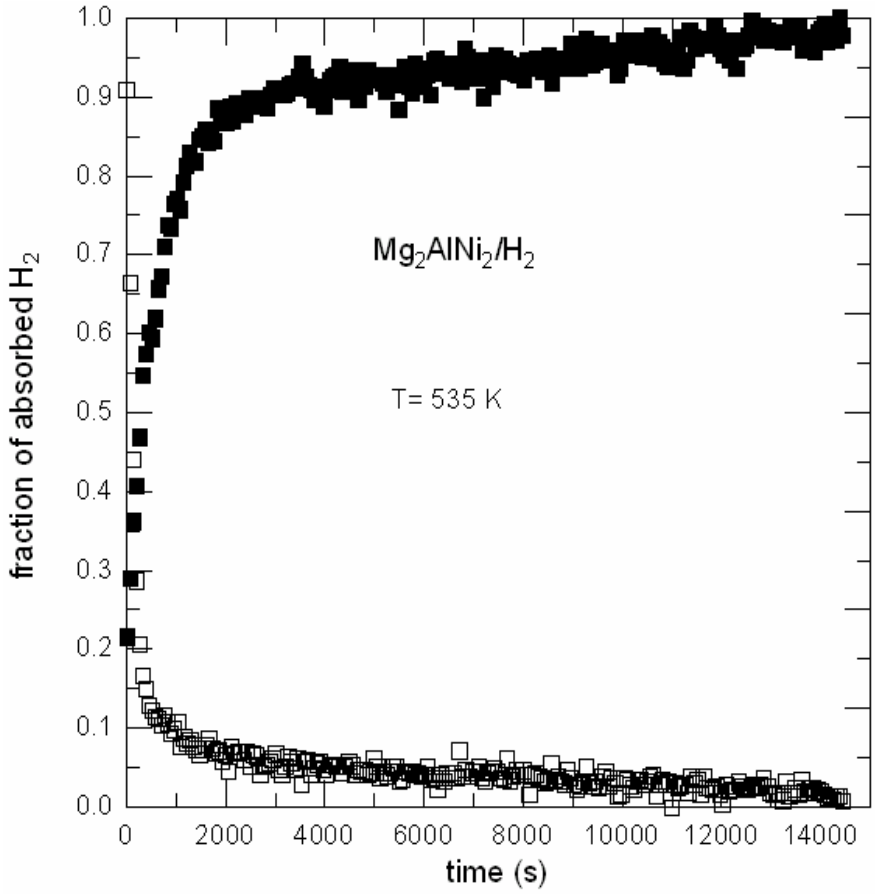

Figure 2.7: Kinetics of hydrogen absorption and desorption (full and open symbols) of Mg_2AlNi_2 at 535 K.

orption reactions at T=535 K. The degree of reaction advancement in each case is plotted vs. time in Fig. 2.7; the absorption and desorption pressures were 0.4 and 0.1 MPa, as at T= 531 K. Both processes are characterized by a first fast step, followed by a quite slower step with quasi-linear behaviours. In the case of hydrogenation, the fast step lasts about 1500 s for 85% completion of the reaction, with an average rate of $5.7 \cdot 10^{-4}$ s^{-1}. Much shorter and faster is the first stage of dehydrogenation, with 90% of the process completed in 800 s (average rate of $1.1 \cdot 10^{-3}$ s^{-1}). The second steps have rates of $1.1 \cdot 10^{-5}$ and of $7.0 \cdot 10^{-6}$ s^{-1} for the absorption and desorption processes, respectively.

An XRD analysis of the hydrogenated sample gave the pattern shown in Fig. 2.8. Both the Mg_2NiH_4 and (tetragonal) α-MgH_2 hydrides are present, and they appear to be the only phases responsible for the hydrogen absorption and desorption processes. Further, α phase with p-BCC structure and a lattice

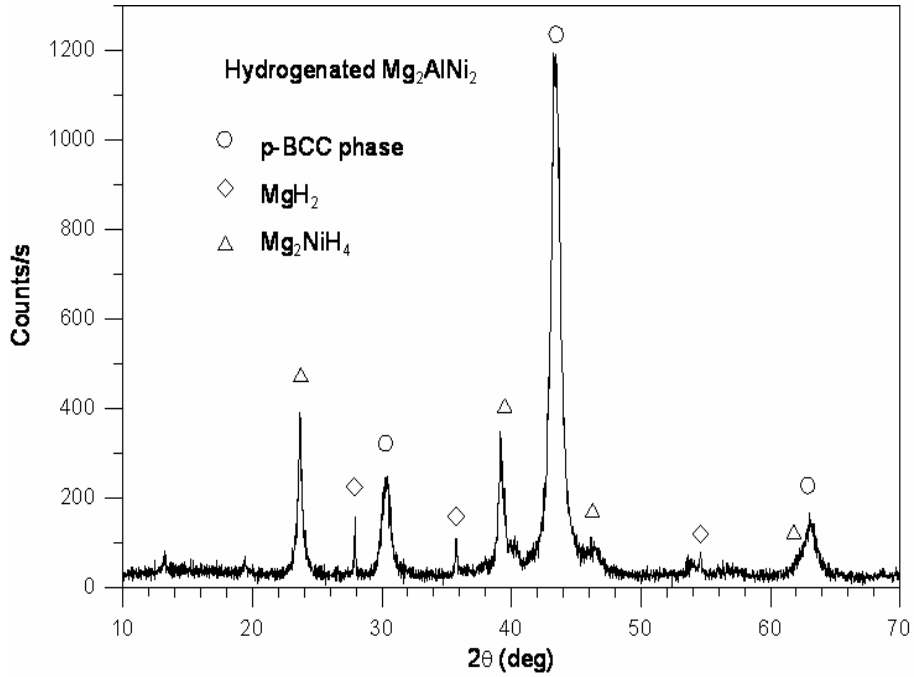

Figure 2.8: Powder XRD pattern (CuKα radiation) of the Mg_2AlNi_2 hydrogenated sample.

constant of a= 2.944 Å is left in considerable amount in the reacted material. A few very weak other peaks of uncertain identification are also observed in the XRD pattern. Thus, the Mg_2AlNi_2 alloy turns out to be decomposed by hydrogen, according to a reaction which may be plausibly guessed as follows:

$$2Mg_2AlNi_2 + 3H_2 \rightarrow 2Mg_2NiH_4 + MgH_2 + 2Mg_{0.5}AlNi_{1.5} \ . \qquad (2.2)$$

This scheme corresponds to a theoretical absorption of 1.5 wt% of H_2, not far from the observed value, and it is consistent with the semi-quantitative phase composition shown by the diffractogram. In particular, the p-BCC phase in the reacted material must be depleted of Mg and Ni with respect to the initial alloy, corresponding to a $Mg_{0.5}AlNi_{1.5}$ composition in order to match the required stoichiometry. A slight decrease of the full width at half-maximum of the (100) Bragg peak is observed, with respect to the original alloy, indicating a particle size of about 15 nm.

On repeated cycling of hydrogenation/dehydrogenation, the original p-BCC solid solution with Mg_2AlNi_2 composition is not formed any more, but the MgH_2 and Mg_2NiH_4 hydrides only are involved in the process. This is proved by the fact that XRD patterns of the dehydrogenated samples always show significant amounts of Mg_2Ni and Mg, consistent with the following reaction :

$$Mg_2NiH_4 + MgH_2 + 2Mg_{0.5}AlNi_{1.5} \leftrightarrow Mg_2Ni + Mg + 2Mg_{0.5}AlNi_{1.5} + 3H_2 \ . \quad (2.3)$$

The very fine dispersion of the MgH_2 and Mg_2NiH_4 particles in the nanosized p-BCC matrix with presumed $Mg_{0.5}AlNi_{1.5}$ composition is likely to be responsible for the low temperature of hydrogen release.

2.5 Conclusions

Mechanical alloying by ball milling in a wide compositional range of the Mg-Al-Ni system was shown to produce a nanocrystalline solid solution with $Pm\bar{3}m$ cubic symmetry. The solid solution is partially ordered over the two independent sites of the CsCl-type structure, according to the presence of weak hkl reflections with odd h+k+l values violating the $Im\bar{3}m$ symmetry (BCC). The two sites have (Mg,Al) and (Mg,Al,Ni) atomic occupations, respectively. These results confirm and generalize the previously reported ball milling synthesis of CsCl-type phases for the $MgAlNi_2$ [36] and Mg_3AlNi_2 [11] particular compositions, belonging to the presently explored range. By production of new metastable phases with nanosized particles in metallic systems, access may be given to novel alloys with interesting properties which can not be obtained by equilibrium thermodynamics methods. This holds particularly for the hydrogen storage application.

Within the pseudo-BCC synthesized ternary alloys, the sample with Mg_2AlNi_2 composition proved to react with hydrogen forming a mixture of the MgH_2 and Mg_2NiH_4 hydrides with a Mg-poorer p-BCC solid solution. About 1.4 wt% of H_2 is absorbed/desorbed reversibly for several cycles; hydrogen can be extracted at 531 K at a pressure not smaller than 0.1 MPa. Although the quantity of stored hydrogen is limited, the temperature of release at $p \geq 0.1$ MPa is significantly lower than for pure MgH_2, and also favourable with respect to Mg_2NiH_4. This indicates that appreciable improvements in the dehydrogenation process of Mg-alloy hydrides can be achieved, by producing the hydride in a convenient chemical-physical environment. The contribution of interface free energy may be responsible for the modified hydrogenation response of nanosized systems dispersed in a heterogeneous matrix.

The result of this par has already been published [2].

Part II

Complex hydrides

Chapter 3

Chemical synthesis

3.1 Introduction

In the search of new hydrogen storage materials, complex hydrides and especially light metal borohydrides have attracted a great deal of attention in the last years due to their large gravimetric hydrogen densities [38]. Furthermore, according to theoretical modelling some have thermodynamic properties that allow operation near ambient conditions, one example is $Mg(BH_4)_2$ [34, 50]. Recently, a major focus has been on alkaline and alkaline-earth metal based borohydrides, such as $LiBH_4$, $Mg(BH_4)_2$ and $Ca(BH_4)_2$. Some proposed decomposition reactions show the following hydrogen capacities:

$$LiBH_4 \rightarrow LiH + B + 3/2H_2 \qquad 13.9\text{wt}\%H_2 \tag{3.1}$$

$$Ca(BH_4)_2 \rightarrow 1/3CaB_6 + 2/3CaH_2 + 3H_2 \qquad 9.6\text{wt}\%H_2 \tag{3.2}$$

$$Mg(BH_4)_2 \rightarrow MgB_2 + 4H_2 \qquad 14.9\text{wt}\%H_2 \tag{3.3}$$

However, the dehydrogenation of these compounds proceeds via several steps, intermediate phases are present, and there are kinetic limitations and/or competing side reactions. $LiBH_4$ [39] and $Ca(BH_4)_2$ [19] are partially reversible, and reversibility in $Mg(BH_4)_2$ [23] has only been found for extreme pressure and temperature conditions. Moreover, practical utilization of these compounds for hydrogen storage applications seems challenging due to their high decomposition temperatures. Hence, intensive research efforts are carried out in order to improve the kinetic and thermodynamic properties. For instance, the design of solid state reaction systems like MBH_4-M'H_x has proven to be a powerful tool for improving the thermodynamic properties [6]. Numerous approaches have also been performed in order to improve the kinetic properties such as the addition of dopants and/or confinement of the complex hydride in nano-porous scaffolds

[9]. Recently, it has been proposed that mixed-metal borohydrides based on alkaline and selected transition metals could have acceptable thermodynamics for reversible hydrogen storage and still maintain a high hydrogen capacity [24]. Some examples of MM'$(BH_4)_n$ have already been reported [14, 18]. Additionally, first reports on bialkaline borohydrides, such as $LiK(BH_4)_2$ [55, 35] and $NaK(BH_4)_2$ [47] have been published. The formation of a dual-cation borohydride has also been proposed for the 1:1 $LiBH_4/Mg(BH_4)_2$ mixture [9]. In the case of the pseudo-binary system $LiBH_4$–$Ca(BH_4)_2$, the borohydrides exist as a physical mixture of the constituent phases exhibiting an eutectic melting at ca. 200 °C and even a partial reversibility has been confirmed for the first time in the case of a mixed borohydride composite [22].

Our current approach focuses on the mixed lithium-magnesium borohydride system. The theoretical hydrogen capacity of this system might be calculated by the combination of the decomposition reactions of the single borohydrides as follows:

$$LiBH_4 + Mg(BH_4)_2 \rightarrow LiH + B + MgB_2 + 11/2H_2 \qquad 14.6\text{wt\% H2} \qquad (3.4)$$

The aim of this study is to elucidate the possible formation of a mixed-metal borohydride, such as $Li_{1-x}Mg_{1-y}(BH_4)_{3-x-2y}$ [12], a solid solution or a physical mixture of the components with an eutectic melting as in the case of $LiBH_4$-$Ca(BH_4)_2$ [13]. Therefore, several composites, such as $x$$LiBH_4$–(1-$x$)$Mg(BH_4)_2$, have been synthesized and investigated. Second, due to the high hydrogen capacity of this system, this material can be a good candidate for hydrogen storage applications. Consequently, the thermodynamic and kinetic properties of the formed system have also been studied.

3.2 Handling and chemical synthesis operations

Reagents and products involved in the synthesis are extremely reactive to water and oxygen due to the presence of $[BH_4]^-$ group, a strongly reducing agent. These molecules should not be exposed to air and have to be conserved and handled under controlled atmosphere inside an argon loaded glove box.

During the work two different types of glove box have been used for storing and manipulating the materials; one box is a simple Plexiglas glove-box with one medium size load lock; this system has an internal double filtering system consisting of a forced circulation inside microporous zeolites and silica gel containers which had to be periodically renewed.

The absence of an electronic sensor for monitoring the amount of oxygen and water forced us to simply let inside the glove box an open glass container with phosphorus pentoxide, P_2O_5, the anhydride of phosphoric acid, which is a

white crystalline solid and is used ad powerful desiccant according to the reaction

$$P_4O_{10} + 6\ H_2O \rightarrow 4H_3PO_4 \tag{3.5}$$

although its utility for drying is limited by its tendency to form a protective viscous coating that inhibits further hydration by unspent material and that has to be periodically removed.

The second type of glove box is a fully automated M-Brown system with external Cu-CuO filter equipped with sensors monitoring the oxigen and water: the level of oxygen was kept below 3 ppm and water below 1 ppm.

All the solid materials were held inside sealed bottles and exposed to the glove box environment – for the strictly necessary time – only after evaluating the good quality of the atmosphere of the glove box. Solid reagents were usually taken out of the glove box sealed inside the same lab bottles were the reaction should take place.

In case the presence of an excess of oxidizing molecules in the glove box environment allowed them to enter in contact with the samples during the loading inside XRD and Raman sealed sample holder, the consequence was an unexpected slow decomposition reaction during the measurements which slowly creates a second or third phase, reduces the crystallinity of the samples degrading the quality of the harvested data in term of signal/noise ratio. The phase evolution caused by contact with air of $LiBH_4$ has been studied by mean of XRD by Mosegaard *et al.*[33].

Every operation involving dissolving, stirring, filtering, heating or drying of the reagents had to be carried out under inert atmosphere inside purged and vacuum grease sealed lab glassware. These sealed glassware had always to be connected through gummy tubes to a *vacuum/inert gas* line: the presence of two independent valves separating the gummy tubes from vacuum and inert gas lines allows removal of air and purging with inert gas of the glassware internal volumes without any further contact with external ambient gases.

Two different *vacuum/inert gas* lines have been used; vacuum was provided by a mechanical vacuum pump reaching typically $1E^{-3}$ mbar (eventually coupled with a turbomolecular pump when higher vacuum $\tilde{1}E^{-5}$ mbar was needed to increase the efficiency of a decomposition reaction); considering the possibility of thermally treating wet products under vacuum for drying them from the solvents and eventually decompose an adduct, we had to protect the pumps with a liquid nitrogen cooled trap for condensing the solvents vapors. Despite this solution a periodic maintenance of the pumps was needed. Argon or nitrogen were used as

inert gas. Argon (quality 5.0, minimum purity 99.999%, total hydrocarbons ≤ 0.2 ppm, $O_2 \leq 2$ ppm, $H_2O \leq 3$ ppm) was purchased in stainless steel cylinders and directly connected to the gas line; gaseous nitrogen from evaporation of liquid nitrogen was dried over a molecular sieve - potassium chloride filter before letting it flowing into the inert gas line. The gas line itself has a mercury gas valve that allows overpressure to be released before forcing the grease joints of the glassware.

Every glass bottle, condenser and filtering tools had to be equipped with a valve allowing to be connected to a vacuum/Ar line; purging operations always had to be done after the assembling and before the final connection of the glassware with the lab bottles containing the reagents which had to be treated.

It was necessary to use absolutely water free solvents; the usual way for reaching the requested purity grade is distillating the solvents after boiling over sodium for few hours.

We used *puriss., absolute* grade solvent from Sigma Aldrich (assay 99.5%) over molecular sieve ($H_2O = 0.01\%$) inside bottles sealed with gummy crown cap under the standard external plastic cap, allowing us to use the solvents diethyl ether (DEE), methyl tert-butyl ether (MTBE) and 1,4-dioxane as received. Lithium tetrahydroborate (96%, Sigma Aldrich and 95%, Merck), magnesium chloride (98%, Sigma Aldrich), magnesium hydride (99%, Sigma Aldrich), lithium hydride (99%, Sigma Aldrich) were used as received. Borane triethylamine complex (97%, Sigma Aldrich) was degassed using the pump–thaw technique.

The solvents have been transfered from the commercial bottles to the round-bottomed flasks (where the reactions were taking place) using a double ended needle. An argon overpressure was created inside the commercial bottle through the gummy membrane of the crown cap using a standard needle fitted on one argon line; the destination bottle was prepared with a valve on one neck and a glass cap on the other, connected through the valve to a vacuum/Ar line; if necessary, then internal atmosphere was removed and substituted with argon, repeating the process 3 times and filled again with argon; the glass cup was removed without decreasing the argon overpressure on the bottle and a gummy cup was placed on the open neck; a 110 cm long stainless steel double ended needle was inserted on the commercial bottle without reaching the solvent level and letting only argon flowing away removing the air inside the needle; the internal part of the needle was then washed dipping the end into the solvent and letting some drops flowing through the needle pushed by the pressure; after few minutes the free end of the needle was inserted into the gummy cap of the destination bottle, then the over pressure there was reduced letting the solvent being transfered with almost no contact with air.

Dissolution trough stirring and heating at reflux temperature of suspension

into different low boiling point solvents has been carried out using an oil bath and a water cooled condenser connected to the Ar line and to the mercury gas valve for allowing partial pressure increase due to evaporation and avoiding external gases to enter in contact with the reaction environment during vapor condensation.

Separation of solid part of the suspension from the liquid part in controlled atmosphere was managed either letting the solid part depositing and removing the upper liquid part with a syringe or filtering the solid on a glass filter inside a sealed glass cylinder. In this case the hourglass technique has been used: the glass filter cylinder with an empty lab bottle have been mounted upside down on the bottle containing the suspension, then the whole system has been turned over letting the liquid flowing through the filter for gravity.

Removal of the solvent was usually carried out at high temperature and ambient pressure with a Claisen condenser; this way of operating avoid the solvent crystallization when it cools down as consequence of the evaporation heat removal effect.

Drying of the adduct was obtained evacuating the inert gas and the residual solvent vapor inside the bottles during heating in oil bath or inside a Buchi laboratory rotating dryer. Thermal adduct decomposition usually follows a manual milling in agate mortar for reducing the grain size and increase the superficial area.

3.2.1 X-Ray Diffraction

XRD patterns of synthesized powder materials were obtained using a Bruker *D8 Advance* equippend with point detector and Philips *X'PERT* diffractometers with position sensitive detector. In both cases they were used in Bragg-Brentano θ-θ geometry and a copper anode tube as X-ray source were employed with single crystal monochromator to select only Kα radiation.

Were used a step scan of 0.02 and integration time was 8 sec/step (*D8*) or 100 sec/step (*X'PERT*).

In-situ XRD studies were performed with the *X'PERT* instrument under a He flow using a HTK 1200 sample holder made by Anton Paar GmbH. The samples were heated from room temperature to 150 °C and temperature was increased stepwise. The data were taken every 5 °C between 150 °C and 180 °C. The measuring time at each temperature step was approximately 1 hour.

The powder was spread on a silicon single crystal and sealed in a glove box by an airtight hood of Kapton foil. Although Kapton reduces the X-ray intensity on the sample and reaching the detector, this reduction is uniform due to the shape

of the hood; being out of the geometry focus he do not add any extra peak to the XRD patterns.

3.2.2 Ball milling

Pre-milling of reagents for wet chemical syntheses and dry mechanochemical syntheses was performed by a Fritsch *P6* planetary mill at 600 rpm using an 80 ml vial and silicon nitride balls or by a Retsch *PM100* planetary mill at 400 rpm using an 50 ml vial and 10 mm diameter zirconium oxide balls. The vials were filled and sealed in the glove box; the ball-to-powder ratio always was 20 : 1.

Mixtures of xLiBH$_4$ and (1-x)Mg(BH$_4$)$_2$ were prepared by ball milling the starting compounds in a Fritsch P6 planetary mill. Each mixture of Mg(BH$_4$)$_2$ and LiBH$_4$ (1 g of material) was charged together with thirteen 10 mm diameter tungsten carbide balls into a vial of the same material under an argon atmosphere. The ball-to-powder ratio was approximately 100:1. The milling was performed at 600 rpm for 4h.

3.2.3 Thermal analysis

High-pressure differential scanning calorimetry (HP-DSC) was performed by using a Netzsch *DSC 204 HP* apparatus (Netzsch, Germany) placed inside an argon-filled glove box with partial pressures of oxygen and water below 1 ppm. The samples were measured by using Al_2O_3 crucibles and Al_2O_3 lids at 5 bar H_2 and at a heating rate of 5 °C/min between room temperature and 500 °C.

Al_2O_3 crucibles were inserted inside a Al crucible for avoiding that the liquid phase which is present after the melting temperature of the sample could impregnate the porous alumina and drip out inside the DSC system. The same procedure had to be applied both to sample crucible and reference crucible. The optimal heat transfer between Al_2O_3 and Al surfaces was guaranteed by the correct fitting of the crucibles and checked by reference runs used for subtracting the instrumental contributions from the acquired DSC profiles.

Simultaneous thermogravimetric analysis, differential scanning calorimetry and mass spectrometry (TG-DSC-MS) was carried out on a *Sensys Evo* TG-DSC apparatus (Setaram, France) coupled with an *OmniStar* mass spectrometer (Pfeiffer, Germany) for the analysis of the evolved gas. The TG-DSC-MS measurements were performed under a gas flow of 20 ml He/min and a heating rate of 5 °C/min using open platinum crucibles. The visual determination of the melting point was carried out by using a Büchi Melting Point *B-540* apparatus.

3.2.4 Elemental analysis

Elemental analysis of carbon, nitrogen and hydrogen was performed with CE Instruments Flash EA 1112 series analyzer using He as the purge gas. The typical amount of the sample was 1-3 mg.

Elemental analysis of lithium was performed by atomic absorption spectrometry (AA) with AAnalyst 200 by Perkin Elmer Instruments (sample aspirated and ionized by methane flame). Calibration solutions were prepared from a 100 ppm Li^+ solution obtained by dissolution of lithium carbonate (99.4%, Sigma Aldrich) after drying in furnace (2 days at 130 °C).

Elemental analysis of magnesium was performed by inductively coupled plasma emission spectroscopy (ICP) with Instruments SA, Jobin-Yvon 38 Sequential (France). Calibration solutions were prepared from *Magnesium Standard for AAS* (1000 ppm, Fluka Analytical).

A diluted aqueous solution of the boronhydride with HNO_3 (2%) with a typical nominal concentration of magnesium and lithium of 3 ppm was prepared and analyzed.

3.3 Synthesis procedures

Various procedures based on mechanochemical and wet chemical syntheses were used for trying to synthesize the expected compound.

These procedures can be divided in *direct synthesis* reactions and *metathesis reactions* (involving ionic exchange).

Ionic exchange procedures have been performed both with dry mechanochemical reactions through ball milling and by liquid phase dissolution in organic solvents.

3.3.1 Direct synthesis

Chlopek *et al.*[7] proposed a *direct synthesis* procedure for preparing $Mg(BH_4)_2$ based on a proposition made by Koester *et al.*[20]. This procedure has been used during present work (synthesis n. **5**, **11**, **12**) for synthesizing $Mg(BH_4)_2$ and consists in the reaction of triethylamine borane complex with magnesium hydride according to

$$2\mathrm{TMA{\cdot}BH_3} + \mathrm{MgH_2} \rightarrow (\mathrm{TMA})_n{\cdot}\mathrm{Mg(BH_4)_2} \tag{3.6}$$

synthesis n°	expected composition Li:Mg	technique	procedure steps
1	1:1	dry metathesis	ball milling
2	1:1	dry metathesis	ball milling, recrystallization
3	1:1	dry metathesis	dissolution, recrystallization
4	1:1	direct synt.	ball milling, recrystallization
5	$Mg(BH_4)_2$	direct synt.	(without recrystallization)
6(a,b,c)	1:1	wet synthesis	dissolution in Et_2O
7	1:1	wet synthesis	dissolution in Et_2O, recrystallization
8	1:1	wet synthesis	dissolution in dioxane
9	2:1	wet synthesis	dissolution in Et_2O
10	2:1	wet synthesis	dissolution in dioxane
11	$Mg(BH_4)_2$	direct synt.	(without recrystallization)
12	$Mg(BH_4)_2$	direct synt.	(without recrystallization)
13(a,b)	1:1	wet synthesis	dissolution in MTBE
14	2:1	wet synthesis	dissolution in dioxane
15	4:1(1)	wet synthesis	dissolution in dioxane
16	1:1	dry synthesis	ball milling
17	2.2:1(1)	wet synthesis	dissolution in dioxane
18 (INT1)	2:1	wet synthesis	dissolution in dioxane
19	various	dry synthesis	ball milling

Table 3.1: Synthesis list; (1)=effective composition verified with ICP/AAS; expected was 2:1.

The MgH_2 has to be pre-milled in a ball mill under argon atmosphere and transfered into a lab bottle together with triethylamine borane complex, which is liquid at ambient temperature and acts as solvent. The light gray mixture has to be heated under reflux at 100 °C for one hour with vigorous stirring, then afterwards at 145 °C for another six hours. After this time the liquid mixture separates an immiscible dark gray liquid phase with lower density which solidify during cooling down to room temperature. The solid has to be crushed, finely ground, stirred with *n*-hexane, then washed with *n*-hexane (3 x 30 ml) and dried under vacuum. The solid obtained in this way is a triethylamine adduct of magnesium borohydride which has to be decomposed for a total of 17 h at various stages [100 °C/1 h; 130 °C/1 h; 170 °C/3 h; and 160 °C/12 h under vacuum (p $\approx$ 1 x 10^{-3} mbar)] for obtaining the solvent-free product.

In this work a similar procedure was used (synthesis n. **4**) adding triethylamine borane complex to the stoichiometric mixture of LiH and MgH_2 according

to the expected 1:1 Li:Mg molar ratio

$$3\text{TMA}\cdot\text{BH}_3 + \text{MgH}_2 + \text{LiH} \rightarrow (\text{TMA})_n\cdot\text{LiMg}(\text{BH}_4)_3 \tag{3.7}$$

After the thermal treatment the mixture showed the presence of a second phase with high viscosity and higher density which was washed with n-hexane (4 x 30 ml), then decomposed for a total of 17 h.

3.3.2 Metathesis reactions: ball milling and crystallization

A common method to synthesize complex hydrides is the reaction of a halide with a tetrahydroaluminate or tetrahydroborate, whereby the anions are exchanged and the new compounds precipitate. For the preparation of $\text{Mg}(\text{BH}_4)_2$, Chlopek *et al.*[7] proposed the following method:

$$\text{MgCl}_2 + 2\text{MBH}_4 \rightarrow \text{Mg}(\text{BH}_4)_2 + 2\text{MCl} \tag{3.8}$$

with M = Li, Na.

Several *metathetical syntheses* based on wet chemical and dry mechanochemical methods were tried, and the products were investigated.

In literature a mechanochemical preparation for $\text{LiMg}(\text{AlH}_4)_3$ is reported by M. Mamatha *et al.*[29] starting from LiAlH4 and MgCl2 (16.0 mmol and 5.25 mmol respectively) ball milled for 3 hours in a Retsch ball mill 200MM (30 Hz, 25 ml milling vial and two steel milling balls of 6.3 g each). The product of this synthesis was a mixture of $\text{LiMg}(\text{AlH}_4)_3$ + 2LiCl and $\text{LiMg}(\text{AlH}_4)_3$ was then separated by LiCl; the mixture was suspended in 150 ml of Et_2O and extracted for several days using a Soxhlet apparatus, which led to crystallization of the $\text{Mg}(\text{AlH}_4)_2\cdot\text{Et}_2\text{O}$ adduct from the solvent. The solvent was evaporated and the solid Mg(AlH4)2·Et2O heated under vacuum to 60°C for 10 h in two stages (3–4 h to 40°C; 6 h to 60°C).

A similar procedure was used also by H. Grove *et al.*[13] for the preparation of $\text{LiMg}(\text{AlD}_4)_3$ for structure determination through neutron diffraction. Reagents were ball milled according to the reaction

$$3\text{LiAlD}_4 + \text{MgCl}_2 \rightarrow \text{LiMg}(\text{AlD}_4)_3 + 2\text{LiCl}. \tag{3.9}$$

The product diffracted poorly and recrystallization was performed to remove Al and the by-product LiCl using Et_2O for the dissolution of the compound and toluene for precipitation. The result was an highly crystalline product containing about 10 wt% LiCl.

In this work the same procedure was used for trying the preparation of $LiMg(BH_4)_3$ (synthesis **1-3**):

$$3LiBH_4 + MgCl_2 \rightarrow LiMg(BH_4)_3 + 2LiCl. \tag{3.10}$$

The reagents $LiBH_4$ and $MgCl_2$ (18.7 mmol and 6.23 mmol respectively) were ball milled for 18 hours in a Retsch ball mill PM100 (300 rpm, 50 ml ZrO_2 milling vial and 10 ZrO_2 milling balls of 3.1 g each, BPR=30, inversion of rotating direction every 30 minutes). Recrystallization was performed: the solid was transfered in a two neck round-bottomed flasks and Et_2O was added. The suspension was stirred for 24 h at a high rate. Insoluble grey powder was removed by filtration and 230 ml toluene was added to the filtrate. The solution was placed in an oil bath at 80°C, and a white precipitate was observed. The distillation was continued until all toluene was removed. The powder was dried at 70°C for 3 h.
In particular, synthesis n. **1** did not involved a recrystallization in toluene and in n. **3** the reagents have'n been ball milled.

3.3.3 Synthesis reactions: mechanochemical

For avoiding the presence of sub-product LiCl which could not be totally removed by recrystallization of the product and for avoiding a residual presence of solvent as an adduct, a dry synthesis reaction from single borohydrides was tried according to

$$LiBH_4 + Mg(BH_4)_2 \rightarrow LiMg(BH_4)_3. \tag{3.11}$$

In synthesis n. **16** the reagents $LiBH_4$ and $Mg(BH_4)_2$ in equal molar amount (2.64 mmol, corresponding to 0.057 g and 0.142 g respectively) were ball milled for 4 hours in a Retsch ball mill PM100 (200 rpm, 50 ml ZrO_2 milling vial and 10 ZrO_2 milling balls of 3.1 g each, BPR=150, inversion of rotating direction every 15 minutes).
The milling parameters have been chosen after a test where 0.24 g of $LiBH_4$ was ball milled in the same vial for different period and speed (0.5, 1, 2, 4 hours at 200 rpm and 1 h at 300 rpm) for evaluating the structure degradation of lithium borohydride by mean of XRD measurements of the milled sample.

In synthesis n. **19** mixtures of $x LiBH_4$ and (1-x)$Mg(BH_4)_2$ were prepared by ball milling the starting components with different molar ratio of $x/(1-x)$, with x = 0, 0.10, 0.25, 0.33, 0.40, 0.50, 0.60, 0.66, 0.75, 0.80, 0.90, 1.

3.3.4 Synthesis reactions: dissolution

The same reaction (3.11) was supposed to take place in liquid solution of the reagents (synthesis n. **6-10** and **13-15**). Three solvents have been tried:

diethyl ether, methyl tert-butyl ether and 1,4-dioxane. The procedure involved the stirring at hight rate at reflux temperature of the solvent typically for 24 hours the stoichiometric amount of $LiBH_4$ and $Mg(BH_4)_2$ (according to Li/Mg ratio 1:1 or 1:2). Then a remaining solid part was removed by filtration and the solvent was distilled from the filtrate at low pressure and room temperature. The product was finally dried under vacuum at the solvent's boiling temperature.

Due to the high affinity of ether group with the $[BH_4]^-$ ions the products consisted in an adduct whose presence was confirmed by XRD and raman analysis. A product with solvent-free XRD pattern and raman spectra was obtained after a thermal treatment (8 hour at 170°C, 1E-4 mBar).

Effective Li:Mg ratio of the product was checked in synt. **15** by mean of ICP/AAS measurements and it resulted to be 4:1 due to the removal by filtration of an undissolved solid part.

A better control on the stoichiometry was obtained in synt. **17** by preparing two different limpid solution of the single borohydride adding 375 ml of dioxane to 0.263 g of $LiBH_4$ and 0.625 ml to 0.300 g $Mg(BH_4)_2$. The undissolved part was removed by filtration and weighted for calculated the effective borohydride concentration.
Then the right amount of solution was mixed according to the formula $LiMgB_3H_{12}$, then the solvent was remove and the adduct was decomposed by thermal treatment (1 hour at 160°C, 1E-4 mBar, 12 hours at 170°C, 1E-3 mBar). The effective stoichiometry was 2.2:1.

The same synthesis with Li:Mg ratio 2:1 was repeated by INT laboratories using high purity magnesium borohydride produced there (synt. **18**). The stoichiometric amount of lithium borohydride (0.0446 g corresponding to 2.05 mmol) and magnesium borohydride (0.0553 g corresponding to 1.025 mmol) has been dissolved in 0.37 L of dioxane under stirring at reflux temperature for 12 hours; then the solvent has been removed and the product has been dryed under vacuum ar ambient temperature and thermally treated (1 hour at 160°C, 1E-3 mBar, 5 hours at 160°C, 1E-3 mBar).

Chapter 4

Material characterization

4.1 X-Ray diffraction

4.1.1 $LiBH_4$-$Mg(BH_4)_2$ mixture

Figure 4.1d shows the XRD pattern of the composite obtained after ball milling the starting materials, namely o-$LiBH_4$ and α-$Mg(BH_4)_2$ at 1:1 molar ratio. For comparison, the XRD patterns of the starting materials are shown in fig. 4.1a-c. Some reflections can be assigned to the constituent phases but the low crystallinity of the sample prevents a full characterization of the pattern. In order to gain an insight into the material the sample was annealed for 12h at 200 °C.

During heating, the diffraction peaks gained intensity and additional reflections became detectable in the XRD pattern at room temperature (Figure 4.1e). All observed peaks have been assigned either to the orthorhombic phase of $LiBH_4$ or to a polymorph of $Mg(BH_4)_2$ (alpha and/or beta phase), slightly shifted to lower angles. Since no new peak could be found, the components are existing as a physical mixture rather than a new compound, for example $Li_{1-x}Mg_{1-y}(BH_4)_{3-x-2y}$ as was proposed by Fang *et al.*[9] Moreover, the reaction of o-$LiBH_4$ and β-$Mg(BH_4)_2$ at 1:1 molar ratio leads to a similar XRD pattern suggesting that by milling the high temperature modification of $Mg(BH_4)_2$ in the presence of $LiBH_44$, both low temperature modifications can be formed again. This is surprising since the α to β transformation in pure $Mg(BH_4)_2$ is known to be (thermally) non-reversible. Similarly, Lee *et al.*[22] have reported that milling $LiBH_4$ with β-$Ca(BH_4)_2$ results in a physical mixture of the components, concretely, $LiBH_4$ with α-$Ca(BH_4)_2$ and γ-$Ca(BH_4)_2$ whereas β-$Ca(BH_4)_2$ could not be detected any longer in the physical mixture at room temperature.

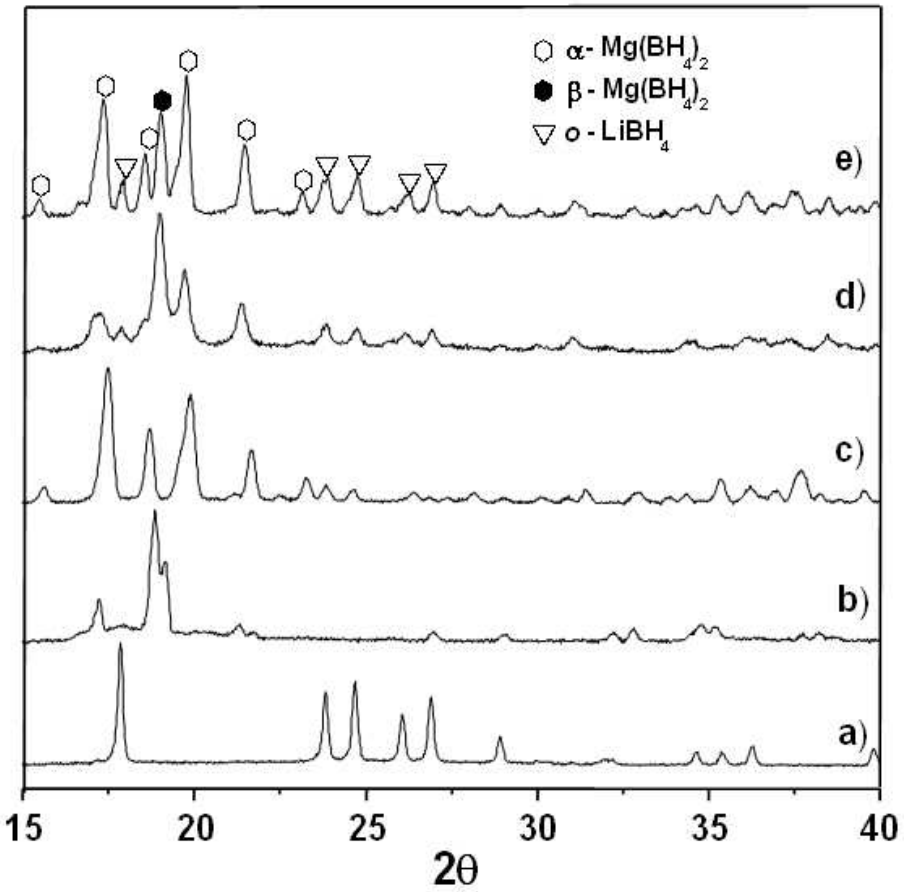

Figure 4.1: XRD patterns of (a) as-milled $LiBH_4$, (b) as-synthesized β-$Mg(BH_4)_2$, (c) as synthesized α-$Mg(BH_4)_2$, (d) as-milled $LiBH_4$-$Mg(BH_4)_2$, (e) as-annealed $LiBH_4$-$Mg(BH_4)_2$.

4.1.2 xLiBH$_4$-(1-x)Mg(BH$_4$)$_2$ composite

In order to determine a potential eutectic composition of the physical mixture, different composites of the starting borohydrides (in the low temperature modification) were synthesized and investigated. In figure 4.2 the XRD patterns of ten composites (namely, x = 0.10, 0.25, 0.33, 0.40, 0.50, 0.60, 0.66, 0.75, 0.80, 0.90) are plotted. Likewise, the diffraction patterns of the milled starting materials are shown for comparison.

All reflections can be assigned to polymorphs of $LiBH_4$ or $Mg(BH_4)_2$ and no diffraction peaks corresponding to a new phase could be detected. The pure lithium and magnesium borohydride (Figure 4.2a and l) show the reflections corresponding to the low- and the high-temperature modifications, respectively, since the polymorphic transformation of magnesium borohydride from alpha to

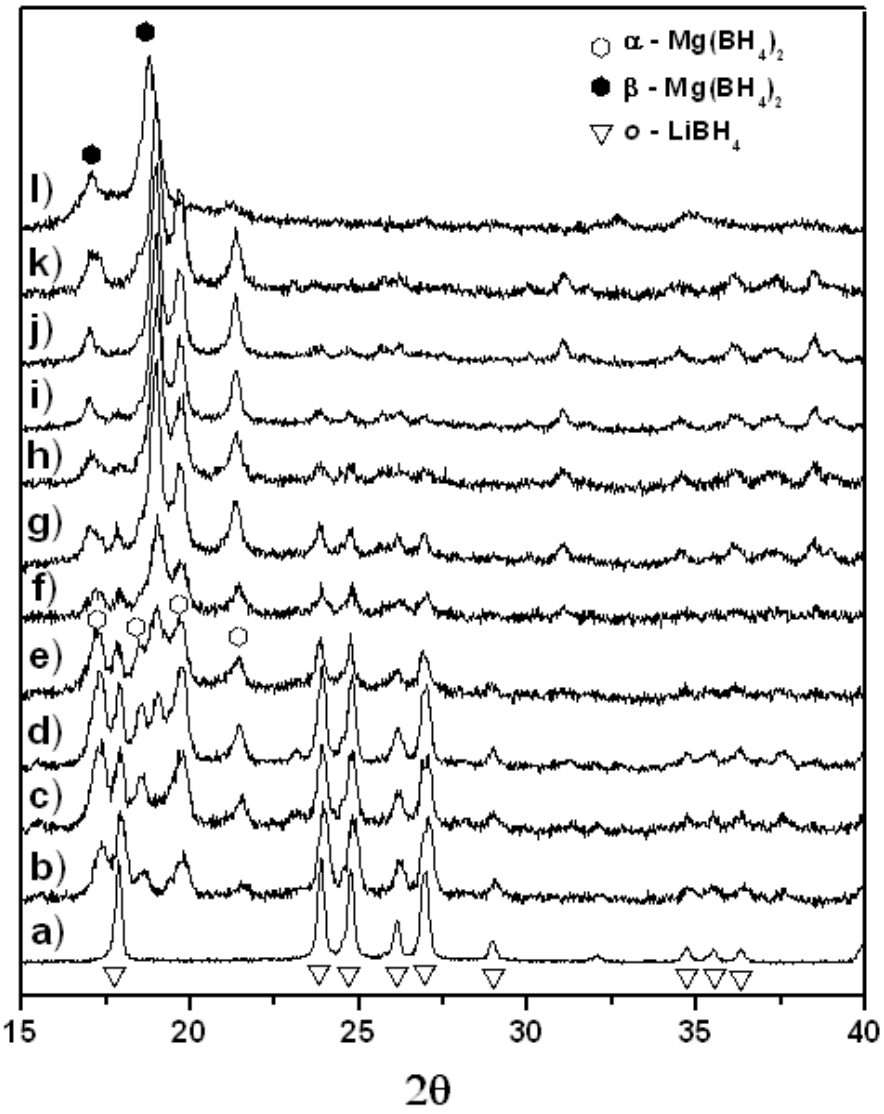

Figure 4.2: XRD patterns of the xLiBH$_4$–(1-x)Mg(BH$_4$)$_2$ composites with (a) x = 1, (b) x = 0.90, (c) x = 0.80, (d) x = 0.75, (e) x = 0.66, (f) x = 0.60, (g) x = 0.50, (h) x = 0.40, (i) x = 0.33, (j) x = 0.25, (k) x = 0.10 and (l) x = 0, respectively. On the top as-synthesized α-Mg(BH$_4$)$_2$.

beta already takes place during milling. In contrast, the composites consisted of a mixture of alpha- and beta-phase depending on the molar ratio of the starting materials. The composites with major amount of LiBH$_4$ (0.60 = x = 0.90, Figure 4.2b–f) showed alpha as the major phase of Mg(BH$_4$)$_2$, while the composites with minor amount of LiBH$_4$ (0.10 = x = 0.40, Figure 4.2h–k) show beta as the major phase. Interestingly, similar diffraction patterns were observed for compos-

ites synthesized with β-$Mg(BH_4)_2$ as starting material. Therefore, these results suggest that $LiBH_4$ makes $\alpha - \beta$ transition reversible. Since this polymorphic transformation becomes reversible, the presence $LiBH_4$ affects either the kinetics of the polymorphic transition in $Mg(BH_4)_2$ or it thermodynamically stabilizes the alpha phase or both.

Calculations on the two phases have shown that, including the electronic total energy and the lattice vibrational total energy, the alpha phase is the more stable one at all temperatures [53]. The beta phase, however, contains long-range disorder that leads to additional entropic contributions [53, 15]. Since the difference between the calculated total energies is small, ¡ 0.1eV/f.u., these entropic contributions can easily cause the beta phase to become the stable phase at higher temperature. In accordance to previous interpretations [10], this leads to the conclusion that in the pure $Mg(BH_4)_2$ system the beta phase becomes quenched-stable on cooling. Our observation, that the transformation can actually be made reversible, confirms this hypothesis experimentally. To our knowledge, this is the first time that the orthorhombic phase (high temperature modification) of magnesium borohydride can be reversibly transformed in the hexagonal phase (low temperature modification).

4.2 Thermal Analysis

4.2.1 High Pressure Differential Scanning Calorimetry

The thermal behaviour of the composites has been investigated by using high pressure differential scanning calorimetry. Figure 4.3 shows the corresponding DSC profiles of the different mixtures. As shown above, the polymorphic phase transformation of $Mg(BH_4)_2$ already takes place during milling, therefore no peak can be observed below 200°C for pure milled $Mg(BH_4)_2$ (Figure 4.3 l). The DSC curves of the composites are remarkably different from those of both single borohydrides. For instance, the polymorphic transformation from orthorhombic- to hexagonal-$LiBH_4$ at 118.7 °C (Figure 4.3a) is slightly shifted for the composites ranging from 110.5 to 113.9 °C (peak 1). Additionally, the melting point peak of lithium borohydride at 288.1 °C (peak 5) can not be detected any longer. Instead, a bump (✯) was found to appear in the DSC profile of some composites, specifically when $0.66 \leq x \leq = 0.90$ (Figure 4.3b–e). This bump can be tentatively associated to an excess of $LiBH_4$ in an eutectic mixture. With increasing amount of $LiBH_4$ this bump shifts up in the temperature up to the melting point of pure $LiBH_4$ ($x = 1$). On the other side, the first decomposition signal of $Mg(BH_4)_2$ (peak 6) cannot be detected and another bump (▼) appears in the DSC profiles of composites with higher Mg content (when x = 0.25, 0.10 in Figure 4.3j, k). This bump can be tentatively associated to an excess of $Mg(BH_4)_2$ in an eutectic mixture and with increasing amount of $Mg(BH_4)_2$ this bump shifts up in

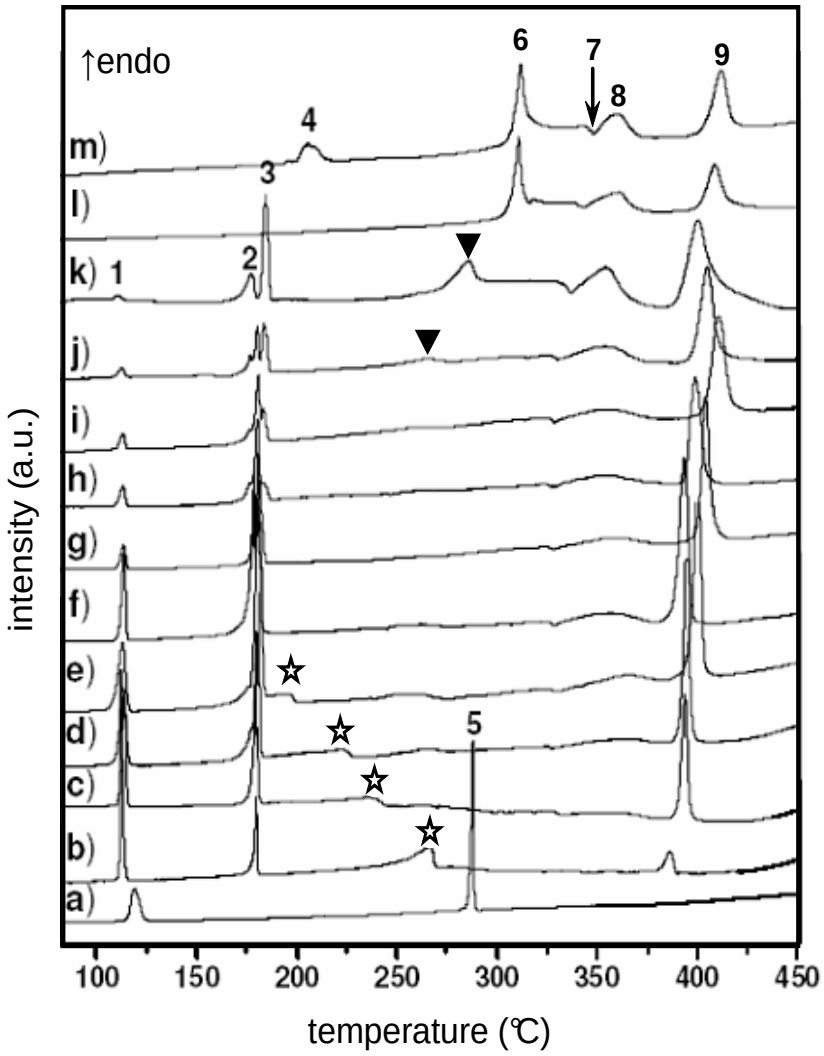

Figure 4.3: HP-DSC profiles of the xLiBH$_4$–(1-x)Mg(BH$_4$)$_2$ composites under 5 bar H_2 at a heating rate of 5 °C/min with (a) $x = 1$, (b) $x = 0.90$, (c) $x = 0.80$, (d) $x = 0.75$, (e) $x = 0.66$, (f) $x = 0.60$, (g) $x = 0.50$, (h) $x = 0.40$, (i) $x = 0.33$, (j) $x = 0.25$, (k) $x = 0.10$, (l) $x = 0$ β-Mg(BH$_4$)$_2$ and (m) $x = 0$ α-Mg(BH$_4$)$_2$ respectively.

the temperature up to the position of peak 6 of pure Mg(BH$_4$)$_2$ ($x = 0$). Peaks 6-9 are connected to pure Mg(BH$_4$)$_2$ decomposition and will be commented on section 5.3.2.

Nevertheless, all composites show an endothermic event at approximately 180 °C (peak 2). This originates from the eutectic melting of the physical mixture, as was confirmed by visual determination of the melting using a static apparatus. In addition, the composites with minor amount of LiBH$_4$ ($0.10 \leq x \leq 0.40$, Figure

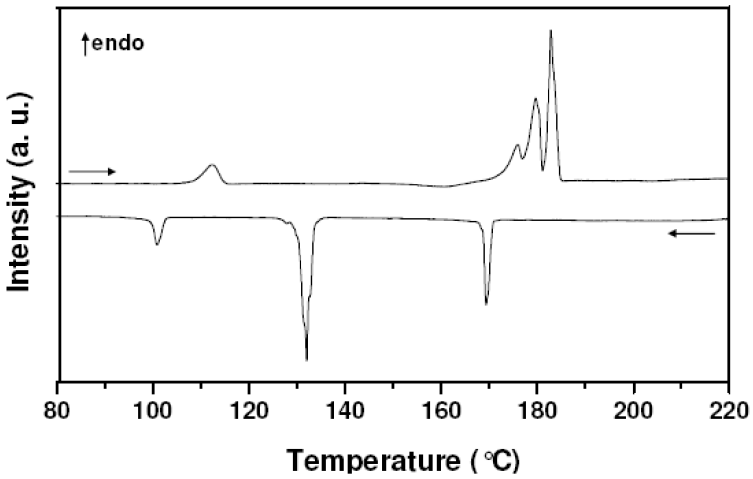

Figure 4.4: DSC profile of $0.25LiBH_4$-$0.75Mg(BH_4)_2$ composite after heating up to 220°C and cooling down to room temperature under 3 bar H_2 and a heating rate of 5 °C/min.

4.3h–k) show an additional peak very close to the melting at ca. 184 °C (peak 3), which gradually increases with increasing amount of $Mg(BH_4)_2$. Therefore, peak 3 may originate from the polymorphic phase transformation of the excess of $Mg(BH_4)_2$, which takes place immediately after the melting of the eutectic mixture. Interestingly, upon heating and cooling these endothermic events (peak 1-3) were found to be reversible (figure 4.4). These results support the hypothesis proposed above that the polymorphic transformation of $Mg(BH_4)_2$ becomes reversible in the presence of $LiBH_4$. Moreover, we see from Figure 4.3 that the polymorphic transition takes place at a temperature about 15° lower than the alpha to beta transition in pure $Mg(BH_4)_2$ (peak 3 and peak 4, respectively). From this shift we can conclude that the major effect of the $LiBH_4$ is changing the transformation kinetics. A relative stabilization of the alpha phase would always lead to an *increase* in the transition temperature. Decreasing kinetic barriers, on the other hand, *decreases* the alpha to beta transition temperature towards its thermodynamic limit. When the kinetic barrier is decreased sufficiently to enable a polymorphic transition at temperatures close to the thermodynamic limit the transition becomes reversible.

4.2.2 Thermo Gravimetric Analysis, Differential Scanning Calorimetry and Mass Spectrometry

The hydrogen desorption has been studied by using simultaneous thermo gravimetric analysis, differential scanning calorimetry and mass spectrometry.

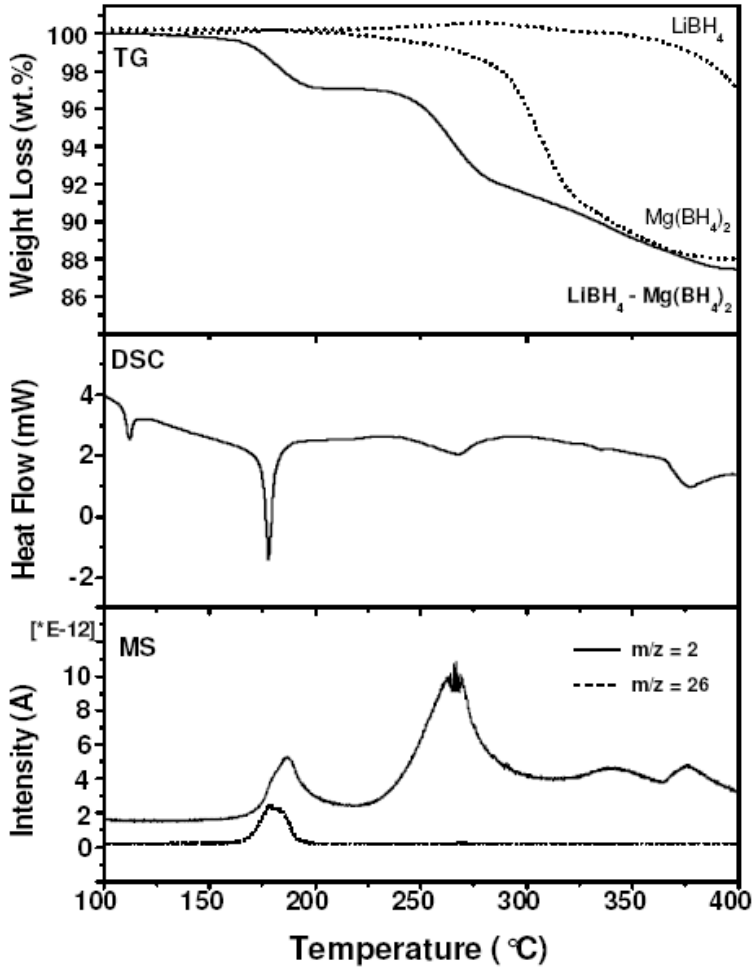

Figure 4.5: TG-DSC-MS profiles of milled $0.5LiBH_4$–$0.5Mg(BH_4)_2$, milled $Mg(BH_4)_2$ and milled $LiBH_4$ samples. The measurements were performed under 20 ml He flow and at a heating rate of 5 °C/min. A light fluctuation of the TG signal can be detected for pure lithium borohydride during the melting process (ca. 288 °C). The MS-signal of hydrogen (m/z = 2) is shown on the bottom together with the strongest signal of the characteristic mass fragments of diborane (m/z = 26).

Figure 4.5 shows the TG-DSC-MS profiles of the xLiBH$_4$–(1-x)Mg(BH$_4$)$_2$ composite with x = 0.5 .

According to the TG signal, the main decomposition of the $LiBH_4$–$Mg(BH_4)_2$ composite takes place between 170 °C and 400 °C. The hydrogen evolution detected by mass spectroscopy starts at around 170 °C. Three different decomposition steps can be clearly distinguished from the TG signal, each of them

associated with distinct hydrogen loss. Approximately 3.0 mass % loss was observed at 215 °C during the first step indicating that the decomposition of the sample takes place right after the melting. However, this weight loss can not be totally attributed to hydrogen since traces of diborane (m/z = 24, 25, 26, 27) were detected together with the hydrogen release (m/z = 2). A similar behaviour has been observed in the case of pure lithium borohydride under vacuum, where the hydrogen desorption is accompanied by the evolution of gaseous diborane, B_2H_6 [21]. The second step (215 – 280 °C) consists of a rapid hydrogen desorption resulting in additional 4.5 mass % loss. This decomposition process seems to be quite different from that of the pure borohydrides. While pure magnesium borohydride releases just 1.5 wt % H_2 at 280 °C, the decomposition of pure lithium borohydride starts not before 380 °C. Finally, during the last step (280 – 400 °C), an additional 5.1 mass % loss was observed. Hence, the total amount of hydrogen released at 400 °C for the $LiBH_4$–$Mg(BH_4)_2$ composite was found to be approximately 12.6 wt %.

The theoretical hydrogen capacity of the $LiBH_4$–$Mg(BH_4)_2$ composite can be calculated from reaction

$$LiBH_4 + Mg(BH_4)_2 \rightarrow LiH + B + MgB_2 + 11/2\ H_2 \quad 14.6\text{wt\% } H_2 \tag{4.1}$$

as 14.6 wt% H_2. However, it should be taken into account that the starting materials were not 100% pure and that during the synthesis of the composite by high energy ball milling some hydrogen is already liberated, as was confirmed by elemental analysis ($LiMgB_3H_{12}$; calc. = 15.9 % H, found = 15.0 % H). Thus, it can be suggested that at 400 °C the decomposition of $LiBH_4$–$Mg(BH_4)_2$ is finished to a degree of 85%.

4.3 In-Situ X-Ray Diffraction

In-situ XRD analysis of the material offers complementary information of the decomposition mechanism according to the temperature. For instance, it provides a direct evidence of the eutectic melting as well as, if it is the case, of the remaining solid phases. Therefore, this is a useful method to determine the eutectic composition in the physical mixture.

The *In-situ* XRD experiments have been performed for the composites with x = 0.33, 0.40, 0.50, 0.60, and 0.66. Figures 4.6 and 4.7 show the XRD patterns after stepwise heating up to 180°C for x = 0.33 and 0.66, respectively. Heating of the samples to 150°C leads to the transformation of beta into alpha $Mg(BH_4)_2$ in both compositions, since the peaks corresponding to the beta phase disappeared. Presumably, this behaviour can be explained by the compatible crystal structure of the constituent phases. Both the low temperature modification of $Mg(BH_4)_2$ and the high temperature modification of $LiBH_4$ crystallize in

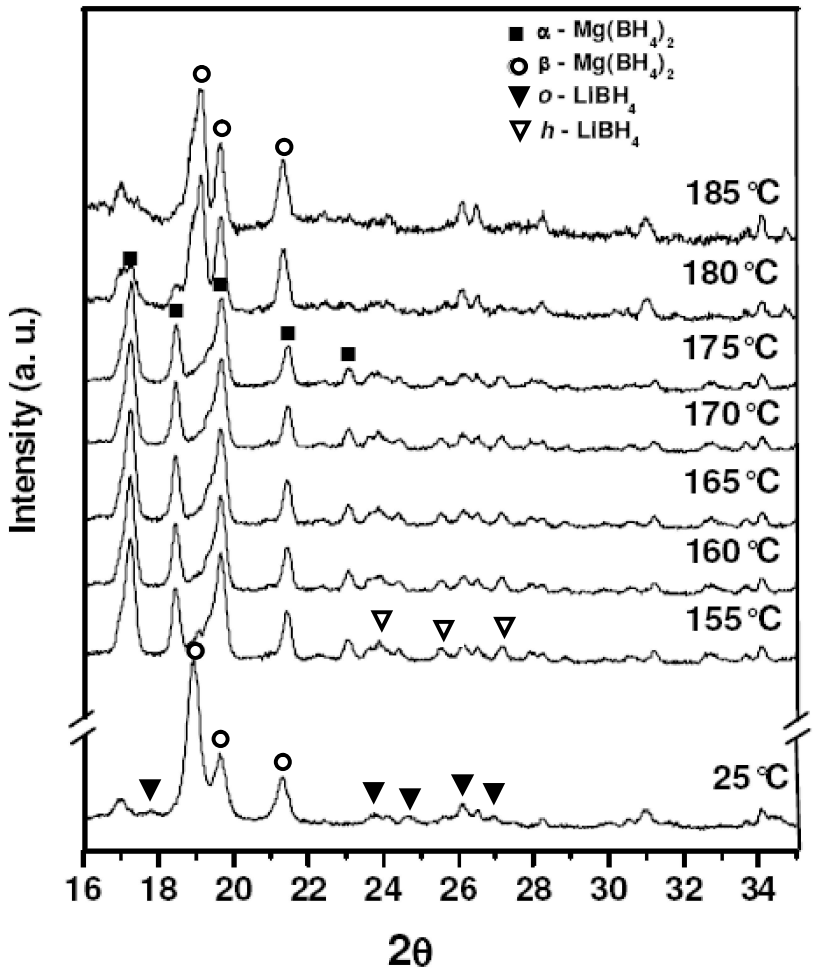

Figure 4.6: In-situ XRD patterns of the 0.33$LiBH_4$-0.66$Mg(BH_4)_2$ composite upon heating at 5 °C/min under He.

a hexagonal structure. Further heating to ca. 180°C leads to the melting of the sample. In the case of $x = 0.33$, only the peaks corresponding to alpha and beta phases of $Mg(BH_4)_2$ can be detected after melting, while for $x = 0.66$ only the peaks corresponding to the hexagonal phase of $LiBH_4$ can be observed together with an additional bump corresponding to the molten material. Hence, these results agree with the thermal analysis above suggesting that:

- the alpha phase of $Mg(BH_4)_2$ is stable;
- the eutectic composition lies in the range of $0.33 < x < 0.66$.

The XRD patterns of the intermediate composites are plotted together for different temperatures in Figure 4.8.

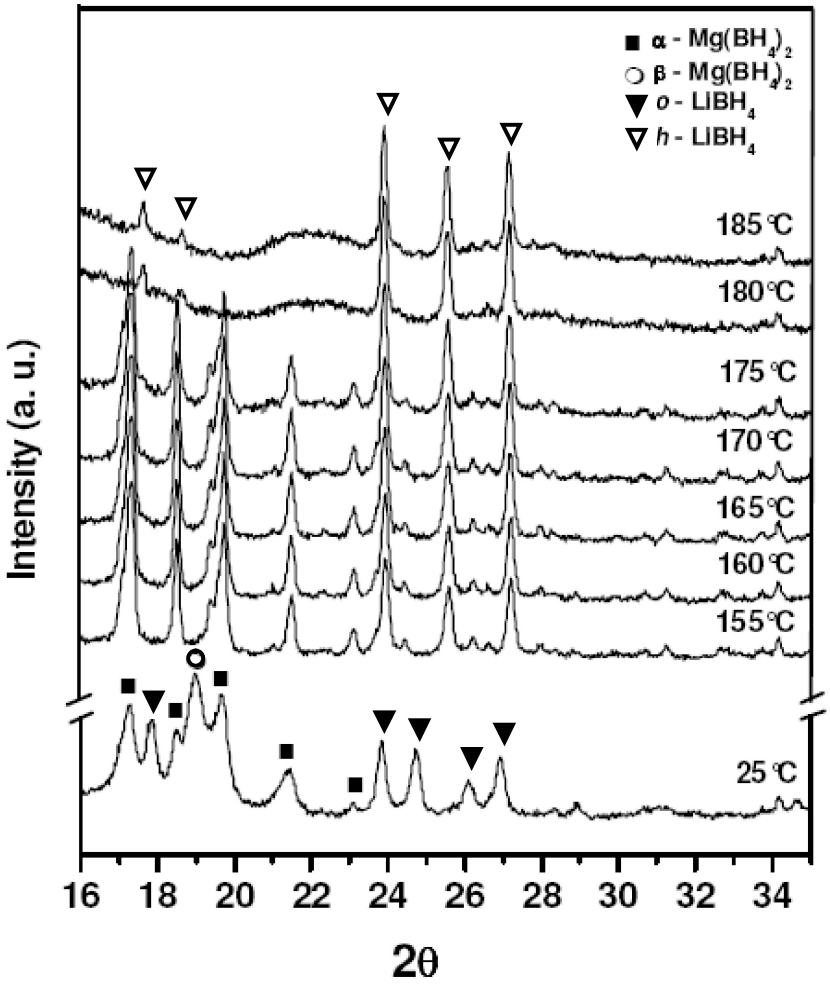

Figure 4.7: In-situ XRD patterns of the 0.66$LiBH_4$-0.33$Mg(BH_4)_2$ composite upon heating at 5 °C/min under He.

As expected, at room temperature only alpha- and beta-$Mg(BH_4)_2$ as well as orthorhombic-$LiBH_4$ can be detected. Upon heating up to 150 °C the peaks corresponding to the alpha phase gain increasing diffraction intensity whereas the beta phase disappears. The XRD patterns indicate that $x = 0.5$ is very close to the eutectic composition since no peak can be clearly detected at 180 °C. In contrast, $LiBH_4$ peaks can be found for $x = 0.60$ and 0.66 as well as $Mg(BH_4)_2$ peaks for $x = 0.33$ and 0.40, respectively, suggesting an excess of each component in the eutectic mixture.

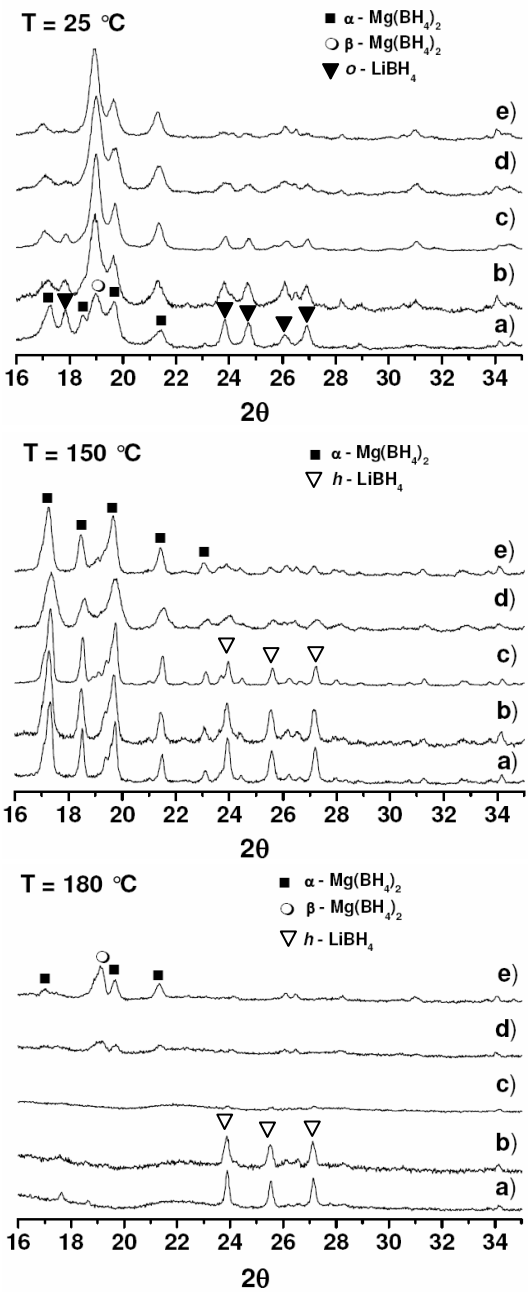

Figure 4.8: XRD patterns of xLiBH$_4$–(1-x)Mg(BH$_4$)$_2$ composites with (a) x = 0.66, (b) x = 0.60, (c) x = 0.50, (d) x = 0.40 and (e) x = 0.33, after heating up to 25°C, 150°C and 180 °C.

4.4 Phase Diagram

Considering the thermal decomposition data and the X-ray diffraction analysis, a phase diagram for this system is proposed in Figure 4.9. Following conclusions have been taken into account:

- The eutectic melting point of the physical mixture was 180 °C;
- The polymorphic transformations of the components were found to be at ca. 113 °C and 184 °C for $LiBH_4$ and $Mg(BH_4)_2$, respectively;
- An excess of $LiBH_4$ is present in the physical mixture for the composites with $x = 0.60$ (a small bump could be detected in the DSC profiles for those composites (Figure 4.2b-e) which is connected to the melting to the lithium borohydride excess which may show the limit of the liquidus temperature on one side);
- $Mg(BH_4)_2$ was found to be in excess for composites with $x = 0.40$ (as a tentative approximation, two dots are drawn in the diagram indicating the temperature of the first decomposition peak of $Mg(BH_4)_2$ detected by using DSC (Figure 4.2k-l));
- The eutectic composition could not be determined exactly but it is expected to be in the range of $0.50 < x < 0.60$, see extrapolation in Figure 4.9.

4.5 Hydrogen Desorption

The hydrogen desorption properties of the xLiBH$_4$–(1-x)Mg(BH$_4$)$_2$ composite with $x = 0.5$ were investigated by thermovolumetric method. The composite was slowly heated under an initial pressure of 1 bar H2 to 270 °C, 345°C and 435 °C, respectively, and the volume of released hydrogen was measured in a modified Sieverts type apparatus. The dehydrogenation profiles of the material at each decomposition temperature are shown in Figure 4.10.

The composite showed relatively slow hydrogen desorption kinetics at 270°C, where a total of 7.0 wt % of hydrogen was released after 48h. The XRD analysis of the partially dehydrogenated sample shows the presence of MgH_2 phase. These results are consistent with the thermogravimetric analysis of the composite, which shows 7.5 mass % loss at 280°C (Figure 4.5). Moreover, this indicates that the evolved diborane detected by mass spectrometry under this temperature should not be significant and thus, the mass loss detected by TG can be mostly attributed to hydrogen. During a second dehydrogenation experiment at 345 °C, the composite was able to liberate ca. 9.2 wt % of hydrogen after 20h.

At 435 °C, the sample exhibited much faster desorption, the hydrogen release was 11.6 wt % just after 4h. The diffraction peaks on the XRD patterns of the

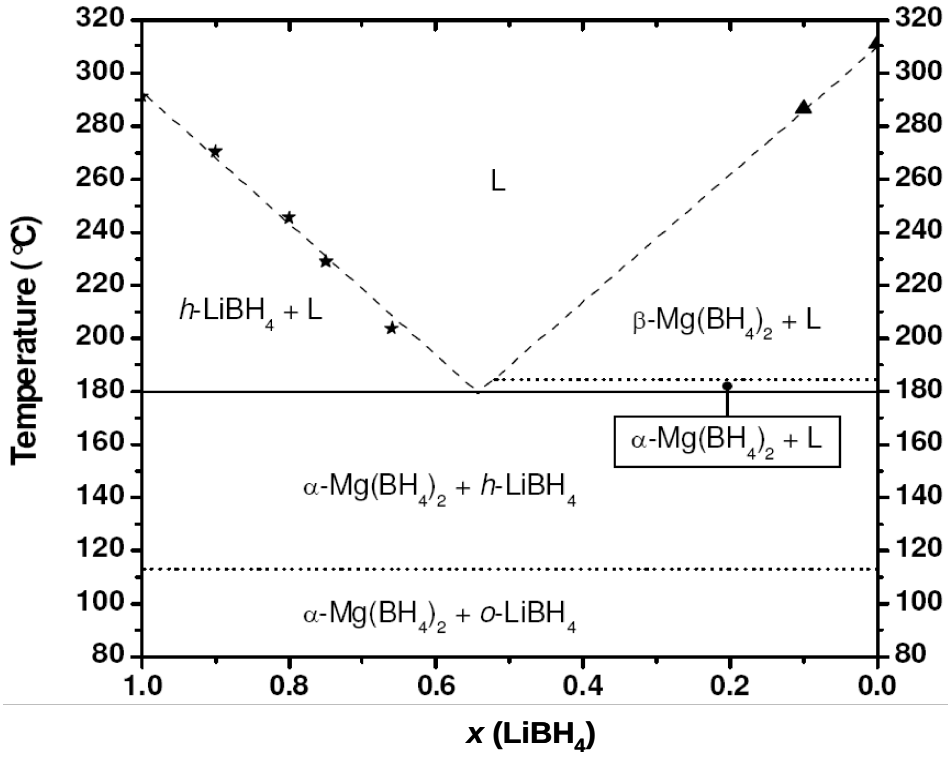

Figure 4.9: Tentative phase diagram for the physical mixture of xLiBH$_4$–(1-x)Mg(BH$_4$)$_2$.

dehydrogenated sample could be assigned to Mg and MgB_2. The observed MgO in the XRD patterns is possibly caused by the trace of air coming into the XRD sample holder during the measurement or to a small amount of oxidic compounds in the starting materials.

4.6 Conclusions

We have investigated the mixed lithium—magnesium borohydride system. In order to investigate this binary system, several composites have been synthesized, xLiBH$_4$–(1-x)Mg(BH$_4$)$_2$. High energy ball milling of LiBH$_4$ and Mg(BH$_4$)$_2$ leads, in all cases, to the formation of a physical mixture of the components rather than a new compound, the eutectic composition lies between $x = 0.5$ and 0.6. The presence of already a small amount of LiBH$_4$ affects the kinetics of the polymorphic transition in Mg(BH$_4$)$_2$ so that the orthorhombic phase (high temperature modification) can be reversibly transformed in the hexagonal phase (low temperature modification). The decomposition of the eutectic composition begins right after the melting at 180 °C, it hence releases hydrogen at much lower temperature

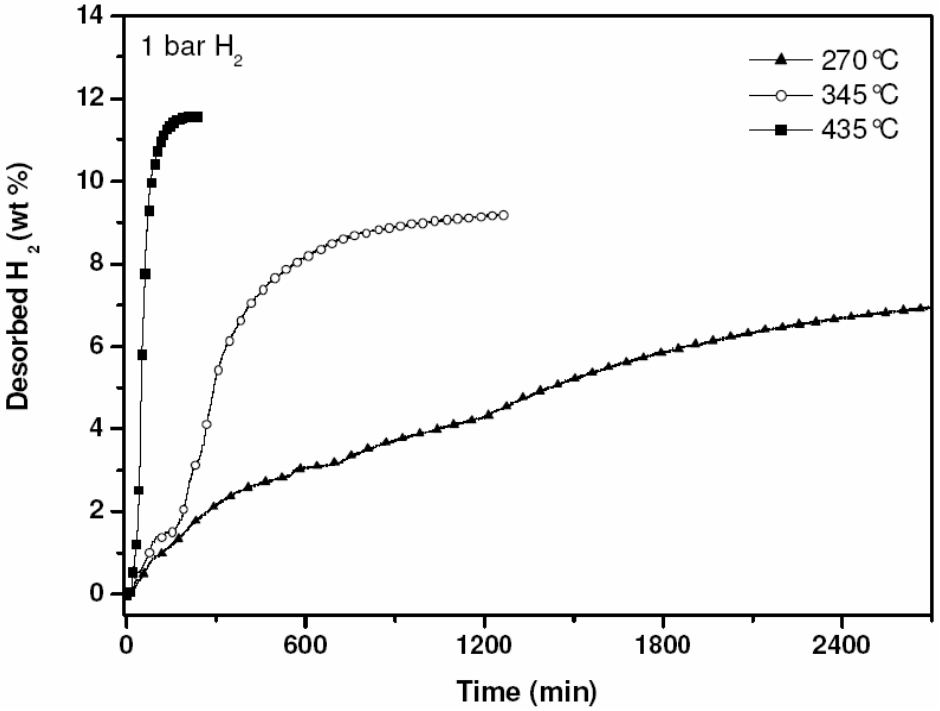

Figure 4.10: Isothermal hydrogen desorption curves of the $0.5LiBH_4$–$0.5Mg(BH_4)_2$ composite at 270 °C, 345 °C and 435 °C, respectively.

than the pure borohydrides. At 270 °C the $0.5LiBH_4$–$0.5Mg(BH_4)_2$ composite releases 7.0 wt % of hydrogen.

The result of this part has already been submitted [8].

Chapter 5

Thermodynamic Measurements

5.1 Chemical model

Thermodynamics parameters of absorption and desorption reactions of a material can be accessed by isotherm equilibrium measurements.

Considering the simple case where a metal hydride releases one hydrogen molecule according to

$$MH_2 \rightleftharpoons M + H_2 \tag{5.1}$$

the material in hydrided state, kept at constant temperature inside a reactor, is placed in contact with hydrogen gas at a certain pressure. Starting from high pressure of H_2 and removing gas, the pressure will initially decrease; then for increasing amounts of removed hydrogen gas, the pressure will remain constant and at a certain point the pressure starts decreasing again. This happens because there are different phases involved in the reaction.

At the beginning of the process H_2 is present in form of solid solution inside β-phase. When a lower hydrogen pressure is reached the *de-hydriding reaction* takes place: hydride decomposes with formation of α-phase end evolution of H_2 gas from the material; removing more gas, a bigger amount of β-phase is transformed in α- and remains inside as solid solution; at this temperature and pressure the reaction 5.1 is in equilibrium condition and an increase in pressure would drive it to the direction of the hydride. When all the material is converted, removing more gas forces the soluted hydrogen to be desorbed from the α-phase.

Equilibrium pressure is correlated with temperature, so repeating this experiment for different temperatures the material reacts at different pressure. The result is a *Pressure Composition Isotherm* (PCI) plot of a reaction as shown in fig. 5.1 (left).

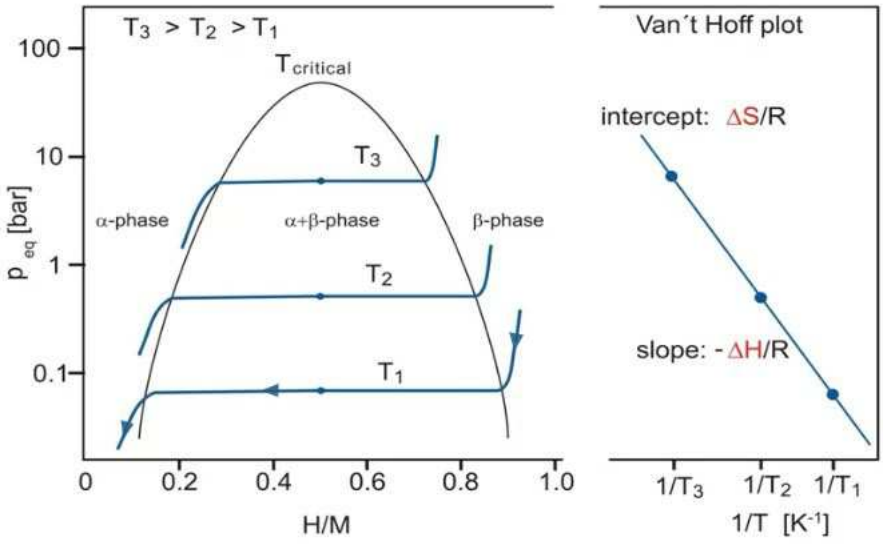

Figure 5.1: Example of PCI plot (left) and corresponding Van't Hoff plot (right) in case of a simple hydriding reaction 5.1; H/M is the molar ratio between the reagents [61].

These data can be converted into a *Van't Hoff plot* reporting $\ln(P/P_0)$ over 1/T, connected to the *Van't Hoff equation*

$$\ln\left(\frac{P}{P_0}\right) = -\frac{\Delta H}{R}\frac{1}{T} + \frac{\Delta S}{R}. \tag{5.2}$$

The experimental points should lay on a straight line whose slope and intercept allow to estimate ΔH and ΔS. Free energy of the reaction can be calculated from

$$\Delta G = \Delta H - T\Delta S. \tag{5.3}$$

Optimal values of enthalpy in case of a "ideal material" which is at equilibrium pressure of 1 bar at room temperature (it means ΔG = 0 at 300 K) are ΔH $\approx$ 40 kJ mol^{-1} H_2 calculated considering the ΔS value dominated by the gas entropy ΔS $\approx$ 130 J mol^{-1} K^{-1} .

Analysis of dehydriding reactions can be carried out in the same way moving with pressure on the opposite direction: starting from higher pressure ad decreasing it removing gaseous H_2.

In case the material can admit multi step hydriding - dehydriding reactions the experimental data show more than one pressure *plateau*.

5.2 The Gas Reaction Controller Sievert's Apparatus

Pressure composition Isotherm are performed inside *Gas Reaction Controller* (GRC), a fully automated Sievert-type Apparatus produced by Advanced Material Corporation (850 Poplar St., Pittsburgh, PA 15220 U.S.A.). The electro mechanical system is controlled by a personal computer which perform every gas load and download and calculates the amount of reacted gas in moles and wt% from the weight of the loaded sample.

5.2.1 Layout of GRC

The GRC system's layout is reported in Figure 5.2. The sample is placed inside "*Sample CH1*" chamber which is actually made by two parts separated by a valve, one external and one internal. The external part is a 30 cm long stainless steel tube placed inside a cylindrical furnace for the temperature control. It contains the sample holder which is a little stainless steel cylinder (with internal volume equal to 4 cc) mounted inside the eternal part which integrates a thermocouple, *TC1*, placed exactly on the sample; the tube is connected to the internal part which is inside the main system box and hosts the *HP1* pressure transducer.

The sample holder has been cleaned with concentrated hydrochloric acid, water, ethanol and acetone, then dried in furnace at 115°C. It was usually transfered together with the external part inside the glove box, powder sample was inserted and covered with a little amount of quartz wool for keeping powder into the cylinder during handling and evacuation. The sample holder is then inserted to the external part and sealed to it. Then is was carried out and connected to the system. It's internal volume is purged before opening the valve to avoid any contact of the sample with air.

5.2.2 Operations of GRC

The GRC first admits an appropriate amount of gas to the reservoir (see Fig. 5.3) and determines its molar amount N_0 from its pressure and temperature. The system then manipulates the valves between the reservoir and the reaction chamber and transfers a desired amount of the gas from the reservoir to the reaction chamber. After the gas-solid reaction is complete, the system calculates the total molar amount of gas N_g in the sample chamber and in the reservoir. The molar amount of gas absorbed by the solid by reaction N_s is given by

$$N_s = N_0 - N_g \ . \tag{5.4}$$

Here it's assumed that the initial amount of gas atoms in the solid is zero. When this is not the case, Equation 5.4 needs to be modified to

$$N_s = N_{s0} + (N_0 - N_g) \ , \tag{5.5}$$

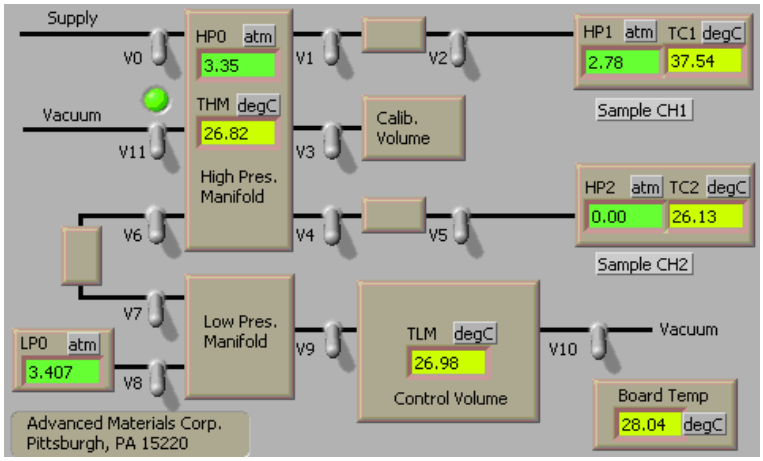

Figure 5.2: Layout of GRC from GrcLV controller software.

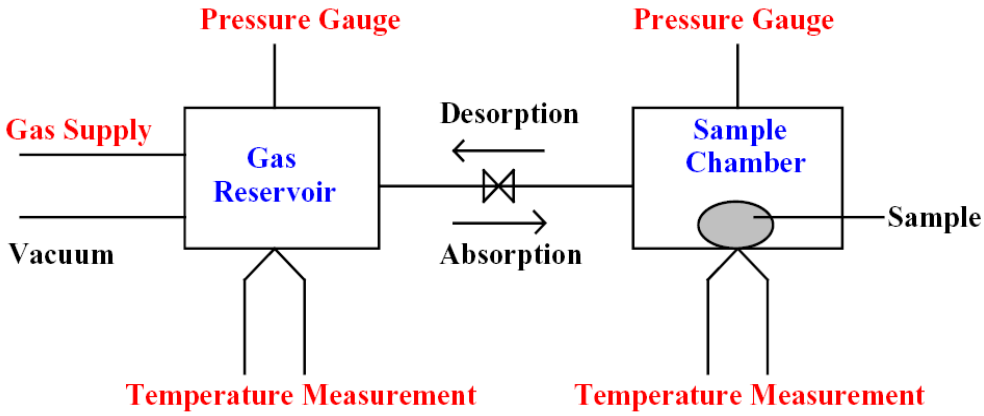

Figure 5.3: The amount of gas is determined from measurements of temperature and pressure.

where N_{s0} is the initial molar amount of gas in the solid. The control program GrcLV initially assumes $N_{s0} = 0$ but keeps track of the value of N_{s0} in subsequent steps, such as a desorption run and re-runs at different temperatures. The value can be reset to zero by inserting "evacuation" step where the sample chamber is evacuated and GrcLV resets N_{s0} to be zero.

Since the molar amount of the gas is essentially given by the ideal gas law,

$$N = \frac{pV}{RT} , \tag{5.6}$$

the accuracy of the system is limited by the accuracy of the pressure and the temperature measurements. When the temperature is well regulated, the pressure measurement is generally the limiting factor. In an absorption measurement, the

accuracy of the pressure is 0.1 psi = 6.89 ·E-3 bar and the volume involved is about 50 cm^3. Therefore the accuracy of the measurement is 0.1 psi x 50 cm^3 / 15 psi = 0.3 cm^3 stp.

In desorption measurement, the gas pressure of a much larger volume of 1000 cm^3 is measured using a more sensitive gauge with an accuracy of 0.01 psi resulting in the same accuracy of 0.01 psi x 1000 cm^3 / 15 psi = 0.7 cm^3 stp.

For samples that absorb large amount of gas (e. g., up to 150 cm^3 of H_2 gas per a gram of $LaNi_5$), its quantity can be determined with high precision. However, accuracy of the PCI measurement may actually be limited by slow kinetics.

GrcLV reports the reacted amount of gas as an absolute value in ccstp (cm^3 at Standard Temperature and Pressure) as well as a weight percent to the sample. The absolute value in ccstp ν is related with N_s by

$$\nu = 22413.6 \times N_s \ . \tag{5.7}$$

The relative value of gas to the mass (weight percent, wt) is given by

$$wt = \frac{N_S M_G}{m} \times 100 \tag{5.8}$$

where m is the mass of the sample and M_G is the molar mass of the gas (1.0079 x 2 for hydrogen). If the molar mass is known for the sample, the formula ratio of the gas atom to the host (x) can also calculated as follows for diatomic molecules:

$$x = \frac{2N_S}{(m/M)} = \frac{2M}{M_G}\frac{wt}{100} \tag{5.9}$$

5.2.3 Beattie-Bridgeman Equation

For clarity, the ideal gas law has been used in the above discussion. Although this gas law gives a good approximation for a wide range of temperature and pressure, the provided program GrcLV employs a Virial Expansion Equation for better accuracy.

The system software employs a third order virial expansion equation in calculating the amount of the gas from its pressure, temperature, and the volume it occupies. The equation for 1 mole of gas may be given as

$$\frac{PV}{RT} = 1 + B(T)\frac{1}{V} + C(T)\frac{1}{V^2} + D(T)\frac{1}{V^3} \tag{5.10}$$

where $B(T)$, $C(T)$, and $D(T)$ are the second, third, and fourth virial coefficients that depend on temperature. These coefficients may be calculated using the equation of Beattie and Bridgeman (Z. Physik 62, 95 (1930)) from five constants.

Gas	A_0	a	B_0	b	c
He	0.0216	0.05984	0.01400	0.0	40
Ar	1.2907	0.02328	0.03931	0.0	5.99×10^4
H_2	0.1975	-0.00506	0.02096	-0.04359	504
N_2	1.3445	0.02617	0.05046	-0.00691	4.20×10^4
CH_4	2.2769	0.01855	0.05587	-0.01587	12.83×10^4
CO_2	5.0065	0.07132	0.10476	0.07235	66.00×10^4

Table 5.1: Constants for calculation of the virial coefficients.

The relations are:

$$B(T) = B_0 - \frac{A_0}{RT} - \frac{c}{T^3} \tag{5.11}$$

$$C(T) = -B_0 b + \frac{A_0 a}{RT} - \frac{B_0 c}{T^3} \tag{5.12}$$

$$D(T) = \frac{B_0 bc}{T^3} \tag{5.13}$$

The five coefficients are listed in Table 5.1 for several gases. Note that units for the pressure, temperature, volume are atmosphere, kelvin, and liter, respectively.

From Equation 5.10, the amount of gas molecules n in a given volume of v at pressure p and temperature T is given by

$$n = \left(\frac{pv}{RT}\right) \Big/ \left(1 + B(T)\frac{n}{v} + C(T)\frac{n^2}{v^2} + D(T)\frac{n^3}{v^3}\right) \tag{5.14}$$

The value of n can be determined, for example, by numerical iteration.

5.2.4 Benedict-Webb-Rubin Equation of State

The used version of GrcLV software employs modified Benedict-Webb-Rubin equation of state for hydrogen to get better accuracy in extreme conditions.

$$\begin{aligned} P = {} & \rho RT + \left(B_0 RT - A_0 - \frac{C_0}{T^2}\right)\rho^2 + (bRT - a)\,\rho^3 + \alpha a \rho^6 + \\ & + \frac{c\rho^3}{T^2}\left(1 + \gamma\rho^2\right)\exp\left(-\gamma\rho^2\right) \end{aligned} \tag{5.15}$$

In moderate conditions, the difference between the Beattie-Bridgeman equation and Benedict-Webb-Rubin equation is small. Table 5.2 compares the density of hydrogen calculated by several different methods.

5.2.5 Soak and Release modes

Most user tasks can be performed automatically with the GRC by using the following standard automatic operation modes:

Condition	Ideal Gas Law	Beattie-Bridgeman	Modified Benedict -Webb-Rubin
400° C, 50 atm	1.825	1.796	1.798
400° C, 100 atm	3.650	3.533	3.545
400° C, 200 atm	7.300	6.828	6.894
25° C, 50 atm	4.497	4.365	4.355
25° C, 100 atm	8.995	8.438	8.440
25° C, 200 atm	17.989	15.685	15.868
77 K, 50 atm	15.954	16.701	16.718
77 K, 100 atm	31.907	31.934	31.671
77 K, 200 atm	63.814	53.495	50.097

Table 5.2: Calculated density of hydrogen (kg/m^3).

- **Soak Mode**: starting from a material in de-hydrided state and kept at certain temperature under a low value of gas pressure, the system fills Sample Chamber with a specified pressure of gas from the High Pressure Manifold and periodically keeps a record of the pressure, temperature, and amount of absorbed gas. This mode may be used for studying kinetics of the reaction and activation processes.

- **Release Mode**: starting from a material in hydrided state and kept at certain temperature under a high value of gas pressure, the system reduces the pressure to a specified value and keeps a record of the pressure, temperature, and amount of released gas as a function of time.

In these two modes the hydrogen pressure on the sample is not strictly constant. V1 and V2 valves are closed during the waiting time between two experimental data points. During this period the material reacts either releasing or absorbing gas (according to the actual pressure and temperature); this phenomena changes the amount of free gas inside the sample chamber with a consequent variation of the pressure.

In *Soak* mode the Sample Chamber is placed in communication with the High Pressure Manifold which is still at the initial pressure. The pressure difference moves gas from manifold to sample and partially compensates the adsorbed gas, considering that the two parts have a similar volume (42.84 cc for Sample Chamber, 36.26 cc for High Pressure Manifold). In *Release* mode the expected phenomena is a pressure increase which is partially compensated by the system opening all the internal valves and letting gas expanding from Sample Chamber to the internal volumes including the Control Volume, offering a total volume of 645.74 cc. The effective volume used by software for calculations is corrected by subtracting the Volume displaced by sample which is calculated from sample

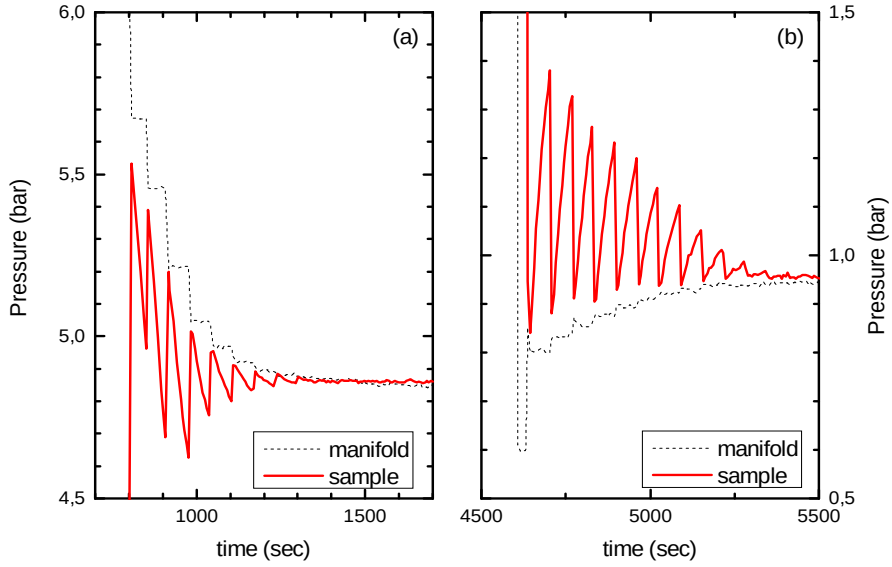

Figure 5.4: Pressure over time registered on the sample and inside the High Pressure Manifold during Reaction 5.16 with GRC system operating in *Soak* and *Release* mode (*a* and *b*, respectively).

weight and density (provided by user).

The measurement's terminating condition is the specified Run Period. Data recording time is usually set to 60 sec; data logging is usually set to 10 sec.

The effect of this behavior can be seen in Figure 5.4 during a calibration run using $LaNi_5$ at room temperature according to reaction 5.16.

$$LaNi_5 + 3H_2 \rightleftharpoons LaNi_5H_6 \tag{5.16}$$

5.2.6 Pressure composition isotherm modes

Two PCI modes are available:

- **PCI Absorption Mode** (PCIa): Determines the pressure-composition isotherm of a sample in Sample Chamber. This mode gives the full thermodynamic properties of the gas-alloy reaction.
- **PCI Desorption Mode** (PCId): Perform the same as above for desorption.

With these modes the system changes the pressure on the sample step by step covering a predetermined range, then for every pressure step operates similarly to

the previous modes compensating the eventual gas release or absorption opening the valves connecting Sample Chamber to High Pressure Manifold.

The system checks the experimental parameters every minute registering these "*non-equilibrium* data points" in a separate file; if the material is reacting the system will observe a pressure change $\mathrm{d}P/\mathrm{d}t$; this change will be compared to the predetermined threshold $\mathrm{d}P$: if

$$\mathrm{d}P/\mathrm{d}t < \mathrm{d}P/10 \text{ minutes} \tag{5.17}$$

the system considers the reaction running and waits before adding or removing gas till the settling condition is fulfilled or until Maximum Waiting Time, $\mathrm{t_{max}}$, is reached. When the settling condition is satisfied the system registers all the experimental parameters as "*equilibrium* data point" and proceed to the next target pressure.

The measurement's primary terminating condition is the reaching of the specified final pressure on the sample.

Value range for pressure settling condition is between 10–0.01 bar; a low $\mathrm{d}P$ value increases the resolution of the pressure *plateau* and it's useful in case of slow kinetic materials. A small $\mathrm{d}P$ value has to be used with relatively long Maximum Waiting Time for allowing the system to reach the true equilibrium condition, especially at low temperature when kinetic is slow: the total measurement time could consequently become longer in the order of days.

An example of this behavior is reported in Figure 5.5a where the GRC system is working in PCId mode on $\mathrm{Mg(BH_4)_2}$ sample decomposing at 307.0°C ($\mathrm{d}P$=0,02 bar, $\mathrm{t_{max}}$=33 min). *Non-equilibrium* data (+) are always recorded every 60 seconds; in pressure range near to PCI's plot *plateau* pressure (50–46 bar) *equilibrium* data (•) are recorded every 33 minutes (at the end of the Maximum Waiting Time) while near the end of the *plateau* (in this plot for P lower then 46 bar) only few minutes are necessary for satisfying the $\mathrm{d}P$ settling condition. As a consequence, *non-equilibrium* points are either placed before the correspondent *equilibrium* point or scattered around it. This positioning confirms the correct behavior of the system and allows us to identify non reliable data: in this example, the two *non-equilibrium* points at 45.8 bar and -3.7 wt% has to be considered errors due to instability of HP1 pressure transducer and has to be ignored in following data elaboration. Figure 5.5b shows the same behavior in case of $\mathrm{LiBH_4}$ decomposition at 430°C.

The reported data shows that although the system did not really worked in equilibrium condition, a good estimation of the correct equilibrium pressure is still possible using the value at the beginning of the process (at low wt% values).

The effect of different $\mathrm{d}P$ values on PCI plot has been observed in case of $\mathrm{Mg(BH_4)_2}$ decomposition: isothermal decomposition of α-magnesium borohy-

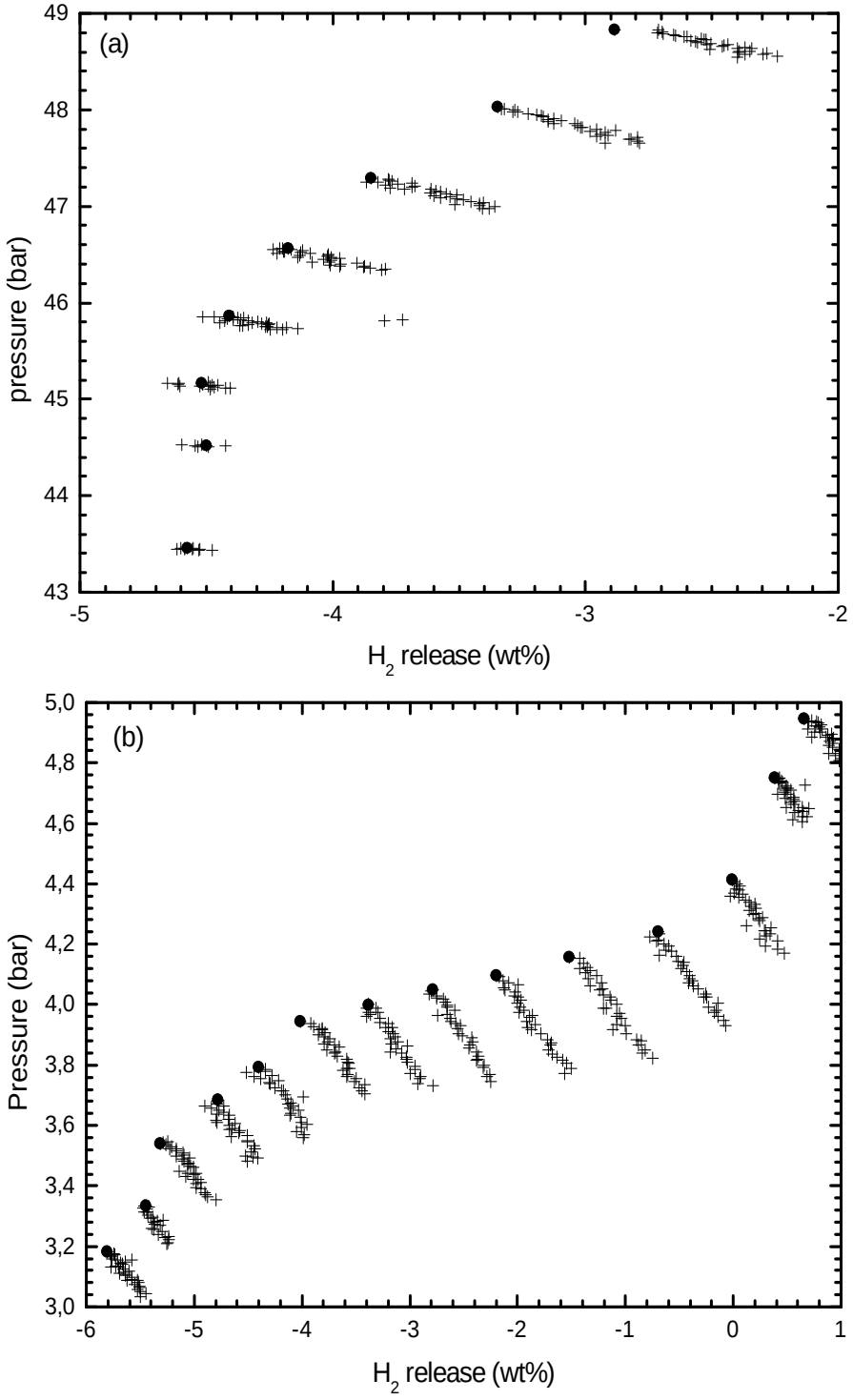

Figure 5.5: Detail of the pressure *plateau* of PCI measurements showing *equilibrium* (•) and *non-equilibrium* (+) points registered by GRC system operating in *PCId* mode during decomposition of $Mg(BH_4)_2$ sample at 307°C (a) and $LiBH_4$ sample at 433°C (b).

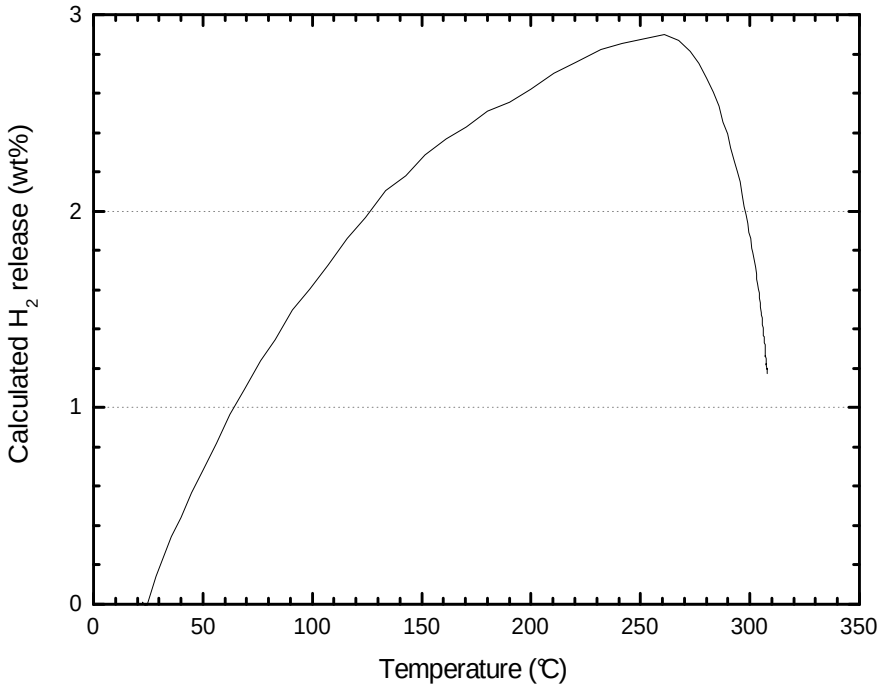

Figure 5.6: calibration runs without sample; wt% profile calculated by GRC system using *monitor* mode during heating from 25 to 307°C under 110 bar H_2 backpressures.

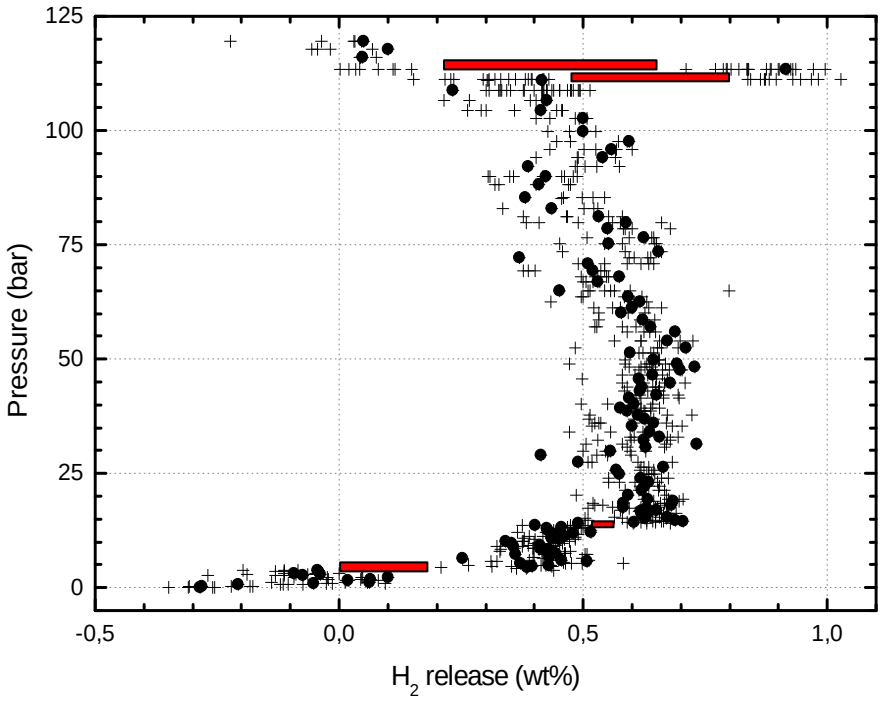

Figure 5.7: *equilibrium* (•) and *non-equilibrium* (+) points registered by GRC system operating in *PCId* mode during calibration run without sample at 307°C.

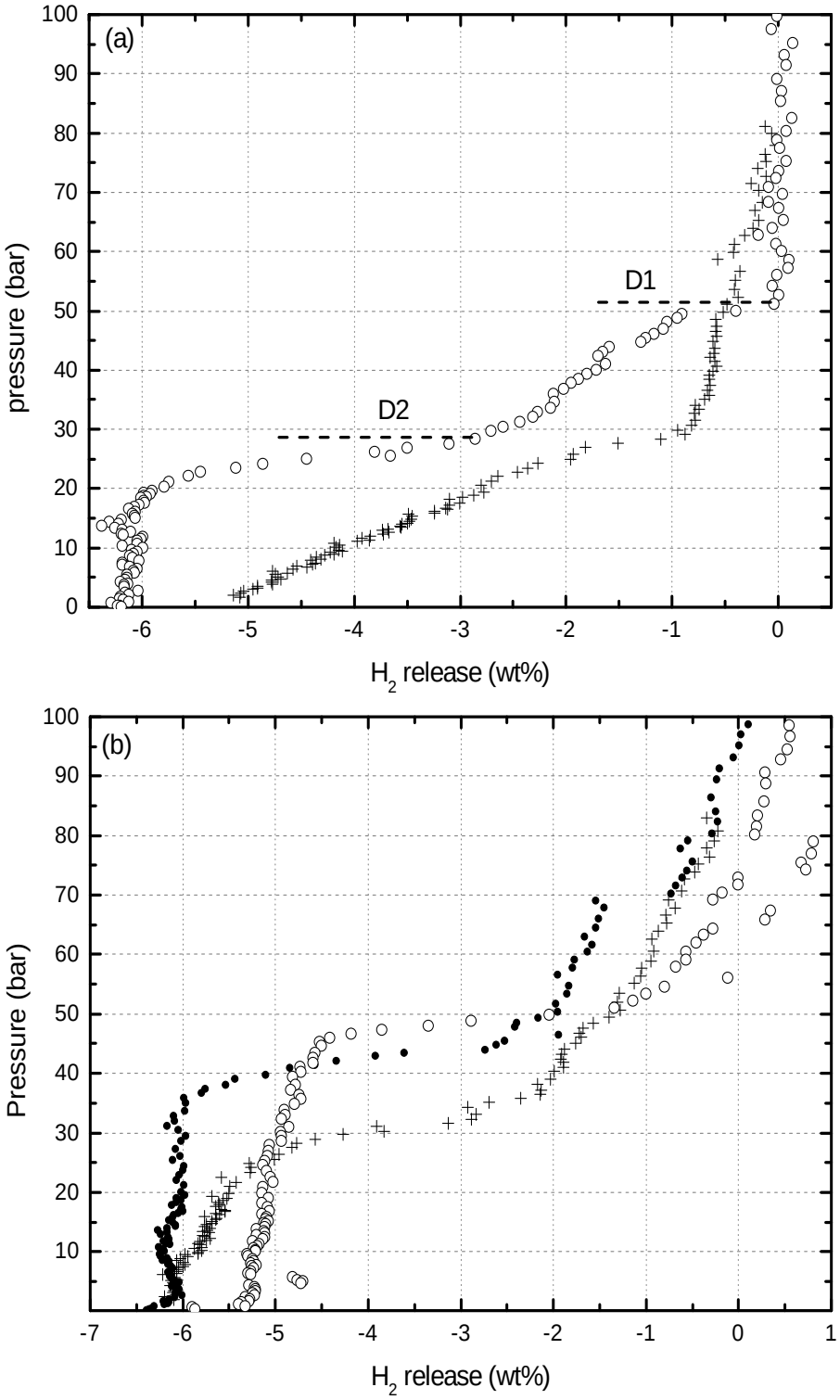

Figure 5.8: PCId measurements of $Mg(BH_4)_2$ performed at 281°C (a) and 307°C (b) with different settling conditions; dP=0.1 bar, t_{max}=8 min (+); dP=0.05 bar, t_{max}=15 min (•); dP=0.02 bar, t_{max}=33 min (◦).

dride synthesized and ball milled for 4 hours has been performed at 281° and 307°C in PCId mode with different settling conditions for reaching a balance between measuring time and reliability of pressure *plateau* shape and positioning; moreover these data allow a comparison with eutectic mixture decomposition inside GRC system. The results are reported in Figure 5.8: dP=0.1 bar, t_{max}=8 min (+); dP=0.05 bar, t_{max}=15 min (•); dP=0.02 bar, t_{max}=33 min (◦).

The decomposition performed at 281°C with dP=0.5 shows two different reactions: one well defined *plateau* at 28 bar and one non equilibrium decomposition from 25 to zero bar. The use of a smaller settling condition (dP=0.02 bar) coupled with a longer waiting time for every equilibrium point moves the estimation of the first step to 50 bar and increases the resolution of the following step; the second decomposition clearly happens between 30 and 18 bar placing out best estimation of *plateau* pressure at 27.5 bar. An incorrect estimation of the second equilibrium temperature is probably connected to slow kinetic of decomposition reaction at this temperature.

At 307°C the use of smaller dP value and longer t_{max} values do not improve the shape of the *plateau* but increases the estimation of the equilibrium pressure, confirming that at this temperature the reaction has a fast kinetic; only one decomposition process is detectable.

Reported data has been acquired decomposing 100 mg of sample. The use of smaller amount of sample can effect equilibrium pressure estimation because in case of slow kinetic decomposition, the absolute amount of released gas could result in a small pressure change. If this initial pressure change is smaller than dP value the system considers the pressure as settled and moves to next – lower – pressure step. The final effect is an underestimation of equilibrium pressure.

A full range PCId run without sample has been performed at 307°C ($125 < P < 0.1$ bar, dP=0,02 bar, t_{max}=33,33 min, 126 equilibrium data points) is reported in Figure 5.7: excluding the wrong equilibrium points identified by the lack of non-equilibrium points between these data and the previous (underlined in the plot by red lines), the equilibrium points distribution is within 0.4 wt%. In absence of the sample, wt% values have been calculated for 0.094 mg of material with density 0.780 g/cc which are the typical conditions of a PCId measurement made on sample with composition near to the eutectic mixture.

5.2.7 Monitor mode

One more simple mode is available:

- **Monitor Mode**: Periodically records pressure, temperature, and amount of absorbed gas as a function of time. Typically used with temperature ramp operation.

In this mode the system do not perform any operation except changing the sample temperature according to an eventual temperature ramp. This mode can be used for kinetic measurements in alternative to *soak* or *release* mode. In comparison with *release* mode, in case of sample decomposition, the lack of pressure compensation through expansion in bigger volume results in higher pressure increase during gas evolution from the material (ratio between Sample Chamber volume and the total available volume for gas expansion in *release* mode is 0.065). This higher pressure increase is correctly interpreted by the software which calculates the right H_2 wt% value and the measure shows a better signal/noise ratio. For this reason this mode has been used during non-isothermal dynamic decomposition measurements where a change in pressure value is expected and a better estimation of small gas release is important for studying the different steps of the decomposition reaction. Moreover effective pressure value for the every experimental point is recorded.

An example of *monitor* mode data in comparison to *release* mode is plotted in Figure 5.9: the same sample xLiBH$_4$–(1-x)Mg(BH$_4$)$_2$ with x=0.6 (sample (f) of Figure 4.2) has been decomposed in presence of SiO_2 (as catalyst) inside GRC system under three different initial H_2 backpressures. Data corresponding to 25 bar backpressure do not show noise at this scale while data corresponding to 3 and 11 bar backpressure recorded in *release* mode suffers by high noise and by a transducer's random error which is the cause of the evident vertical steps at around 100, 430 and 480°C (3 bar measurement) and 340°C (11 bar measurement).

One calibration on hydrogen content (expressed in wt%) is necessary for this mode. The layout of GRC were Sample Chamber is a volume which is partially inside a furnace at temperature = T_{sample} and partially inside the system at room temperature is the cause of a thermal gradient affecting the stainless steel of the sample holder and consequently the gas inside. Moreover this temperature gradient evolves with time during a heating ramp of the furnace according to the heating rate and the final temperature. The result is an inhomogeneous thermal expansion of the gas which depends by the described parameters and by the starting hydrogen pressure inside the Sample Chamber. The software can correctly compensate this variation only for low pressure values ($P < 3$ bar); the result of this error is a vertical shift of H_2 release towards positive values which is evident in Figure 5.9 (green line, 25 bar) between 25 and 250°C where, according to chemistry of the reaction, no H_2 absorption is expected while a small drift of data towards positive values of wt% is visible.

A complete set of calibration measurements without sample from 25 to 560°C and heating rate of 2 K/min under a backpressure of 10, 30, 60 and 90 bar has been performed and are reported in Figure 5.10. In absence of the sample, wt%

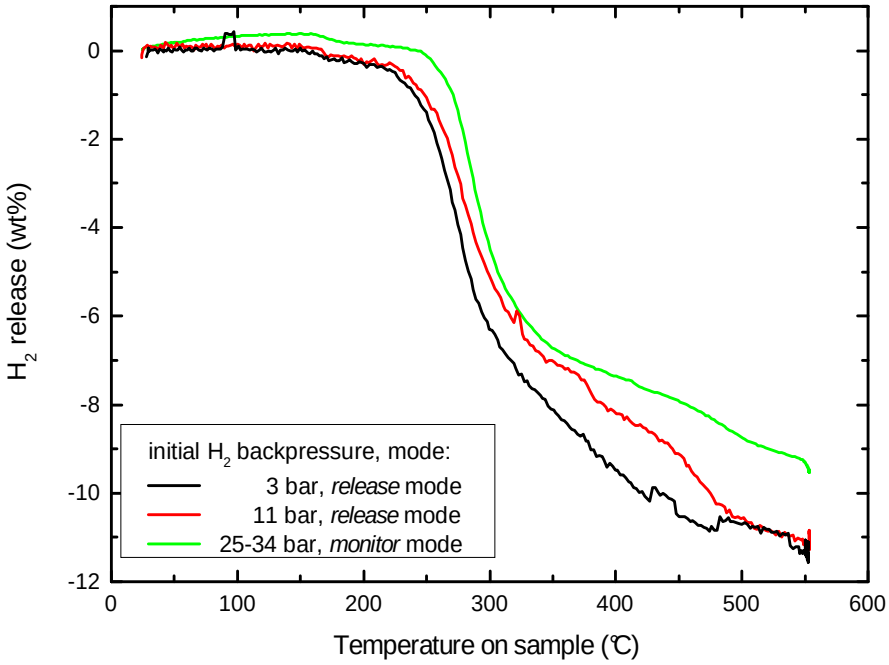

Figure 5.9: Mixture $0.6LiBH_4$–$(0.4)Mg(BH_4)_2$ decomposed in presence of SiO_2 under three different initial H_2 backpressures using *monitor* and *release* mode.

values have been calculated for 0.043 mg of material with density 0.780 g/cc which are the typical conditions of a dynamic decomposition measurement made on sample with composition near to the eutectic mixture.
These values for wt% has been subtracted to registered values of H_2 release from samples during measurements performed at the same temperature in the same heating rate conditions. The final vertical part after 550 °C, showing different wt% values for the same temperature on the sample is justified by two effects: the evolution of the thermal gradient towards a thermal equilibrium with environment after that the maximum temperature is reached; the stainless steel absorption of hydrogen, phenomena which is expected under these conditions. At low pressure (cases *a* and *b*) the first effect drives wt% data toward negative values, at higher pressure (cases *c* and *d*) the second effect becomes prevalent, moving wt% towards positive values.

The same situation occurs during the heating ramp used for heating sample to target temperature before starting a PCId measurement: the sample chamber is loaded with 110 bar H_2, the GRC system register and irregular pressure increase due to inhomogeneous heating of the sample chamber and for increasing temperature it calculates an incorrect hydrogen absorption value, reported in Figure

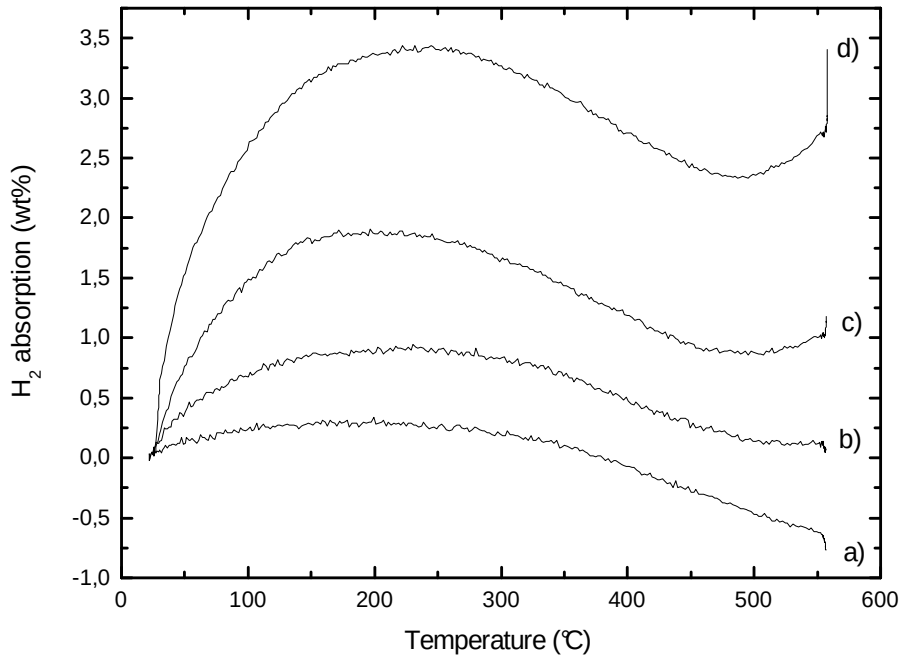

Figure 5.10: calibration runs without sample for dynamic decomposition measurements using *monitor* mode and different initial H_2 backpressures; 10 bar (a), 30 bar (b), 60 bar (c) and 90 bar (d).

5.6: absorption error is +1.2 wt% after thermal gradient stabilization at 307°C.

The absolute error value depends by final temperature, so one blank test should be carried out for every temperature; actually, in the hypothesis that the sample do not chemically reacts in these experimental condition, the wt% value can be reset to zero before starting the PCId measurement; this operation has been performed for data reported in Figure 5.7 where first point at 124 bar is correctly placed on 0.0 wt% value. In following experimental PCId measurements this correction hasn't been applied.

Anyway in case of isothermal measurement this error is constant and it affect only the initial amount of stored hydrogen; the relative H_2 wt% changes during pressure decrease can be still considered reliable, as confirmed by the absence of horizontal drift in equilibrium data points for decreasing pressure over two order of magnitude, as reported in Figure 5.7. Moreover the used parameter for determination of reaction enthalpy and entropy is pressure of *plauteau*, independently by the absolute wt% value.

5.3 Performed decomposition experiments

Reagents and product of the mechanochemical synthesis has been analyzed with GRC system: $LiBH_4$, $Mg(BH_4)_2$ and $x LiBH_4$–(1-x)$Mg(BH_4)_2$ with $x = 0.6$, the physical mixture with composition near to eutectic.

Two types of decomposition experiments have been performed: dynamic decomposition experiments for an overview on the hydrogen release behavior of and PCI decomposition experiments for identifying the involved reactions from decomposition's pressure *plateau*.

Eutectical mixture has been synthesized by ball milling (4 hours at 600 rpm), so the same treatment has been applied to commercial lithium borohydride and prepared magnesium borohydride.

Dynamic decomposition experiments have been performed decomposing 50 mg of sample with a temperature profile ranging from 25 to 550°C at heating rate of 2 K/min; *monitor* mode, data acquisition every 60 seconds.

PCI decomposition experiments have been performed decomposing 100 mg of sample with pressure ranging from 120 to 0.1 bar at different temperatures; settling conditions have been fixed to dP=0.02 bar and t_{max}=33 min; non- equilibrium data recording every 60 seconds. Samples have been loaded inside GRC system at room temperature; 110 bar hydrogen overpressure has been added, then temperature has been increased from 25°C to target temperature using a fast thermal ramp (10 K/min) followed by 1 hour thermal stabilization time; final pressure was over 125 bar. Thermodynamic parameters have been registered during the heating ramp and following waiting time and H_2 release has been calculated and recorded by GRC system as starting wt% value of the PCId run: this is the cause of the incorrect absolute wt% values reported; no additive corrections over absolute wt% value have been applied.

A full interpretation of experimental results requests to identify the chemical reaction involved in hydrogen release and relative stoichiometry.

Reactions can be identified by comparison of the equilibrium pressure of isothermal measurements with literature data; this comparison can be easily performed reporting these parameters on a Van't Hoff plot where, according to Van't Hoff equation, for the same reaction every couple *equilibrium pressure / temperature* is placed on the same straight line.

Dynamic decomposition data show the sample's behavior at different pressure and in particular they report the H_2 release temperature for a certain overpressure. Being non-equilibium decomposition, the temperature corresponding to

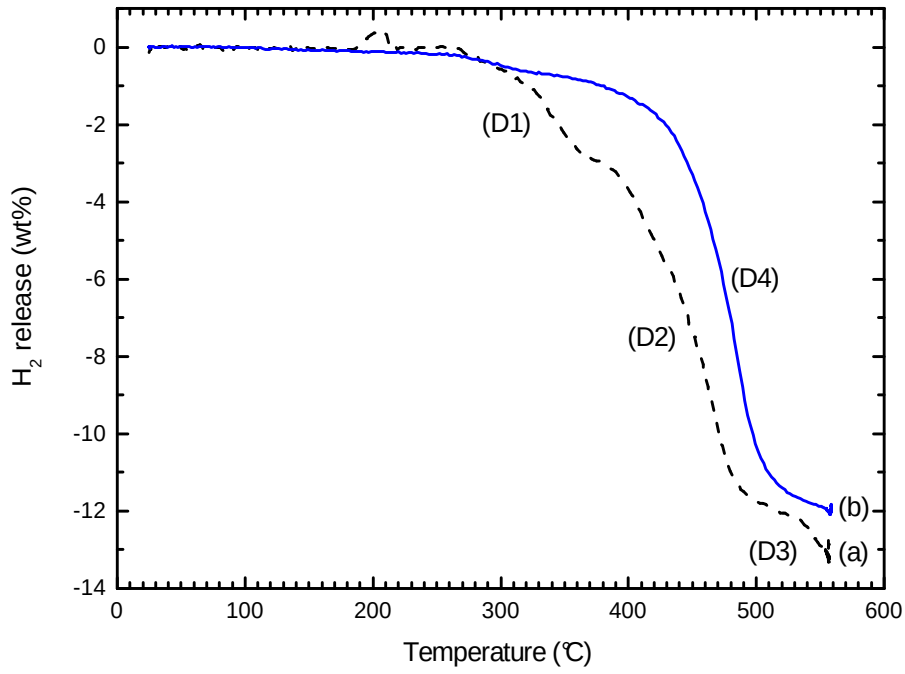

Figure 5.11: dynamic decomposition experiments of $LiBH_4$ performed under 3 bar H_2 backpressures; sample in contact with quartz wool (a), or with a stainless steel sponge (b).

the middle point of the gas evolution process is actually an overestimation of real equilibrium temperature. So the positioning of these couple *pressure / release temperature* on a Van't Hoff plot are expected to be shifted towards higher temperature values if compared to equilibrium data, expecially in case of reactions with slow kinetic.

5.3.1 Decomposition of $LiBH_4$

Dynamic decomposition experiments at increasing temperature of $LiBH_4$ (density 0.666 g/cc as reported by producer) have been performed under 3 bar H_2 backpressure; result is reported in Figure 5.11a.

The result was actually not coherent to TG data due to an interaction of $LiBH_4$ after melting with the quartz wool used for retaining the sample: three different decomposition reaction are clearly visible (D1 centered at 335°C, D2 at 450°C and D3 at 535°C) while only one should appear; the catalytic effect of SiO_2 on $LiBH_4$ was already reported by Zuettel *et al.* [59].

The problem was solved using a stainless steel sponge instead of quartz wool; the decomposition profile performed under the same initial condition (backpres-

sure pressure from 3 to 6.4 bar) is reported in the same Figure as line *b*: only one hydrogen desorption is present (D4 at T=475°C and p=5.0 bar).

Three Pressure Composition Isotherm decompositions experiments have been performed on $LiBH_4$ at 433°, 483° and 537°C.

Result PCI plot is showed in Figure 5.12; a detail of pressure *plateau* for decomposition at 433°C is reported in Figure 5.5b; Table 5.3 reports temperature, estimated equilibrium pressure and hydrogen release obtained from PCId data for $LiBH_4$; these data have been inserted in a Van't Hoff plot reported in Figure 5.13 (full circles).

$LiBH_4$ melts at 288.1°C, then the dehydriding reaction accompanied by the phase decomposition proceeds mainly above 450°C according to the following equation [60]

$$LiBH_4 \rightarrow LiH + B + 3/2H_2 \qquad (13.7\text{wt}\%), \tag{5.18}$$

so 13.7wt% is the expected total amount of released gas.

In Figure 5.13, equilibrium pressures for $LiBH_4$ are correctly placed over the corresponding reaction data (eq. 5.18) confirming the correct behavior of lithium borohydride in our Sievert's Apparatus;

As already described, GrcLV software calculates the released amount of gas expressed in wt% from pressure change over time, applying calibration correction for compensating the non-ideal behavior of gas and specific features of GRC design. Nevertheless the main problem of GRC system is a wrong interpretation of gas expansion during high pressure non-isothermal stages; in case of dynamic decomposition reactions, one manual subtraction of blank test data (reported in fig. 5.10) has been performed.

Observing dynamic decomposition of $LiBH_4$ (fig.5.11), the general reliability of collected wt% value can be verified considering the total amount of released gas. The decomposition with initial 3 bar backpressure reported in 5.11b shows a final amount of released gas equal to 12wt%. Admitting that the decomposition reaction at 6.4 bar and 550°C is completed according to eq. 5.18, the experimental value is around 1.7wt% (12%) smaller than expected. It means that in this pressure conditions the gas release is underestimated by mean of 15% of measured value.

In case of PCI decomposition (fig. 5.12), although the gas release of *plateau* is always smaller, the overall hydrogen release at 433° and 483°C is 11wt% confirming that a similar underestimation is present and needs to be corrected for

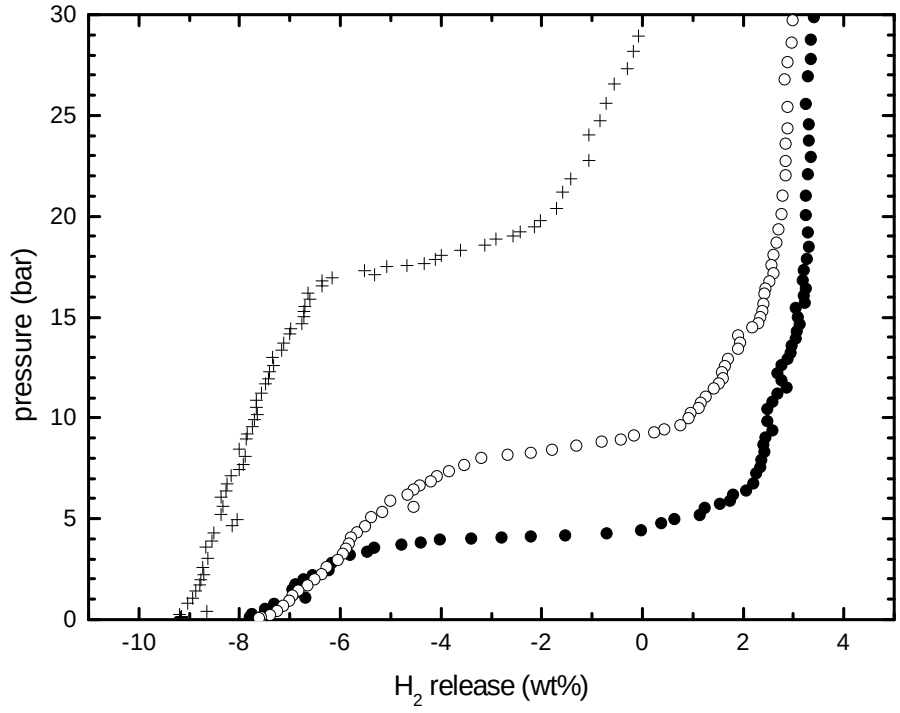

Figure 5.12: Pressure Composition Isotherm decompositions of $LiBH_4$ performed at 433°C (•), 483°C (◦) and 537°C (+).

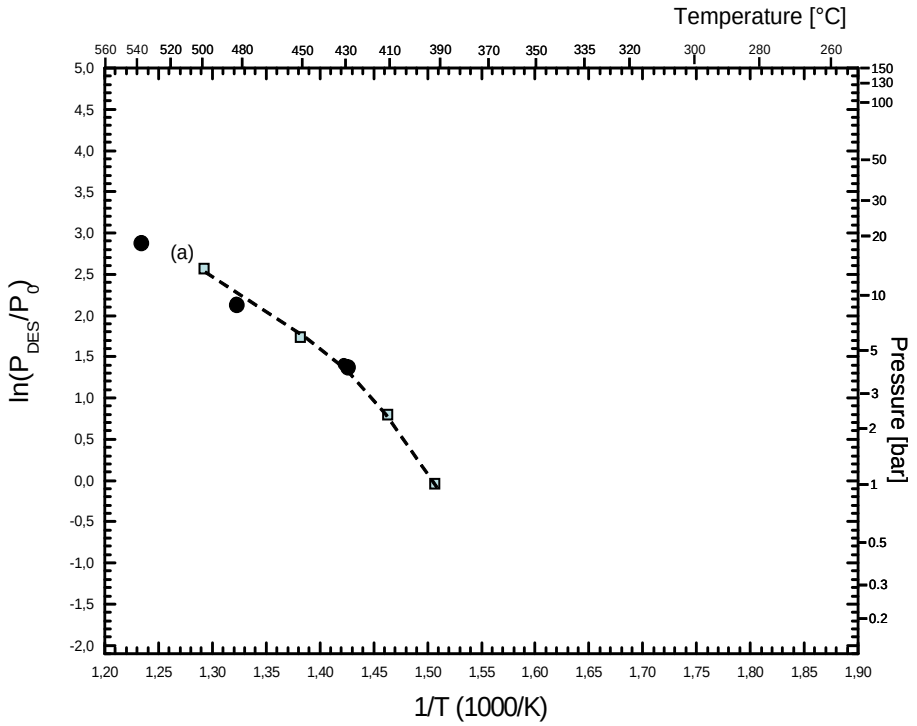

Figure 5.13: Van't Hoff plot in range P from 0.1 to 150 bar, T from 250 to 560°C; equilibrium pressure at corresponding temperature are reported for $LiBH_4$ (full circles); literature data are reported for chemical reactions 5.18 [60].

temperature (°C, K)	1/T (1/K)	pressure (bar)	ln(P/0.1MPa)	H_2 release (wt)%
433, 706.15	1.42	4.1	1.41	8.2
483, 756.15	1.32	8.6	2.15	7.2
537, 810.15	1.23	18.0	2.89	4.7

Table 5.3: Pressure and temperature estimation for $LiBH_4$ decomposed in GRC system.

chemical interpretation of these data; the overall hydrogen release at 537°C is 10wt%.

Van't Hoff equation (5.2) applied to straight line fitting the data (min square method, R^2=0.9988) returns $\Delta_r H$=65.4 kJ mol^{-1} H_2 for reaction enthalpy of decomposition according to Equation 5.18; Zuettel [31] reported enthalpy of reaction value $\Delta_r H$=74 kJ mol^{-1} H_2 and entropy of reaction value $\Delta_r S$=115 J K^{-1} mol^{-1} H_2 and decomposition data are reported in Figure 5.13a.

5.3.2 Decomposition of $Mg(BH_4)_2$

Dynamic decomposition experiments at increasing temperature of $Mg(BH_4)_2$ (density 0.780 g/cc as reported by Cerny [5]) have been performed from 25 to 555°C (2 K min^{-1}) under 3, 30 and 60 bar H_2 pressure using a stainless steel sponge for retaining the powder.

Hydrogen release has been calculated in real time by the GrcLV software, then numerical values have been elaborated: corresponding calibration values already reported in Figure 5.10 have been subtracted in temperature range 25-560°C and data have been vertically shifted in order to have a wt% average value equal to zero in temperature range 25-185°C, where no reaction is expected. Results are reported in Figure 5.14, and Table 5.4 summarizes the hydrogen release of every decomposition step. Three different processes (D1-3) confirm the presence of a multi step reaction, coherently with DSC peaks reported in Figure 4.3m for pure magnesium borohydride decomposition.

Gas release at 560°C on a line will not be taken in account being probably consequence of an instrumental error connected to GRC behavior at this temperature. Remaining dynamic data with pressure ranging from 3.8 to 5.6 bar can be compared to DSC profiles of $Mg(BH_4)_2$ performed at 5 bar H_2 and reported in lines m and l of Figure 4.3: the D3 desorption at 370°C is placed between endothermic peaks 8-9 of DSC profile (at 365° and 410°C respectively). Actually the shape of the gas evolution process suggests a fast kinetic which is more consistent with the sharp peak 9. Moreover, no other gas release are present over 420°C and consequently no other endothermic DSC peaks are expected.

Decomposition at higher pressure correctly shifts the same process towards higher temperatures. The D3 feature is quite sharp at high pressure (30 and 60 bar curves) but it becomes broader and worst defined at 3 bar. Also the D1 and D2 processes are hardly separated from each other at low pressure and better distinguished at the highest pressure of 60 bar.

A simple decomposition pathway of $Mg(BH_4)_2$ (fig. 5.16A) was been proposed by Matsunaga [30] on the basis of xray diffraction data, and it was generally accepted. The following two different steps are involved

$$Mg(BH_4)_2 \rightarrow MgH_2 + 2B + 3H_2 \text{ (-11.1wt\%)} \quad (5.19)$$

$$MgH_2 \rightarrow Mg + H_2 \text{ (-3.7wt\%)} \quad (5.20)$$

The first step is consistent with the D3 feature, whereas the first one roughly correspond to the D1+D2 process without accounting yet for the separation in two parts.

The Van't Hoff plots based on features D1, D2, D3 of the dynamic decompositions of $Mg(BH_4)_2$ are shown in Figure 5.15. In reference to Figure 5.14 can be observed that D3 release at 30 and 60 bar has a fast kinetic and consequently it

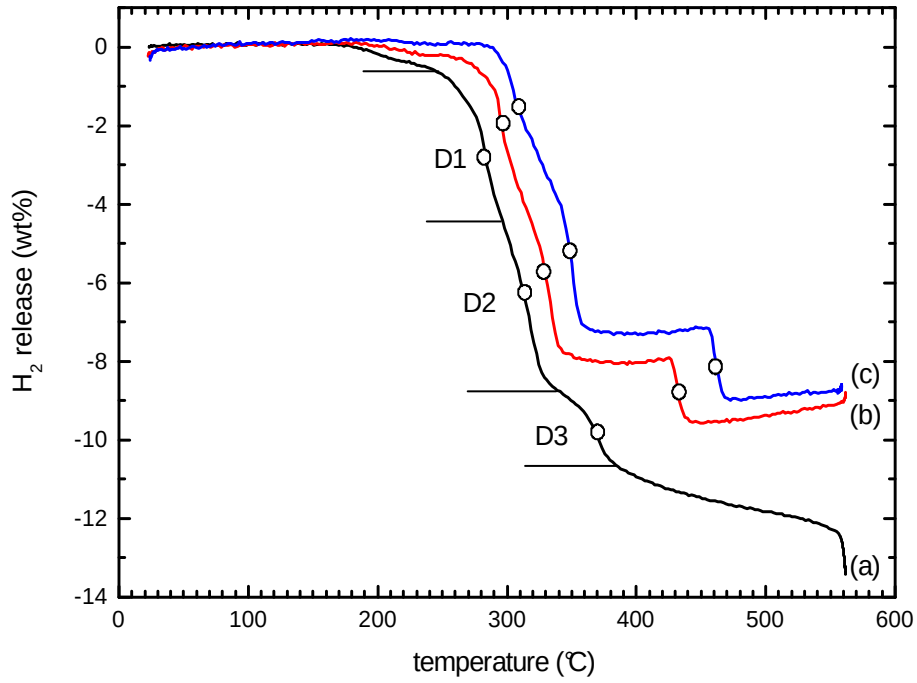

Figure 5.14: dynamic decomposition experiments of $Mg(BH_4)_2$ performed under different H_2 backpressures; 3 bar (a), 30 bar (b) and 60 bar (c); inflection points are identified by open circles.

presents a small overestimation of release temperature; this favorable condition places his P/T points for these two pressures almost exactly over the reaction 5.31, allowing us to attributed it to MgH_2 decomposition.

Releases labeled D1 and D2 has to be considered caused by two different intermediate decompositions of $[BH4]^-$ group and forming MgH_2.

H.-W Li [23] observed a double *plateau* during a PCI decomposition of the same material and suggested the partial formation of $[B_{12}H_{12}]^{2-}$ (fig. 5.16B) for explaining the B-H bending and stretching modes observed in Raman spectra of rehydrided sample (543K in hydrogen at 40 Mpa for 48 hours):

$$Mg(BH_4)_2 \rightarrow 5/6MgH_2 + 1/6MgB_{12}H_{12} + 13/6H_2 \rightarrow \quad (5.21)$$

$$\rightarrow 5/6Mg + 1/6MgB_{12}H_{12} + 3H_2 \rightarrow \quad (5.22)$$

$$\rightarrow 5/6Mg + nMgB_2 + mB + 4H_2. \quad (5.23)$$

Actually the proposed stoichiometric coefficient for MgH_2 is not consistent with the registered amount of released hydrogen and still does not explain the D1-D2 two step ovolution of gas observed before the D3 MgH_2 decomposition.

line	pressure (bar)	temperature (°C)	ID	H_2 release (wt%)
(a)	3.84	283	D1	4.8
3 bar	4.96	319	D2	4.0
	5.66	370	D3	1.9
(b)	33.4	295	D1	3.9
30 bar	34.7	333	D2	4.1
	35.9	431	D3	1.7
(c)	66.3	305	D1	3.6
60 bar	68.3	352	D2	3.5
	70.2	460	D3	1.8

Table 5.4: H_2 release by $Mg(BH_4)_2$ from dynamic decomposition plots reported in Figure 5.14.

step	temperature (°C, K)	1/T (1/K)	pressure (bar)	ln(P/0.1MPa)	H_2 release (wt%)
D1	283, 556	1.80	3.85	1.34	4.8
	295, 568	1.76	33.4	3.50	3.9
	305, 578	1.73	66.4	4.19	3.6
D2	319, 592	1.69	4.96	1.60	4.0
	333, 606	1.64	34.7	3.55	4.1
	349, 622	1.60	68.2	4.22	3.5
D3	370, 643	1.55	5.66	1.73	1.9
	431, 704	1.41	35.9	3.58	1.7
	460, 733	1.36	70.2	4.25	1.8

Table 5.5: data for the Van't Hoff plots of the D1-D3 steps of $Mg(BH_4)_2$ dynamic decomposition (Figure 5.15).

A chemical decomposition pathway (fig. 5.16C) has been proposed by Soloveichik [48] for explaining the observed hydrogen evolution steps D1 and D2 in a Volumetric Temperature Programmed experiment performed in a Sievert's Apparatus. This hypothesis suggests the formation of polyborane species MgB_nH_m with hydrogen content calculated from the amount of desorbed gas (4.8 and 4.9 wt%, respectively), plus amorphous MgB_4 detected by ^{11}B NMR. Thus, the following reactions would explain the D1-D2 features observed in our dynamic decomposition results:

$$Mg(BH_4)_2 \rightarrow \text{“}MgB_2H_{5.5}\text{”} \text{ (D1 – 4.8wt\%)} \quad (5.24)$$

$$\text{“}MgB_2H_{5.5}\text{”} \rightarrow \text{“}MgBH_{2.5}\text{”} + MgB_4 \text{ (D2 – 4.9wt\%).} \quad (5.25)$$

The next step involves the formation of amorphous $MgB_{12}H_{12}$ (detected by

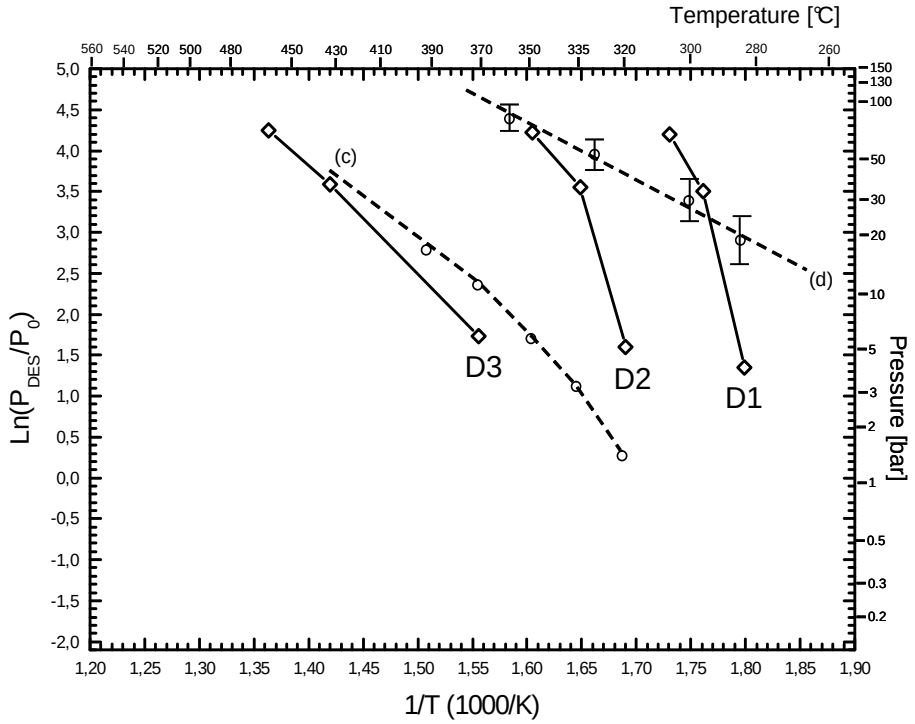

Figure 5.15: Van't Hoff plots for the D1, D2 and D3 steps of the dynamic decomposition of $Mg(BH_4)_2$ (full lines); the (c) and (d) dashed lines denote plots for reactions 5.19 and 5.20 from literature data [23].

NMR), and crystalline MgH_2 (observed by XRD) which are appearing simultaneously after the exothermic effect:

$$\text{“}MgBH_{2.5}\text{”} + MgB_4 \quad \rightarrow \quad xMgH_2 + 1/12MgB_{12}H_{12} + MgB_4. \qquad (5.26)$$

The next hydrogen desorption (2.8 wt%) would correspond to decomposition of MgH_2 process, according to :

$$\begin{aligned} & xMgH_2 + 1/12MgB_{12}H_{12} + MgB_4 \rightarrow \\ \rightarrow \quad & Mg + 1/12MgB_{12}H_{12} + MgB_4 + H_2 \text{ (D3 – 2.8wt\%.)} \end{aligned} \qquad (5.27)$$

The final decomposition step would account for the final H_2 release shown in the *a* curve of Figure 5.14.

$$1/12MgB_{12}H_{12} \quad \rightarrow \quad MgB_2 \text{ (2.7wt\%) .} \qquad (5.28)$$

There is not full agreement in literature on this reaction model and recently other pathways based on different intermediates have been proposed [57, 51].

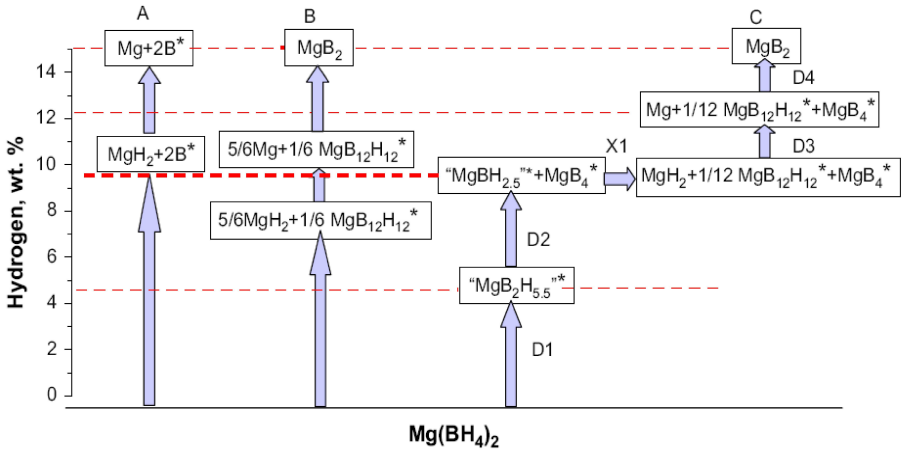

Figure 5.16: decomposition pathways of $Mg(BH_4)_2$ (amorphous phases denoted by asterisk, observed hydrogen evolution steps marked by dashed lines)[48].

Informations about stoichiometry can be deduced by evaluation of amount of released gas considering that the result is reported in wt% H_2 and the initial molar weight of the sample.

The final correction on overall H_2 release obtained by $LiBH_4$ dynamic decomposition can not be confirmed by consideration about overall H_2 release of $Mg(BH_4)_2$ at the same pressure, fig. 5.14a, because decomposition at 3 bar is not concluded when sample reaches the upper temperature limit of GRC system; anyway, considering the relative amount of H_2 released in D1, D2 and D3, there is a good agreement between our results summarized in Table 5.5 and experimental data reported by Soloveichik [48]; this agreement is confirmed by the underestimation correction except for D3 which is 1.9±0.1wt% and after the correction it's still 30% smaller than reported value (2.1 wt% instead of 2.8wt%). Actually no stoichiometric coefficient was proposed for MgH_2 decomposition of proposed 5.16C pathway.

If all Mg is converted to MgH_2 by reaction 5.19 and then decomposed, the amount of released hydrogen for reaction 5.20 is 3.7wt%; considering the value of D3 gas evolution 2.1wt% (already corrected), the calculated stoichiometric coefficient is x=0.56 .

Isothermal decomposition of α-magnesium borohydride has been performed at 281° and 307°C in PCId mode with optimal settling conditions identified in paragraph 5.2.6; results are reported in Figure 5.17. Table 5.6 reports temperature, estimated equilibrium pressure and hydrogen release of reaction step obtained from PCId data for $Mg(BH_4)_2$; these data have been inserted in a Van't Hoff plot reported in Figure 5.18 (full diamonds identify D2 and D3 decompo-

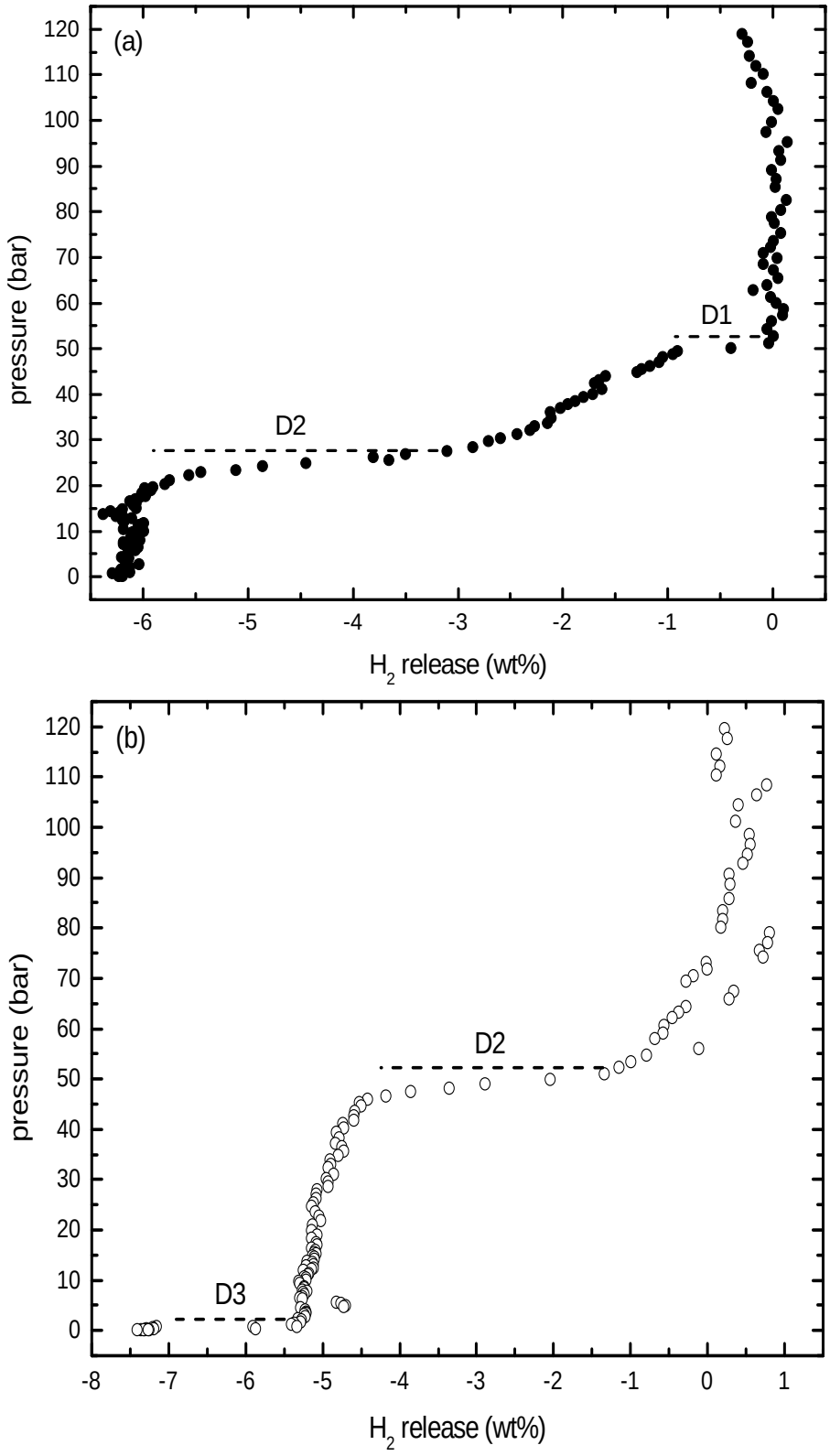

Figure 5.17: PCId measurements of $Mg(BH_4)_2$ performed at 281°C (a) and 307°C (b).

temperature (°C, K)	1/T (1/K)	pressure (bar)	ln(P/0.1MPa)	H_2 release (wt%)
285, 558.15	1.79	50.0	3.91	1.1
		27.5	3.31	4.1
307, 580.15	1.72	51.0	3.93	1.2
		0.7	-0.35	1.8

Table 5.6: Pressure and temperature estimation for $Mg(BH_4)_2$ decomposed in GRC system.

sition *plateau*; empty diamond identifies the D1 decomposition *plateau* at 281°C).

Van't Hoff equation (5.2) applied to straight line connecting D2 data returns $\Delta_r H$=63.2 kJ mol^{-}1 H_2 for reaction enthalpy; Matsunaga [30] reported an enthalpy of reaction value $\Delta_r H$=39.3 kJ mol^{-}1 H_2 for the first step reaction reported in Eq. 5.19; H.-W Li [23] reported for the same reaction $\Delta_r H$=57±5 kJ mol^{-}1 H_2 . Main cause of the incoherence between results and literature data could be the presence of only two experimental data point.

Since no other PCId data are available, values by H.-W Li [23] have been reported in fig. 5.18; equilibrium pressure observed for the D2 *plateau* decomposition at 281°C is within the experimental error of these data, while the equilibrium pressure of D1 *plateau* is outside this range. Equilibrium pressure observed for D2 decomposition at 307°C is higher than expected but the different measurements performed with more strict settling condition showing an increase of this parameter confirm us the reliability of finally observed value; D3 *plateau* pressure at 307°C is coherent with expected result for decomposition reaction of MgH_2.

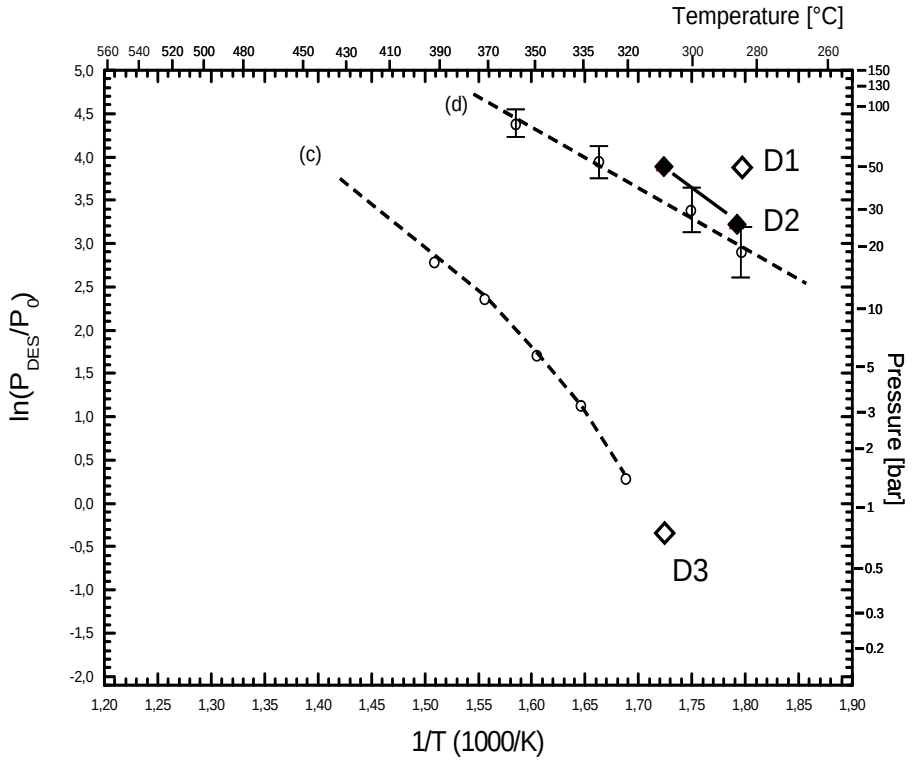

Figure 5.18: Van't Hoff plot for the D2 step of the isothermal (equilibrium) decomposition of $Mg(BH_4)_2$ (full line); single D1 and D3 data are indicated by isolated open diamonds; the (c) and (d) dashed lines denote plots for reactions 5.19 and 5.20 from literature data [23].

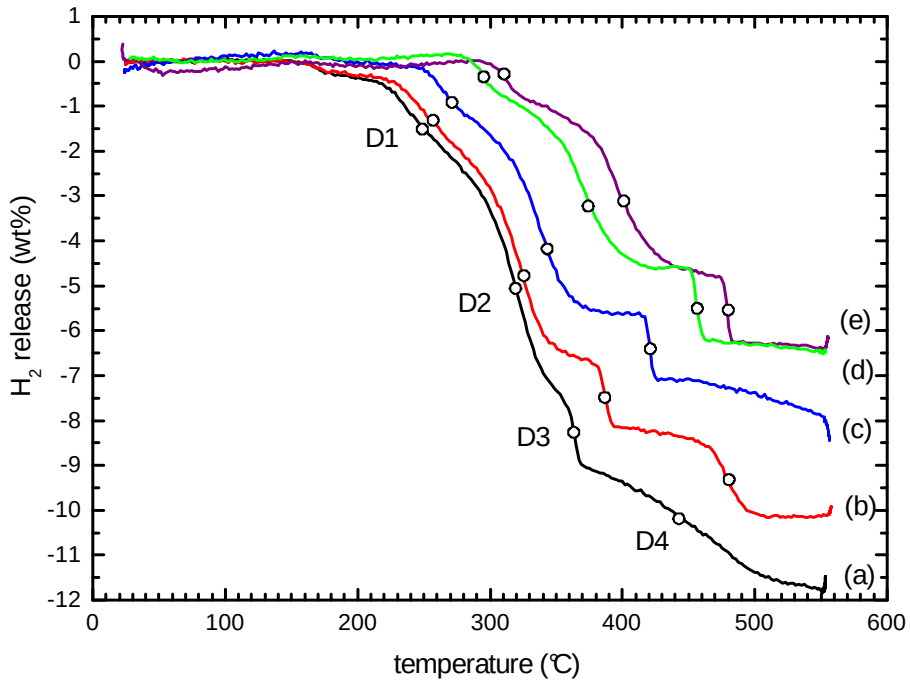

Figure 5.19: dynamic decomposition plots of $0.6LiBH_4$–$0.4Mg(BH_4)_2$ (eutectic composite) performed under different H_2 pressures; 3 bar (a), 10 bar (b), 30 bar (c), 60 bar (d) and 90 bar (e). Different hydrogen release steps are identified with labels (D1-D4); the corresponding inflection points are denoted by empty circles.

5.3.3 Decomposition of the eutectic mixture $0.6\mathbf{LiBH_4}$–$0.4\mathbf{Mg(BH_4)_2}$

Dynamic decomposition experiments of xLiBH$_4$–(1-x)Mg(BH$_4$)$_2$ with $x = 0.6$ have been performed at increasing temperature from 25 to 550°C with heating rate of 2 K/min using a stainless steel sponge for retaining the powder (weight: 50 mg); different H_2 backpressures have been loaded on the sample chamber: 5, 10, 30, 60 and 90 bar; every 60 seconds thermodynamic parameters have been acquired.

Hydrogen release has been calculated in real time by the GrcLV software, then numerical values has been elaborated: corresponding calibration values already reported in Figure 5.10 have been subtracted in temperature range 25-555°C and data have been vertically shifted in order to have a wt% average value equal to zero in temperature range 25-185°C, where no reaction is expected. Result is showed in Figure 5.19 where different reaction steps are identified with labels (D1-D4) and Table 5.7 summarizes the hydrogen release of every decomposition step observed.

Decomposition at higher pressure correctly shifts the same process towards

line	pressure bar	temperature (°C)	ID	H_2 release wt%
(a)	3.46	234	D1	2.6
3 bar	4.37	320	D2	4.7
	5.03	363	D3	1.7
	5.70	481	D4	2.7
(b)	11.6	242	D1	2.3
10 bar	12.3	324	D2	4.3
	13.1	387	D3	1.6
	13.8	477	D4	2.0
(c)	32.7	263	D1	1.8
30 bar	33.8	335	D2	3.8
	34.9	421	D3	1.5
	36.0	552	D4	-.-
(d)	65.8	294	D1	1.1
60 bar	67.5	370	D2	3.5
	69.2	455	D3	1.7
(e)	99.2	312	D1	1.2
90 bar	101	396	D2	3.6
	103	478	D3	1.5

Table 5.7: H_2 release by eutectic mixture calculated from dynamic data reported in Figure 5.19.

higher temperatures; lines *a* and *b* show D4 release which is not visible for other pressure and the same phenomena changes his shape moving from 3 to 10 bar H_2 backpressure; D1 and D2 change his shape reducing the H_2 release and thus confirm the overall decrease of gas loss from 3 to 60 bar. On the other hand D3 profile remains constant with pressure. The two plots at 60 and 90 bar are almost equal for intensity and only shifted for temperature.

The Van'T Hoff plots of dynamic decompositions results are shown in Figure 5.20, together with the plots taken from literature for the following dehydrogenation reactions:

$$\text{(a) [60]} \quad - \quad LiBH_4 \rightarrow LiH + B + 3/2H_2 \tag{5.29}$$

$$\text{(b) [49]} \quad - \quad LiBH_4 + 1/2MgH_2 \rightarrow LiH + 1/2MgB_2 + 2H_2 \tag{5.30}$$

$$\text{(c) [23]} \quad - \quad MgH_2 \rightarrow Mg + H_2 \tag{5.31}$$

$$\text{(d) [23]} \quad - \quad Mg(BH_4)_2 \rightarrow MgH_2 + 2B + 3H_2. \tag{5.32}$$

Reactions (a), (c) and (d) have been already described in sections 5.3.1-5.3.2 in the

step	temperature (°C, K)	1/T (1/K)	pressure (bar)	ln(P/0.1MPa)	H_2 release (wt%)
D1	234, 507	1.97	3.46	1.24	2.6
	242, 515	1.94	11.0	2.40	2.3
	263, 536	1.86	32.7	3.49	1.8
	294, 567	1.76	65.8	4.19	1.1
	312, 586	1.71	99.2	4.60	1.2
D2	320, 593	1.68	4.3	1.47	4.7
	324, 597	1.67	12.3	2.51	4.3
	335, 608	1.64	33.8	3.52	3.8
	369, 642	1.55	67.5	4.21	3.5
	394, 667	1.50	101.4	4.62	3.6
D3	363, 636	1.57	5.03	1.61	1.7
	387, 660	1.51	13.1	2.58	1.6
	420, 694	1.44	34.9	3.55	1.5
	455, 729	1.37	69.2	4.24	1.7
	478, 752	1.33	103.4	4.64	1.5
D4	448, 721	1.39	5.53	1.71	1.7
	478, 751	1.33	13.8	2.62	1.6

Table 5.8: data for the Van't Hoff plots of the D2-D5 steps of eutectic mixture dynamic decomposition (Figure 5.20).

decomposition of $LiBH_4$ and $Mg(BH_4)_2$. The reaction (b) was identified by Vajo [49] who showed that by making $LiBH_4$ react with MgH_2, the dehydrogenation of lithium borohydride is thermodynamically favoured, thanks by the great stability of MgB_2.

The Van't Hoff plots corresponding to the D1-D4 steps od dynamic decomposition of the eutectic composite (Figure 5.20) where obtained by the points of inflection prints in Figure 5.19. The plots of reactions (a)-(d) from literature data were determined on the basis of isothermal (equilibrium) measurements, so that by comparison our plots from dynamic results are expected to be more or less shifted at higher temperature for Kinetic delay (see the decomposition of $Mg(BH_4)_2$ results in 5.3.2). The D3 release has a fast kinetic (sharp shape in Figure 5.19) so that it fits quite well the (c) curve in Figure 5.20 and it can be interpreted as due to reaction 5.31 of MgH_2 decomposition. The D1 and D2 H_2 releases should be considered as two close steps of the decomposition of the $[BH_4]^-$ borohydride anions forming MgH_2. Eventually, the D4 process can be ascribed to reaction 5.30 involving the $LiBH_4$ decomposition assisted by MgH_2.

Eutectic mixture with Li:Mg ratio equal to 0.6:0.4 has raw formula $Li_{0.6}Mg_{0.4}(BH_4)_{1.4}$ and its molar weight is 34.9 g/mole; if all Mg were converted to MgH_2

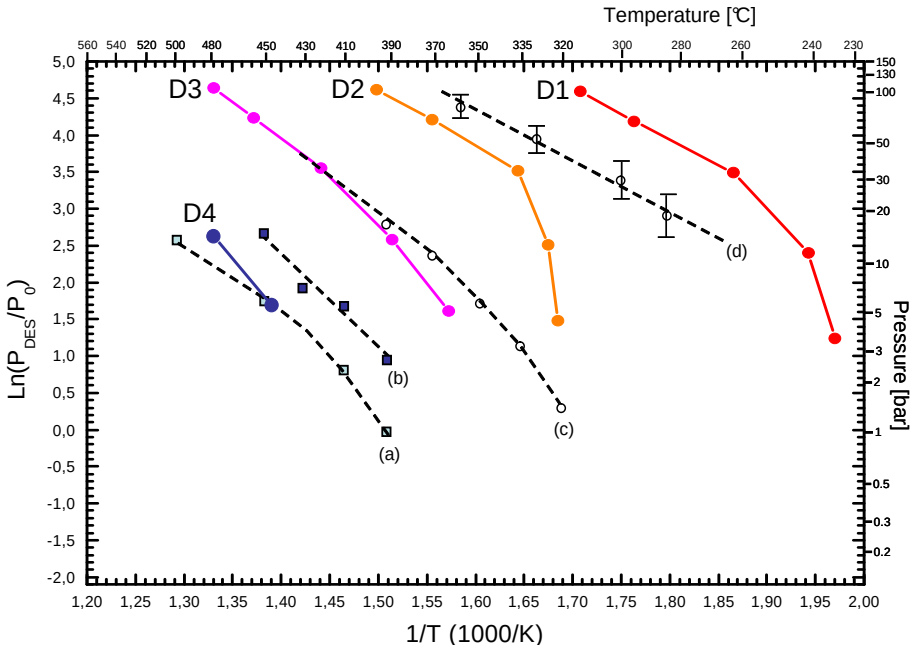

Figure 5.20: Van't Hoff plots for the D1, D2, D3 and D4 steps of the dynamic decomposition of $0.6LiBH_4$–$0.4Mg(BH_4)_2$ (full lines); dashed lines indicate the plot for reactions 5.29-5.32 from literature data (a [60], b [49], c [23], d [23]).

and were decomposed during gas release D4, the expected amount of released H_2 is 0.4 mole, corresponding to 0.8 g for 1 mole of sample and to 2.3wt% weight loss. The actual observed weight loss in dynamic decomposition is 1.6±0.1wt% and after correction it becomes 1.84wt%. This calculation suggests that 80% of Mg reacts producing MgH_2.

PCI decomposition isotherms of the eutectic mixture (weight: 100mg) have been measured at 313°, 369° and 433°C; settling conditions are fixed at dP=0.02 bar and t_{max}=33 min; non-equilibrium data recording every 60 seconds.

Results are shown in Figure 5.21 where different decomposition *plateaus* at decreasing pressure on the same isotherm confirm a multi step decomposition process. Table 5.9 reports temperature and estimated equilibrium pressure obtained from PCI results. These data have been inserted in three Van't Hoff plots (open circles) reported in Figure 5.22 where plots for reactions 5.29-5.32 from literature data (dashed lines) are shown, too. A quite good correspondence of our data with the (b), (c) and (d) lines is observed. Thus, taking also into account the result of the dynamic measurements (Figure 5.20), the three steps of dehydrogenation have been labelled as D1-2 (d), D3 (c), D4 (b).

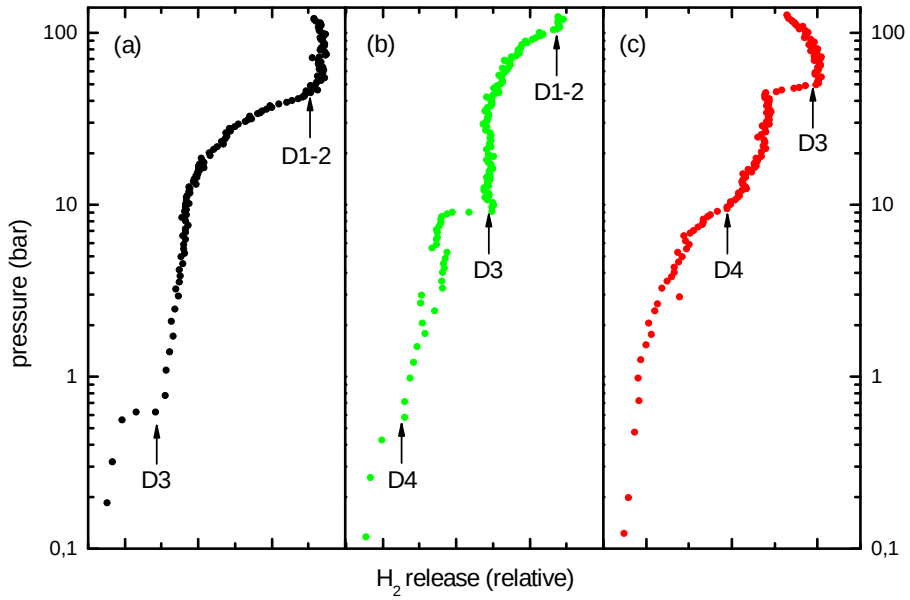

Figure 5.21: Pressure Composition Isotherm (PCI) decompositions of $0.6LiBH_4$–$0.4Mg(BH_4)_2$ performed at different temperatures; 313°C (a), 369°C (b), 433°C (c); *plateau* data are reported in Table 5.9.

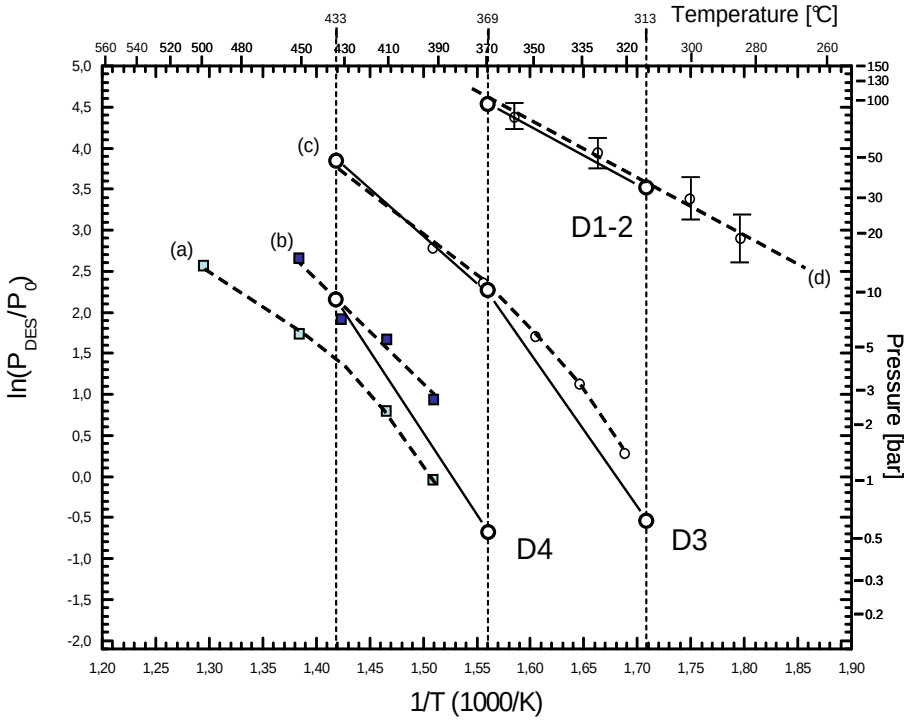

Figure 5.22: Van't Hoff plot for the D1-2, D3 and D4 steps of the isothermal (equilibrium) decomposition of $0.6LiBH_4$–$0.4Mg(BH_4)_2$ (full lines); dashed lines indicate the plot for reactions 5.29-5.32 from literature data (a [60], b [49], c [23], d [23]).

temperature (°C, K)	1/T (1/K)	pressure (bar)	ln(P/0.1MPa)	ID
313, 586.15	1.71	0.6	-0.51	D3
		44	3.78	D1-2
369, 642.15	1.56	0.5	-0.69	D4
		9.1	2.21	D3
		103	4.63	D1-2
433, 706.15	1.42	10.6	2.36	D4
		49.7	3.90	D3

Table 5.9: data for the Van't Hoff plots of the different steps of the eutectic mixture PCI decomposition (Figure 5.22); rif. Figure 5.21.

In order to compare the decomposition behavior of the $0.6LiBH_4$–$0.4Mg(BH_4)_2$ eutectic mixture with that of the two end members, the dynamic dehydrogenation profile measured at 3 bar (see Figure 5.19) was reported in Figure 5.23 together with the dynamic profiles at 3 bar for $LiBH_4$ and $Mg(BH_4)_2$, and for their 0.6/0.4 weighted average.

One can see that the behavior of the eutectic mixture is much more similar to that of pure $Mg(BH_4)_2$ than to that of the weighted average. This is surprising considering the larger content in Li than in Mg. Further, dehydrogenation of the eutectic starts at a lower temperature ($\approx$ 200°C) than for $Mg(BH_4)_2$ itself, thus suggesting a possible better performance also in practical dehydrogenation operations.

An article reporting these results is actually in preparation [1].

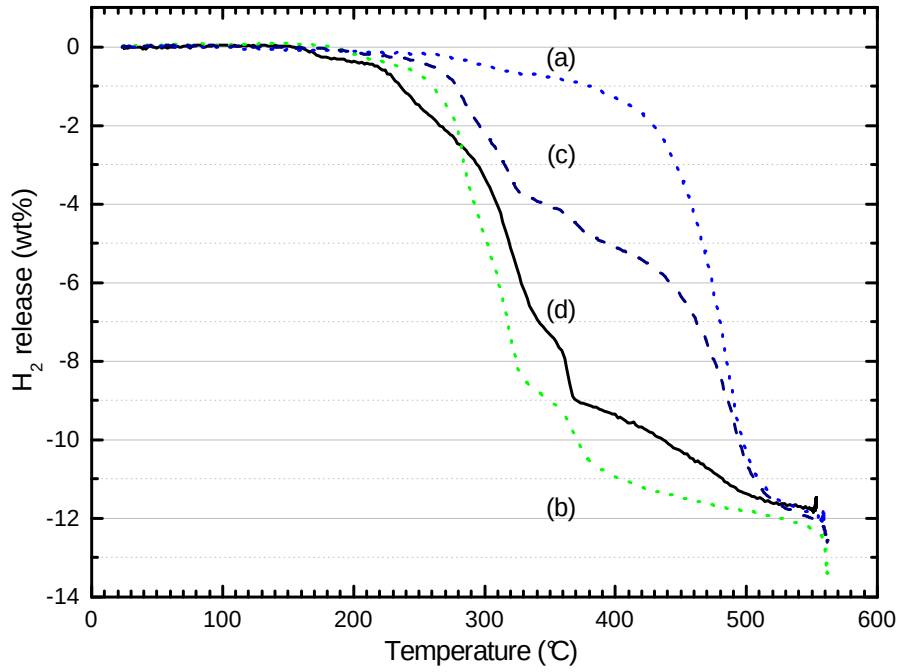

Figure 5.23: dynamic dehydrogenation profile measured at 3 bar of $LiBH_4$ (a), $Mg(BH_4)_2$ (b) and their 0.6/0.4 weighted average (c) toghether with the experimental result for $0.6LiBH_4$–$0.4Mg(BH_4)_2$ (d).

Chapter 6

Conclusions

In this thesis work a number of experimental results were obtained on two important classes of materials for hydrogen storage: ball-milled Mg-Al-Ni alloys and Li-Mg borohydrides. The common aim was to improve the thermodynamic and kinetic features of hydrogen release of the H-storage material by suitable chemical tailoring.

In the case of metal alloys, this was achieved by introducing aluminium into the well known Mg-Ni system, exploring a range of compositions, determining the phase stability diagram, and measuring the hydrogenation/dehydrogenation properties of the Mg_2AlNi_2 pseudo-BCC phase. Such a compound proved to react with hydrogen, forming a mixture of the MgH_2 and Mg_2NiH_4 hydrides with a Mg-poorer p-BCC solid solution. About 1.4 wt% of H_2 is absorbed/desorbed reversibly for several cycles; hydrogen is released at 258 °C at a pressure higher or equal to 1 bar. Although the quantity of stored hydrogen is limited, *the temperature of H2 release for hydrogenated Mg_2AlNi_2 is significantly lower than for pure MgH_2 or Mg_2NiH_4* (above 300 °C). This indicates that appreciable improvements not only in the kinetics, but also in the thermodynamics of the MgH_2 dehydrogenation process can be achieved, by producing the hydride in a convenient chemical-physical environment.

More work was dedicated to the borohydride system, which is so interesting for the very large amount of (though not reversibly) over 10 wt% stored hydrogen. The focus was put on the synergy effect of mixing together two of the most important compounds, $LiBH_4$ and $Mg(BH_4)_2$. In the first part of the study, different synthesis techniques were attempted for the mixed lithium—magnesium borohydride system, finding that *dry ball milling gives better results with respect to solution methods in ethers.* Detailed X-ray diffraction and DSC measurements on xLiBH$_4$ –(1-x)Mg(BH$_4$)$_2$ samples showed that in all cases a physical mixture of the two components is formed, rather than a new compound. In particular,

an eutectic composition was determined in the phase diagram between $x = 0.5$ and 0.6. The decomposition of the eutectic mixture begins just after melting at 180 °C; thus in this case hydrogen is released at a much lower temperature than by pure borohydrides. At 270 °C the $0.5LiBH_4$-$0.5Mg(BH_4)_2$ composite releases 7.0 wt% of hydrogen.

Furthermore, the kinetics of the α/β polymorphic transformation of $Mg(BH_4)_2$ proved to be affected by just a small amount of $LiBH_4$, so that the orthorhombic phase (high temperature modification) can be reversibly transformed in the hexagonal phase (low temperature modification) in the mixed xLiBH$_4$–(1-x) $Mg(BH_4)_2$ system, unlike what happens for pure $Mg(BH_4)_2$.

Dehydrogenation experiments were performed on the eutectic mixture $0.6LiBH_4$ $–0.4Mg(BH_4)_2$ and on the pure lithium and magnesium end members, both by dynamic (isobaric) and by equilibrium (isothermal) techniques. A substantial agreement is observed between results obtained by the two different methods. The main outcome of such measurements is that the decomposition process of the eutectic mixture follows a complex mechanism in four steps (D1, D2, D3, D4), which partly resembles that of pure magnesium borohydride despite the large fraction of lithium end-member. The most significant and interesting difference is that the eutectic dehydrogenation starts at a lower temperature with respect to $Mg(BH_4)_2$. This fully confirms the results of DSC measurements and shows a promising behavior of the eutectic composite for applications, as the decomposition temperature of the H-storage material is required to be as low as possible (though above room temperature).

As the multi-step dehydrogenation mechanism of the $Mg(BH_4)_2$ end-member itself is still debated in the literature, the present results can give a useful contribution to this topic, and to the parallel one of the effect of the $LiBH_4$ fraction on such a mechanism. In summary, the first part of the decomposition reaction involves the formation of MgH_2 in two steps (D1 and D2), with a probable intermediate compound of MgB_nH_m magnesium polyborane composition. The second part is based on the final dehydrogenation of magnesium hydride, occurring with two distinct reactions: a plain decomposition to Mg metal (D3), and a $LiBH_4$-assisted dehydrogenation leading to LiH and MgB_2 (D4). Thus, the high-temperature decomposition of $LiBH_4$ alone is not observed, because all lithium borohydride is consumed in the complex reaction with MgH_2. This explains why the overall decomposition profile of the eutectic composite has little similarity with that of $LiBH_4$.

More work will be needed in the future to better clarify the first part of the decomposition reaction, and in particular the positive role of $LiBH_4$ in lowering the starting temperature of the process, possibly due to a participation to the formation of intermediate polyboranes.

Bibliography

[1] A. Nale, M. Catti, E.G. Bardaji and M. Fichtner. *In preparation.* [cited at p. 83]

[2] A. Parente, A. Nale, M. Catti, E. Kopnin and P. Caracino. Hydrogenation properties of Mg_2AlNi_2 and mechanical alloying in the Mg–Al–Ni system. *J. Alloys Comp.*, 477(1-2):420–424, 2009. [cited at p. 19]

[3] S. Bouaricha and R. Schulz. Hydriding behavior of Mg–Al and leached Mg–Al compounds prepared by high-energy ball-milling. *J. Alloys Comp.*, 297(1-2):282–293, 2000. [cited at p. 9]

[4] R.W. Cahn and E.J. Kramer. *Materials Science and Technology*, volume 3b. VCH, New York, 1994. [cited at p. 15]

[5] R. Cerný and K. Yvon. Magnesium borohydride : synthesis and crystal structure. *Angew. Chem. Int. Ed.*, 46(30):5765–5767, 2007. [cited at p. 70]

[6] P. Chen and K.L. Tan. Interaction of hydrogen with metal nitrides and imides. *Nature*, 420(6913):3–344, 2002. [cited at p. 23]

[7] K. Chlopek and M. Fichtner. Synthesis and properties of magnesium tetrahydroborate, $Mg(BH_4)_2$. *J. Mater. Chem.*, 17:3496–3503, 2007. [cited at p. 29, 31]

[8] E. G. Bardaji, Z. Zhao-Karger, N. Boucharat, M. Van Setten, W. Lohstroh, E. Roehm, A. Nale, M. Catti and Fichtner M. $LiBH_4$-$Mg(BH_4)_2$: A physical mixture of metal borohydrides as hydrogen storage material. *J. Phys. Chem. C, submitted.* [cited at p. 48]

[9] Z.Z. Fang and S.I. Orimo. Unexpected dehydrogenation behavior of $LiBH_4/Mg(BH_4)_2$ mixture associated with the in situ formation of dual-cation borohydride. *J. All. Comp.*, 491:L1, 2010. [cited at p. 24, 35]

[10] Y. Filinchuk and H. Hagemann. Insight into $Mg(BH_4)_2$ with synchrotron x-ray diffraction: structure revision, crystal chemistry, and anomalous thermal expansion. *Chem. Mater.*, 21(5):925–933, 2009. [cited at p. 38]

[11] A. Gasiorowski and M. Jurczyk. Hydriding properties of nanocrystalline $Mg_{2-x}M_xNi$ alloys synthesized by mechanical alloying (M=Mn, Al). *J. Alloys Comp.*, 364:283–288, 2004. [cited at p. 10, 19]

[12] J. Graetz and J.J. Reilly. Thermodynamics of the α β and γ polymorphs of (AlH_3). *J. Alloys Comp.*, 424(1-2):262–265, 2006. [cited at p. 9]

[13] H. Grove and B.C. Hauback. The structure of $LiMg(AlD_4)_3$. *J. All. Comp.*, 455:249–254, 2007. [cited at p. 31]

[14] H. Hagemann and C. M. Jensen. $LiSc(BH_4)_4$: A novel salt of Li^+ and discrete $Sc(BH_4)_4$- complex anions. *J. Phys. Chem. A*, 112:7551, 2008. [cited at p. 24]

[15] J.-H. Her and J.-C. Zhao. Structure of unsolvated magnesium borohydride $Mg(BH_4)_2$. *Acta Cryst.*, B63:561–568, 2007. [cited at p. 38]

[16] DOE hydrogen program homepage. http://www.hydrogen.energy.gov. [cited at p. 3]

[17] K.S. Jung and K.S. Lee. Catalytic effects of metal oxide on hydrogen absorption of magnesium metal hydride. *J. Alloys Comp.*, 421(1-2):179–184, 2006. [cited at p. 9]

[18] C. Kim and V. Ozolins. $LiSc(BH_4)_4$ as a hydrogen storage material: Multinuclear high-resolution solid-state nmr and first-principles density functional theory studies. *J. Phys. Chem. C*, 113:9956–9968, 2009. [cited at p. 24]

[19] J.H. Kim and Y.W. Cho. Reversible hydrogen storage in calcium borohydride $Ca(BH_4)_2$. *Scripta Materialia*, 58:481, 2008. [cited at p. 23]

[20] R Koester. Neue herstellungsmethoden für metallborhydride. *Angew. Chem.*, 3:94, 1957. (in German). [cited at p. 29]

[21] J. Kostka and H. Hahn. Diborane release from $LiBH_4$/silica-gel mixtures and the effect of additives. *J. Phys. Chem. C*, 111:14026, 2007. [cited at p. 42]

[22] J.Y. Lee and Y.W. Cho. Decomposition reactions and reversibility of the $LiBH_4$-$Ca(BH_4)_2$ composite. *J. Phys. Chem. C*, 113:15080, 2009. [cited at p. 24, 35]

[23] H.-W. Li and S.I. Orimo. Dehydriding and rehydriding processes of well-crystallized $Mg(BH_4)_2$ accompanying with formation of intermediate compounds. *Acta Materialia*, 56:1342–1347, 2008. [cited at p. 23, 71, 73, 76, 77, 79, 81, 82]

[24] H.W. Li and A. Züttel. Metastability and crystal structure of the bialkali complex metal borohydride $NaK(BH_4)_2$. *J. Alloys Comp.*, 446:315, 2007. [cited at p. 24]

[25] Q. Li and F. Zhan. Influence of the initial hydrogen pressure on the hydriding kinetics of the $Mg_{2-x}Al_xNi$ (x=0, 0.1) alloys. *Int. J. Hydrogen Energy*, 29(13):1383–1388, 2004. [cited at p. 9]

[26] Z.P. Li and S. Suda. Evaluation of alkaline borohydride solutions as the fuel for fuel cells. *J. Power Sources*, 126:28–33, 2004. [cited at p. 4]

[27] G. Liang and R. Shulz. Mechanical alloying and hydrogen absorption properties of the mg–ni system. *J. Alloys Comp.*, 267(1-2):302–306, 1998. [cited at p. 9]

[28] L.-P. Ma and H.-M. Cheng. Improving hydrogen sorption kinetics of MgH_2 by mechanical milling with TiF_3. *J. Alloys Comp.*, 432(1-2):L1–L4, 2007. [cited at p. 9]

[29] M. Mamatha and C. Weidenthaler. Mechanochemical preparation and investigation of properties of magnesium, calcium and lithium–magnesium alanates. *J. All. Comp.*, 407:78–86, 2006. [cited at p. 31]

[30] T. Matsunaga and A. Zuettel. Hydrogen storage properties of $Mg(BH_4)_2$. *J. All. Comp.*, 459:583–588, 2008. [cited at p. 70, 76]

[31] P. Mauron and A. Zuettel. Stability and reversibility of $LiBH_4$. *J. Phys. Chem. B*, 112:906–910, 2008. [cited at p. 69]

[32] P. Mauron and C.N. Zwicky. Stability and reversibility of $LiBH_4$. *J. Phys. Chem. B*, 112(3):906, 2008. [cited at p. 4]

[33] L. Mosegaard and T. R. Jensen. Intermediate phases observed during decomposition of lithium borohydride . *J. All. Comp.*, 446-447:301–305, 2007. [cited at p. 25]

[34] Y. Nakamori and S.I. Orimo. Correlation between thermodynamical stabilities of metal borohydrides and cation electronegativites: First-principles calculations and experiments. *Phys. Rev. B*, 74(4):045126, 2006. [cited at p. 23]

[35] E. Anne Nickels and P. P. Edwards. Tuning the decomposition temperature in complex hydrides: synthesis of a mixed alkali metal borohydride. *Angew. Chem.*, 47(15):2817–2819, 2008. [cited at p. 24]

[36] S. Orimo and L. Schlapbach. Hydriding properties of the MgNi-based systems. *J. Alloys Comp.*, 293-295:437–442, 1999. [cited at p. 9, 10, 19]

[37] S. Orimo and S. Towata. Dehydriding and rehydriding reactions of $LiBH_4$. *J. Alloys Compd.*, 427:404–406, 2005. [cited at p. 4]

[38] S.I. Orimo and C.M. Jensen. Complex hydrides for hydrogen storage. *Chem. Rev.*, 107(10):4111, 2007. [cited at p. 23]

[39] S.I. Orimo and A. Züttel. Dehydriding and rehydriding reactions of $LiBH_4$. *J. Alloys Compd.*, 404:424, 2005. [cited at p. 23]

[40] M.L. Post and J.J. Murray. Mg_2Ni hydride: In situ heat conduction calorimetry of the phase transition near 510 K. *J. Less-Common Met.*, 134(1):15–26, 1987. [cited at p. 15]

[41] S.B. Prima. *Al-Mg-Ni Phase Diagram, ASM Alloy Phase Diagrams Center.* ASM International, Materials Park, OH, 2006. [cited at p. 14]

[42] J.A. Ritter and R. Zidan. Implementing a hydrogen economy. *Materials Today*, 6(9):18, 2003. [cited at p. 3]

[43] J. Rodriguez-Carvajal. *FULLPROF : a program for Rietveld Refinement and Pattern Matching Analysis.* http://www-llb.cea.fr/fullweb/powder.htm, 2008. [cited at p. 11]

[44] T. Sato and D. Noréus. Attempts to improve Mg_2Ni hydrogen storage by aluminium addition. *J. Alloys Comp.*, 356-357:494–496, 2003. [cited at p. 9]

[45] S. Satyapal and G. Ordaz. The US Department of Energy's National Hydrogen Storage Project: progress towards meeting hydrogen-powered vehicle requirements. *Catal. Today*, 120:246–256, 2007. [cited at p. 3]

[46] L. Schlapbach and A. Zuettel. Hydrogen-storage materials for mobile applications. *Nature*, 414:353, 2001. [cited at p. 3]

[47] L. Seballos and E.H. Majzoub. Metastability and crystal structure of the bialkali complex metal borohydride $NaK(BH_4)_2$. *J. Alloys Comp.*, 476(1-2):446–450, 2009. [cited at p. 24]

[48] G. Soloveichik and J.-C. Zhao. Magnesium borohydride as a hydrogen storage material: Properties and dehydrogenation pathway of unsolvated $Mg(BH_4)_2$. *Int. J. Hydrogen Energy*, 34:916–928, 2009. [cited at p. 72, 74]

[49] J. Vajo and S. Skeith. Reversible storage of hydrogen in destabilized $LiBH_4$. *J. Phys. Chem. B*, 109(9):3719, 2005. [cited at p. 79, 80, 81, 82]

[50] M.J. van Setten and G. Brocks. A density functional study of α- $Mg(BH_4)_2$. *Chem. Mater.*, 20:4952–4956, 2008. [cited at p. 23]

[51] M.J. van Setten and M. Fichtner. A new phase in the decomposition of $Mg(BH_4)_2$: first-principles simulated annealing. *J. Mater. Chem.*, 19:7081–7087, 2009. [cited at p. 73]

[52] R.A. Varin and Z.S. Wronski. Catalytic effects of various forms of nickel on the synthesis rate and hydrogen desorption properties of nanocrystalline magnesium hydride (MgH_2) synthesized by controlled reactive mechanical milling (crmm). *J. Alloys Comp.*, 432(1-2):217–231, 2007. [cited at p. 9]

[53] J. Voss and T. Vegge. Structural stability and decomposition of $Mg(BH_4)_2$ isomorphs - an ab initio free energy study. *J. Phys. Condens. Matter.*, 21(1):012203, 2009. [cited at p. 38]

[54] L.-B. Wang and J. Li. An electrochemical investigation of $Mg_{1-x}Al_xNi$ ($0 \leq x \leq 0.6$) hydrogen storage alloys. *J. Alloys Comp.*, 385(1-2):304–308, 2004. [cited at p. 10]

[55] X.-B. Xiao and B.-Y. Tang. First-principles study of a double-cation alkali metal borohydride $LiK(BH_4)_2$. *J. Phys.: Condens. Matter.*, 20(44):445210, 2008. [cited at p. 24]

[56] H. Yabe and T. Kuji. Thermal stability and hydrogen absorption/desorption properties of $Mg_{17}Al_{12}$ produced by bulk mechanical alloying. *J. Alloys Comp.*, 433:241–245, 2007. [cited at p. 9]

[57] J. Yang and X. Li. Decomposition pathway of $Mg(BH_4)_2$ under pressure: Metastable phases and thermodynamic parameters. *Scripta Materialia*, 64(3):225–228, 2011. [cited at p. 73]

[58] H.-T. Yuan and W.-L. Gong. Electrochemical characteristics of $Mg_{2-x}Al_xNi$ ($0 \leq x \leq 0.5$) alloys. *J. Alloys Comp.*, 309:208–211, 2000. [cited at p. 10]

[59] A. Zuettel and Ch. Emmenegger. Hydrogen storage properties of $LiBH_4$. *J. All. Comp.*, 356-357:515, 2003. [cited at p. 66]

[60] A. Zuettel and Ch. Emmenegger. $LiBH_4$ a new hydrogen storage material. *J. Power Sources*, 118(1-2):1–7, 2003. [cited at p. 67, 68, 79, 81, 82]

[61] A. Zuettel and L. Schlapbach. *Hydrogen as Future Energy Carrier*. WILEY-VCH Verlag GmbH & Co. KGaA, Weinheim, February 2008. [cited at p. 50]

[62] E. Rönnebro. Development of group II borohydrides as hydrogen storage materials. *Curr. Opin. Solid State Mater. Sci.*, Article in Press, 2010. [cited at p. 3]